The Dissertation Committee for Lingyun Wang
certifies that this is the approved version of the following dissertation:

Embedded Metallic Grating and Photonic Crystal based Scanning Probes for Subwavelength Near-field Light Confinement

Committee:

Xiaojing Zhang, Supervisor

Dean P. Neikirk, Co-Supervisor

Andrea Alù

Li Shi

Hsin-Chih Yeh

Edward T. Yu

Embedded Metallic Grating and Photonic Crystal based Scanning Probes for Subwavelength Near-field Light Confinement

by

Lingyun Wang, B.S., M.S.

Dissertation

Presented to the Faculty of the Graduate School of
The University of Texas at Austin
in Partial Fulfillment
of the Requirements
for the Degree of

Doctor of Philosophy

The University of Texas at Austin
December 2012

Dedication

Dedicated to my wife Yingxu Xie
and our beautiful, extraordinary daughter Maggie Yixuan Wang.

Acknowledgments

First, I would like to express my gratitude to my parents, Lipei and Zhonglan Wang, for giving me the unconditional love and support over the years. I thank my wife for her love and support during the long journey. I thank our beloved daughter for all the joy she gives to me. During the process of this writing, whenever I ignore her, she always wants to point out her name on the dedication page in an excited way.

I thank my supervisor Dr. Xiaojing Zhang and co-supervisor Dr. Dean P. Neikirk for the invaluable support and guidance in my doctoral study. I also thank my committee members, Dr. Andrea Alù, Dr. Li Shi, Dr. Hsin-Chih Yeh and Dr. Edward T. Yu for serving on my dissertation committee and giving insightful advices on my dissertation research. I also thank the guidance from Dr. John A. Pearce and Dr. Karl D. Stephan in my earlier research experience. The collaboration with Dr. Kazunori Hoshino, Youmin Wang and Youngkyu Lee will be happily memorized for my life. I enjoy the friendship from faculty and staff from Microelectronics Research Center, Ricardo Garcia, Johnny Johnson, Dr. Marylene Palard and many others. I must thank Dr. Charles E. Mayer at the University of Alaska Fairbanks who makes me miss Alaska.

I also wouldn't forget my younger sister Yuhan's encouragement or discouragement during the process, for she always asks when I would finish the PhD.

Lingyun Wang

The University of Texas at Austin
December 2012

Embedded Metallic Grating and Photonic Crystal based Scanning Probes for Subwavelength Near-field Light Confinement

Publication No. ____________________

Lingyun Wang, Ph.D.
The University of Texas at Austin, 2012

Supervisors: Xiaojing Zhang
Dean P. Neikirk

Near-field light confinement on scanning probe is the backbone technology for near-field imaging with subwavelength resolution that overcomes the diffraction limit by exploiting the properties of evanescent waves. The fusion of the photonics and the latest nanofabrication technology creates emerging frontier for near-field light confinement research with new design approach. The propagation of light can now be controlled by periodical structure at subwavelength scale with low loss in the artificially synthesized dielectric material. New light propagation patterns can now be implemented in subwavelength structure, such as directional free space light focus grating coupler, photonic bandgap material like photonic crystal by permitting light propagation at certain wavelength while prohibiting light outside of bandgap, and nano-slot light resonator for increased light-matter interaction at nanometer scale. Advances in this research area will have tremendous impact on electromagnetic modeling and biomedical technology for probe based subwavelength optical detection. My doctoral research focused on investigating highly efficient, nanofabrication compatible directional light coupling structure and near-field subwavelength light focus through photonic crystal material.

The distinct significance of this research was placed on exploitation of the embedded metallic grating coupler of high free space directivity and subwavelength light processing circuit of enhanced near-field transmission rate, the two most dominating basic elements of the scanning optical imaging system. First, I designed a compact elliptical grating coupler based on embedded noble metal such as gold or silver that efficiently interconnects free space with dielectric rectangular waveguide. The dense system integration capability shows the application potential for on-chip interfacing subwavelength light processing circuits and near-field fluorescent biosensors with far-field detection of superb radiation directivity and coupling efficiency. Second, a novel all-dielectric light confinement probe designed by slotted photonic crystal waveguide provides a light confinement mechanism on the lateral plane. The resonating nano-cavities and the $\lambda/4$ nano-slot are used to enlarge the light throughput while as the nano-slot waveguide provides single subwavelength center lobe. The impetus of this research is the growing interests by near-field imaging researchers to obtain a low loss visible light confinement probe designs through mass production.

Table of Contents

List of Tables

List of Figures

Chapter 1

Introduction

The light confinement on probe tip has been realized by heating pulled optical fiber with metal coating or silicon wet etching probe tip. Plasmonic based probes by metal coating or metal optical structure has intrinsic drawbacks for heating damage due to Ohmic loss at visible range. The first motivation of this research is to find a modular monolithic probe system design that comprises compact light coupling, light illumination or collection, and subwavelength near-field light processing. The second motivation is to find a pure dielectric probe design that has minimal mode mismatch at the probe tip, and still compatible with mass fabrication technology.

1.1 Near-field scanning optical microscopy (NSOM)

The development of the light confinement on probe has been largely related with NSOM technology. In the meanwhile, NSOM technology is also one of the very important constituent of the scanning probe microscopy (SPM) family that comprises atomic force microscopy (AFM), scanning tunneling microscopy (STM), etc. Subwavelength near-field light confinement probes have been used for subwavelength imaging purposes, such as NSOM, high fidelity photo lithography, ultra dense optical data recording, and subwavelength photoluminescence measurement [1], since the proposal by the Irish scientist Edward Hutchinson Synge in 1928 [2]. In Synge's proposal, the colloidal gold particle is used for localizing light emission on a biological sample surface and overcomes the diffraction limit of far-field microscopy resolution limit. Figure 1.1 illustrates the light focusing size due the diffraction limit of a lens system. Due to the diffraction limited effects of confocal microscopy, the resolution r of the far-field based light confinement is no better than

$$r = \frac{\lambda}{2n\sin\theta} \tag{1.1}$$

where λ is the wavelength of the light, n is the refractive index of the object, and θ is the aperture half-angle of the optical system, as formulated by Ernst Abbe in the early 1870s [3]. By generating a light beam with spatial width that is far less than the wavelength, the

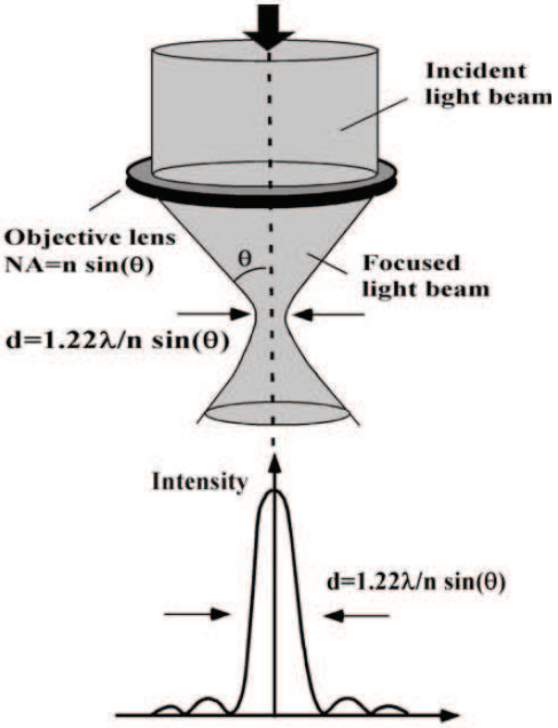

Figure 1.1: Diffraction limited far field light focusing limit. Copied from Figure 2.3 in [1].

imaging resolution size is no longer restricted by the diffraction effects and is dominated by the light source size [4, 5]. This concept is easy to understand, but very difficult to implement for useful application due to the lack of precise probe position control in nanometer scale at Synge's time, that Albert Einstein commented that the idea seems *prinzipiell unbrauchbar* ("essentially unusable") [6]. Due to the technical difficulties for probe control in visible or IR range, the first scanning near-field microscopy was demonstrated at 3cm microwave radiation range by E. A. Ash and G. Nichols in 1972 [7]. With the invention of STM in 1982 by Gerd Binnig and Heinrich Rohrer [8], who won the 1986 Nobel prize in physics, the idea of controlling the xy scanning stage and probe height through piezoelectric scanner, was brought to control the optical probe tip in $<$ 50nm scale to break the diffraction limit in optical imaging that demonstrated the first usable NSOM working in the optical range [9, 10].

The first generation of NSOM probe tip is formed by quartz rod with metal coated aperture tip [9] or metallic pipette with an aperture less than 100nm at the tip [10]. A typical NSOM system is illustrated in Figure 1.2, which comprises illumination part, collection part and detection part [11]. The stage position is controlled by shear-force detection in a feedback control loop, while the optical fiber probe tip is mounted in a fixed position with external laser feeding and polarization control. A inverted microscope objective is used to collect the light illuminated by the subwavelength laser source followed by the CCD spectrograph analysis and light intensity detector. Two sets of information about the sample surface can be obtained through this setup, the surface topography and the localized light distribution in subwavelength scale.

Though the light can be confined in subwavelength scale in the near-field, the throughput for the optical fiber based probe tip is quite low and susceptible to ambient light noise contamination due to the strong light propagation mode mismatch. Even

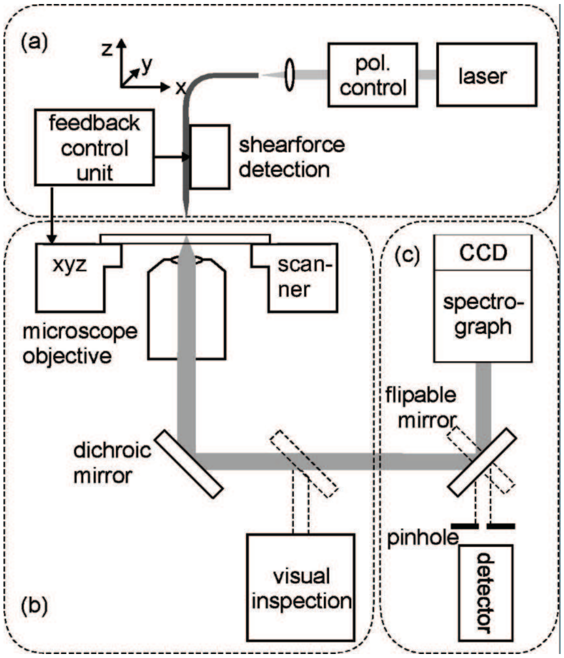

Figure 1.2: Standard NSOM setup. (a) illumination unit, (b) collection and redistribution unit, and (c) a detection module. Copied from Figure 2 in [11].

today, the current commercially available light confinement probe tips made by metal coated tapered optical fiber and some with nano slit aperture at the probe tip still suffer from low optical throughput, poor reproducibility and incompatible fabrication process for mass production. With the development of micro- and nano-fabrication technology, the second group of light confinement probes based on silicon (Si) cantilever technology have been using metal structure to enhance optical throughput and contrast by plasmonic effect since the 1980s. Various kinds of light enhancement structure made by metals have been proposed around the tip aperture, such as nano-grating [12], superlens [13], bow-tie [14, 15], dipole antenna [16], etc. Though stronger light enhancement has been observed in such probes, the added plasmonic metal structure in $<$100nm scale is technically difficult to fabricate and incompatible with the rest of the dielectric device structure. For $<$100nm scale metal structure, the heating damage due to the light ab-

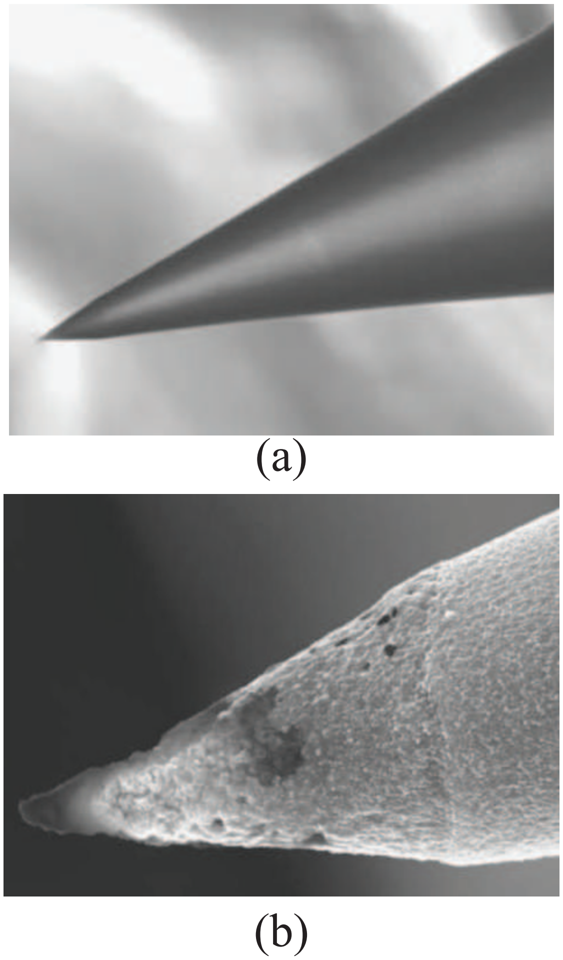

Figure 1.3: Heating damage of an optical fiber based NSOM probe tip with Al coating. The probe tip is fabricated by chemically etching method. (a) Before the heating damage; (b) After heating damage, the peel off of the Al coating is observed. Copied from Figure 4 in [17].

sorption is a fact that cannot be ignored. Figure 1.3 illustrates that a chemically etched optical fiber with aluminum (Al) coating can be easily damaged due to the heat generated by the metal layer.

So there are two main drawbacks with the designs aforementioned, light absorption due to metal material at visible wavelength and complicated fabrication process.

In order to overcome these shortcomings, this doctoral dissertation research proposes a novel probe based on dielectric PhC slot resonator technology that does not use any metal material as a light confinement and throughput enhancement mechanism at the probe tip with background free excitation. A compatible embedded metallic focus grating coupler is used to further enhance the light throughput through external laser source for coupling.

1.2 Light confinement technologies

To understand the light confinement mechanism in the proposed device, I modeled the structure using FDTD method [18] to estimate the light distribution. This novel probe will provide an important alternative light confinement probe design for the near-field imaging. The results of this dissertation research will answer the physics and engineering questions regarding the PhC light confinement: Will this probe provide an enormous optical properties improvement compared to that of the conventional near-field confinement probe designs? Is the nanophotonic device fabrication process compatible with the mass production? And finally, is the visible PhC material a good candidate that represents one of the next important nanophotonic device design trends for subwavelength near-field light confinement? This doctoral research combines the photonic bandgap (PBG) material and the near-field scanning probe microscope at visible wavelength to investigate the optical properties of the proposed all dielectric subwavelength light confinement probe and the device fabrication process based on Si micro machining technology. The impetus of this research is the growing interests by near-field imaging researchers to obtain a low loss visible light confinement probe through mass production.

1.2.1 Embedded metallic focus grating coupler

The grating coupler structure is modeled through CAvity Modeling FRamework (CAMFR) [19] and the FDTD method. The optimal geometries for the grating coupler, such as grating pitch period, maximum coupling angle, grating etching depth, metal layer thickness and far-field directivity are determined from the numerical modeling results. The light transmission efficiency from the far-field free space to the near-field of the probe tip and the full width half maximum (FWHM) beam width can also be quantified through the numerical EM modeling. The reverse process for light propagation from free space laser source to the dielectric waveguide is also modeled to show great light intensity enhancement.

1.2.2 Photonic crystal nano-resonator based slot aperture tip

Through numerical EM modeling tools such as fully-vectorial eigenmodes solvers of Maxwell's equations [20] and FDTD, the proposed light confinement probe can be accurately modeled to obtain the light distribution both inside the probe body and in the near-field from the probe tip. The probe is designed as a system that can be easily mounted and tested, and is compatible with mass fabrication process to lower the fabrication cost and complexity. Both the center placed slotted nano-resonator and quarter wavelength "air rod" type nano-resonator embedded in PhC waveguide have been proposed and numerically verified to show great light intensity enhancement in subwavelength scale. The total light intensity enhancement from the embedded metallic focus grating coupler and the nano-resonator on the probe tip shows enormous improvement with either that of the optical fiber based or plasmonic based probes.

1.2.3 Fluorescence differentiation and perturbation impact

The proposed grating coupler can also be used as a micro fluorescence detector due to the far-field radiation pattern difference for the exciting laser wavelength and the fluorescence emission signal. The isolation between the fluorescence molecule with the active metal grating layer avoids the common quenching effects due to the metal affiliation with the fluorophore. On the other hand the PhC resonator probe tip has been assessed with its performance variation under the impact of the water membrane in the near-field. Both the FWHM of the light beam in the near-field and the light throughput rate are calculated with the numerical modeling results. The fluorescence signal collection by the quarter wavelength "air rod" nano-resonator based PhC probe tip has also been studied by FDTD model.

1.3 Summary of research contribution

While I have examined many aspects of subwavelength near-field light confinement in my PhD, my main contributions have been on developing novel PhC structure and its efficient coupling to overcome the intrinsic light loss by other conventional methods. The current widely used light confinement probe by metal coated tapered optical fiber has intrinsic disadvantage of confining light in an inefficient manner due to its strong light propagation mode mismatch at the tip aperture. In my PhD research work, the light loss is reduced through deliberate design of light propagation mode match, and design a novel light confining probe of the combination by the embedded metallic grating coupler and PhC slotted waveguide based resonator probe aperture that has minimal light propagation mismatch and zero material absorption, while other plasmonic based light confinement methods have severe light absorption and light coupling challenges.

The design and performance of embedded metal grating coupler, and its application for PhC slotted waveguide probe tip embedded with nano-resonator for near-field light focusing at visible range have been quantified through numerical modeling. For the first time, the embedded metallic grating coupler has been quantified by its super high free space far-field directivity. Compared to other grating coupler designs, such as partially etched into waveguide layer or metal grating layer on top of the waveguide layer, as commonly used in the infrared wavelength for communication purpose, the embedded metallic grating coupler is more robust for the uncertainties errors during the fabrication process and more suitable for visible range device design with even smaller feature size tolerance. The far-field radiation pattern expressed in 3D directivity of the conventional etching compact focusing grating structure shows less free space directivity enhancement than that of the embedded noble metal grating coupler.

Another original contribution in this PhD work is the nanometer scale subwavelength light focusing and enhancement in near-field through PhC probe tip embedded with slotted nano-resonator. The 3D field distribution of the tip near-field is calculated to show the light focusing and enhancement due to the embedded nano-resonators. Various PhC tip designs are studied to obtain the optimum design strategy. This new near-field light focusing system is demonstrated to avoid the common drawbacks of the conventional scanning tip optical imaging system. Finally possible biological applications, such as spatial differential field distribution of the fluorescence signal by embedded metal grating coupler, and water perturbation in the PhC probe tip near-field is also discussed.

1.4 Dissertation organization

This dissertation is arranged as follows. “Chapter 1 Introduction” of the thesis gives an introduction of the brief history of the light confinement probe and the summary of the contribution from the proposed light confinement design. “Chapter 2 Review of nanoscale light confinement” presents the background study regarding the light confinement design, and the extensive review of the optical device design that the proposed probe is based upon, such as slotted PhC waveguide and nano optical PhC resonator. The overview of the design approach as proposed by this research is also discussed.

“Chapter 3 Design of dielectric focus grating couplers” studies the optical antenna principle and presents a design flow of the partially etched compact focus grating coupler by CAMFR and FDTD methods. Its performance in terms of 3D far-field directivity by FDTD method serves as reference for the following designs by embedded metallic grating couplers. The etching depth sensitivity on the far-field directivity change is also analyzed in detail. “Chapter 4 Design of embedded metallic focus grating coupler” investigates the dispersive optical properties of the noble metals such as gold and silver in optical wavelength range and proposes a compact focus grating coupler by embedding a thin layer of metal structure between the waveguide layer and the substrate layer to tremendously improve the far-field directivity towards free space direction with minimal light absorption and heating damage due to large heating dissipating area. The high tilted radiation angle case provides more free space coupling efficiency and directivity. The focusing effects of such grating couplers are also investigated in detail.

“Chapter 5 Design of photonic crystal waveguides for near-field light focusing” describes the light confinement probe made by nano slot embedded in the PhC waveguide structure for near-field light enhancement and subwavelength light confinement.

The focusing size and light intensity in the probe near-field are quantified to show the light enhancement and light confinement effects. Two sets of nano slot are presented in details. The first set of nano slot probe structure is based on embedding the nano resonator inside the probe body by forming a nano cavity by shrunk size air holes in the center of the line defect of the PhC structure. The second set of nano slot probe structure is using quarter wavelength nano slot much like a monopole antenna structure embedded the single line defect PhC waveguide in the very near end of the probe tip for near-field light confinement. Both the transmission line model and the numerical analysis yield the field distribution that the light resonance occurs at the end of the probe tip providing light intensity enhancement in subwavelength scale without Ohmic loss.

"Chapter 6 Applications in biosensing and imaging" introduces the possible biological application scenario for the proposed grating structure and PhC probe tip structure. The perturbation of water membrane in near-field and dielectric index change of bulk PhC structure are analyzed by numerical methods to assess the impact on the light confinement and enhancement in the near-field of the probe tip. Cy5 fluorescence signal excited at 632.8nm HeNe wavelength can be vertically detected in an enhanced way due to the far-field angular far-field directivity change of the embedded metallic grating coupler. Also the detection of Cy5 fluorescence signal by the proposed quarter wavelength slot PhC tip is analyzed to find the subwavelength fluorescence signal detection capability of such probe structure and the far-field fluorescence detection in an efficient manner.

"Chapter 7 Conclusions and future work" concludes the thesis and future work recommendation is also presented.

Chapter 2

Review of nanoscale light confinement

The first part of this chapter reviews the optical devices design concepts that the light confinement probe tip and grating coupler are based upon. Following the introduction of the general issues of other probe designs, a novel probe design approach overview is presented in the second part for the monolithic integration of the embedded metallic grating coupler and PhC-based subwavelength near-field light confinement.

2.1 Basic structures

The proposed light confinement probe will be based on optical devices, such as the slab PhC waveguide, the nano-resonating cavities and the slot waveguide. Not like the microwave counterpart, perfect conducting metal forms the waveguide boundary, by regular lattice of the dielectric index distribution the PBG of the PhC material provides an excellent light barrier without any light absorption by using only the dielectric material at visible or infrared band. There are many unique properties of the PhC which can be used to form low loss visible light waveguide. The nano-resonating cavities would enhance the light transmission rate from the probe body to the near-field of the probe tip. And the slot waveguide provide a mechanism to generate light confinement in the low index material at super subwavelength scale. Thus it is necessary to briefly introduce the related background knowledge on these basic design elements.

2.1.1 Photonic crystal devices

The PhC waveguide and the slotted waveguide are the two novel waveguiding structure as proposed recently. Compared to the conventional dielectric waveguide, the PhC waveguide provides more diversity on the light energy processing, and the slotted waveguide provides a mechanism to confine light on the lower refraction index region with subwavelength light confinement in the slot region for TE mode light propagation. The Fabry-Pérot (FP) resonating cavities can confine and enhance light concentration by the resonating effects of the enhanced standing waves. These optical properties will be used in this research as the probe design platform.

Si has relative high refraction index contrast and is relatively low absorption loss at near infrared (IR) wavelength ranges, which can be used to design PhC with much wider PBG [21]. Also Si micro-machining technology has been used to fabricate integrated circuit (IC) devices and is well developed since the 1970s. And Si PhC devices have been intensively studied and fabricated in the IR wavelength for optical communication applications [22]. However in the optical wavelength range, Si has strong loss that makes it not suitable for PhC devices in visible wavelength ranges [23]. Even the visible transparent materials with large refraction index contrast, such as GaN, AlN, and GaInP, have been used for visible range PhC designs [24, 25], most of them suffer from complicated and technologically challenging fabrication process [26]. Recently, silicon nitride (Si_3N_4) has been introduced as an alternative cost-effective optical PhC material due to its metal-oxide compatibility with Si fabrication technology and lossless optical property, which make it a promising candidate for optical PhC design [27, 28]. Even Si_3N_4 does not have high refraction index contrast as Si, it still has fairly large refraction index ($n \cong 2.02$) at wavelength of 632.8nm, and can be tailored to design visible

PhC device with wide enough PBG for fixed wavelength near-field imaging applications [29].

By etching air holes and patterning them through a three layers (SiO_2-Si_3N_4-SiO_2) or even two layers (Si_3N_4-SiO_2) planar thin film structure on top of a Si substrate, complete PBGs with non-directional and polarization insensitive properties have been realized in the 12-fold symmetric quasicrystals [30]. The complete PBG in triangular air hole lattice patterned on Si_3N_4 layer surrounded by two layers of silicon dioxide (SiO_2) in the near infrared and visible ranges have also been experimentally demonstrated [31]. Like one-dimensional (1D) diffraction grating reflects light in different angles according to the wavelength of the input light [32], the two-dimensional (2D) periodic optical structure made of dielectric and lossless material, also prohibits light propagation for a frequency range in all directions within the 2D plane under certain conditions [33, 34] as illustrated in Figure 2.1. The same phenomena happens for the three-dimensional (3D) periodic structure that the light propagation can be prohibited in all directions [35]. The

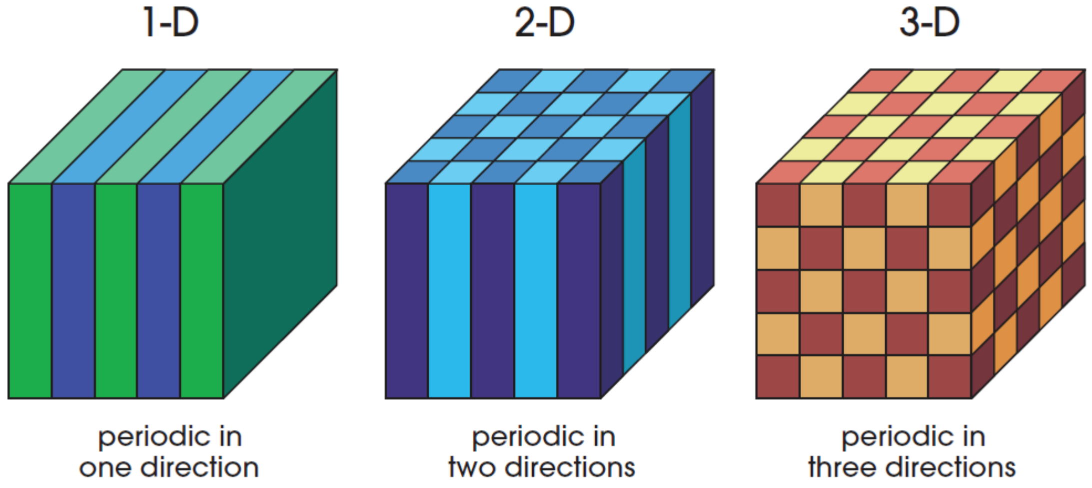

Figure 2.1: Schematic of the 1D, 2D and 3D PhC structures. Copied from Figure 1.1 in [36].

prohibited frequency range is defined as PBG. The 2D and 3D periodic optical structure are named PhCs. Though 3D PhC can manipulate light propagation in all directions, it is technically challenging to fabricate [36]. Since 2D PhC structures is easier to make, most research is focused on 2D PhC to manipulate light propagation in 3D. By removing a line of periodic index line in one direction, a single defect can be used to form a slab based PhC waveguide with light confined in vertical direction by TIR. In this research a single line defect 2D PhC waveguide design based on slab structure has been used to form the basic platform to embed the quarter wavelength slot as shown in Figure 5.6 and Figure 5.9 in Chapter 5.

PhCs exhibits unconventional dispersion properties that can be utilized to realize novel or improved signal processing functions [37]. Thus various kinds of micro-optical devices, such as PhC waveguide, filter and resonators etc., have been designed to change the light propagation direction, or to filter the light input. However the light confinement width in a typical single line defect 2D PhC slab waveguide, is about half wavelength [36], which is still too big for subwavelength light confinement for near-field imaging purposes. Thus it is common to use the near-field imaging tools like NSOM to study the light distribution in PhC devices. But the reversal process, that is using PhC devices to confine light for near-field imaging, is rarely investigated due to the intrinsic light confinement size of the regular 2D slab PhC waveguide as mentioned above. This dissertation research is anticipated to fill this research gap.

2.1.2 Optical slot waveguide

Conventional optical dielectric waveguides are using TIR mechanism to confine the light propagation in the high refraction index medium [38]. In biomedical application, light confinement inside an ultra small air space to interact with the bio-material is used to design the biomedical sensors [39, 40, 41]. Since the minimum light confinement size in the conventional waveguide is about half wavelength, it is hard to design the biomedical sensor by conventional dielectric optical waveguide. In order to overcome the shortcoming of the conventional waveguide, recently, a novel waveguide design that is based on slotted waveguide structure, has been proposed to confine the light propagation in the ultra small space with low refraction index [42, 43]. The slot waveguide is formed by two closely parallel packed dielectric strip waveguide separated by a narrow low refraction index slot, usually filled by air. As long as the cross section size of slot is less than evanescent penetration depth in the low refraction medium, the continuous electric displacement field boundary condition around the discontinuity interface of the refraction index contrast enables much higher electric field to appear in the low refraction index slot region. By placing two closely packed dielectric waveguide, a slotted optical waveguide can be formed to guide the light in the center slot region, given that the slot size is well less than the evanescent depth. In order to support the propagation mode in the slot region, the strip waveguides have to support symmetric traveling mode for quasi-TE polarized waves (electric field vector in vertical direction with respect to the interface). The relationship of the electric field at the refraction index discontinuity interface can be expressed as

$$\boldsymbol{E}_{low} = \frac{\varepsilon_{high}}{\varepsilon_{low}} \boldsymbol{E}_{high} \tag{2.1}$$

where ε_{high} and ε_{low} are the dielectric constant for high and low refraction index mediums respectively, and $\boldsymbol{E}_{high}$ and $\boldsymbol{E}_{low}$ are the electric fields in respective mediums. Since only the boundary condition is involved, the slot waveguide is wavelength independent. The slot waveguide shows great potential in high performance active devices and ultra-sensitive sensors etc., where highly confined light-material interaction is preferred [44, 45]. Rigorously, the analytical solution for the TE field profile E_x as illustrated in

Figure 2.2 can be formed by the interaction between the fundamental TM eigenmodes of the individual slab waveguides as

$$\boldsymbol{E}_x(x) = A\begin{cases} \dfrac{1}{n_S^2}\cosh(\gamma_S x), & |x| < a; \\[2ex] \dfrac{1}{n_H^2}\cosh(\gamma_S a)\cos[k_H(|x|-a)] + \dfrac{\gamma_S}{n_S^2 k_H}\sinh[k_H(|x|-a)], & a < |x| < b; \\[2ex] \dfrac{1}{n_C^2}\{\cosh(\gamma_S a)\cos[k_H(b-a)] + \\ \quad \dfrac{n_H^2\gamma_S}{n_S^2 k_H}\sinh(\gamma_S a)\sin[k_H(b-a)]\}\exp[-\gamma_C(|x|-b)], & a < |x| < b. \end{cases} \tag{2.2}$$

where k_H is the transverse wave number in the high index slabs, γ_C is the field decay coefficient in the cladding, γ_S is the field decay coefficient in the slot, and constant A is given by $A = A_0\dfrac{\sqrt{k_0^2 n_H^2 - k_H^2}}{k_0}$, where A_0 is a arbitrary constant, and k_0 is the wave number in free space [46]. The dimension and the geometry of the derivation is shown

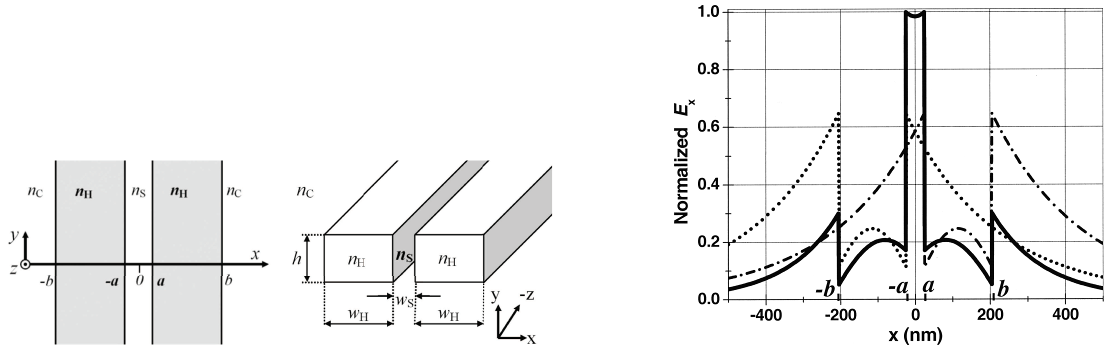

(a) Cross section and 3D views of the slotted waveguide

(b) Electric field $|\boldsymbol{E}|^2$ distribution

Figure 2.2: Slotted waveguide model. (a) Schematic cross section view and 3D view of the slot waveguide. (b) Normalized $\boldsymbol{E}_x$ for TE field of the fundamental TM eigenmode (solid curve) for slab-based slot waveguide at $\lambda_0 = 1.55\mu m$, with $n_H = 3.48$, $n_S = n_C = 1.44$, $a = 25nm$, and $b = 205nm$. The individual TM eigenmode is also shown as the dotted and dashed-dotted curves [46].

in Figure 2.2(a). Thus by given material optical properties and working wavelength, the field distribution can be analytically obtained as illustrated by the example structure in Figure 2.2(b) as derived from equation (2.2). The slot waveguide design based on Si_3N_4 and SiO_2 platform has been experimentally verified [47]. By filling the slot through SiN dielectric waveguide strips with SiO_2 material, a discontinuity generates the high electric field to concentrate in the slot. The Si_3N_4/SiO_2 slot waveguide fabrication process is also compatible with the state of the art silicon device fabrication technology. The slab slot waveguide as illustrated in Figure 2.2 is essentially the nano light confining cavity excited by TE mode light.

It was also experimentally demonstrated by replacing one line of air hole in ΓK direction in triangular air hole lattice on silicon slab that is based on silicon on insulator (SOI) fabrication technique [48, 49]. But the simple straight slab waveguide cannot provide further light processing functions like resonating cavity, and lossless transmission along sharp curves. On the other hand, since the PhC waveguide can slow down the light propagation speed to a fraction of that in the free space, light can have more interaction with the guiding medium [50]. However since the slab PhC waveguide made by air holes cannot provide empty space for the molecular targets, the application of the slab PhC waveguide in biological or chemical detection is greatly restricted. Thus a new light confinement idea was proposed by combining the slab slot waveguide and the PhC slab structure in order to leverage the PhC's versatile micro-optical device design advantages onto the biosensor designs or subwavelength light confinement.

2.1.3 Nano Fabry-Pérot resonating cavity

Micro optical resonator plays an important role in optical signal processing such as optical modulators, filters, delay lines, switches, sensors etc. [51]. In this research the

PhC resonators are designed to enhance the light throughput to overcome the dielectric interface barrier for the light confinement probe. The 2D slab PhC material provides a platform for a variety of micro-resonators on which line defect cavities with patterned air holes have been extensively investigated in subwavelength scale. The 1D FP model can adequately describe the working mechanism of the the PhC nanocavity coupled to PhC waveguides as illustrated in Figure 2.3. As illustrated in Figure 2.3(a) and (b), the total round trip phase delay $\Phi_T(\lambda_0)$ has to be equal a integer multiple of π in order to form a FP cavity by two metallic mirrors,

$$\Phi_T(\lambda_0) = k_0 n_{eff} L + \phi(\lambda_0) = m\pi, \tag{2.3}$$

where L is the actual cavity length, n_{eff} is the effective index equals $c(\frac{d\omega}{dk_z})^{-1}$ and m is an integer [52]. And the horizontal quality (Q) factor for the coupling waveguide as defined as Q_h in Figure 2.3(c) can be expressed by 1D FP model with metallic mirrors as,

$$Q_h = \frac{\pi}{1-R}\left[\frac{2Ln_g}{\lambda_0} - \frac{\lambda_0}{\pi}\left(\frac{\partial\phi}{\partial\lambda}\right)_{\lambda_0}\right]. \tag{2.4}$$

where $R = |r|^2 = [|r|\exp(i\phi)]^2$ is the mirror reflectance. By assuming the penetration depth into the mirror as $L_p = -\frac{\lambda_0^2}{4\pi n_{eff}}(\frac{\partial\phi}{\partial\lambda})_{\lambda_0}$, equation (2.4) can be further simplified as ,

$$Q_h = \frac{k_0}{1-R} n_g (L + 2L_p), \tag{2.5}$$

where $k_0 = \frac{2\pi}{\lambda_0}$ is the wavenumber in freespace [52]. As illustrated in Figure 2.3(c), the out of plane radiation loss will dominate the overall Q factor if the 2D PhC cavity is within PBG in the horizontal plane. If the Q factor of the out-of-slab radiation loss is expressed as Q_v, then the overall Q factor $Q_{overall}$ can be written as [53]

$$Q_{overall}^{-1} = Q_v^{-1} + Q_h^{-1}. \tag{2.6}$$

On the other hand, the transmittance T of the PhC waveguide coupled nanocavity can be obtained as [53]

$$T = \left(\frac{Q_{ovreall}}{Q_h}\right)^2 = \left(\frac{Q_h^{-1}}{Q_v^{-1} + Q_h^{-1}}\right)^2. \tag{2.7}$$

2.2 Modular scanning probe integration

To solve the issues faced by the conventional optical probe design, here is my approach to this problem through deliberate design of light propagation mode. A novel light confining probe of the combination by the embedded metallic grating coupler and

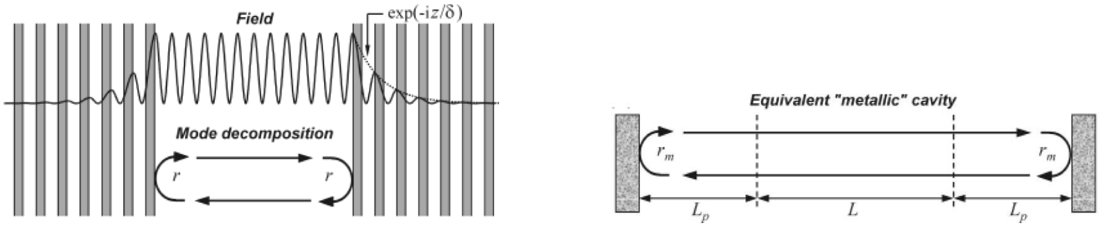

(a) FP electric field of the cavity mode

(b) Equivalent “metallic” cavity

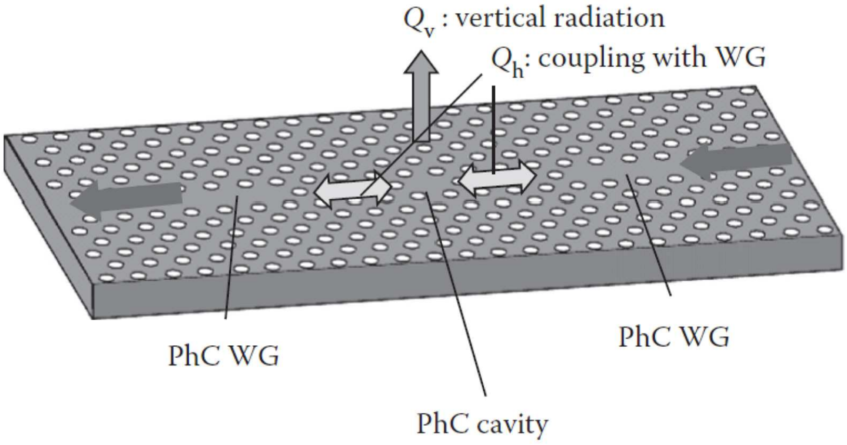

(c) Illustration of PhC nanocavity coupled to PhC waveguides by Q factors

Figure 2.3: FP resonator model. (a) FP electric field of the cavity mode [52]. (b) Equivalent “metallic” cavity [52]. (c) Illustration of PhC nanocavity coupled to PhC waveguides by Q factors [53].

PhC waveguide with slot nano-resonator on single chip design have been designed with minimal mismatch at the probe tip that overcomes the disadvantages of the optical fiber based probe. The proposed light confinement probe design is based on the monolithic integration of the two parts as illustrated in Figure 2.4. Since there is no metal coating or other metal structure for plasmonic effects, there is no light absorption and the transmission rate is also greatly enhanced by joint focusing capabilities of both the compact embedded metallic grating coupler and the PhC nano-resonator. Due to the relative large area for heat dissipation, the metal absorption effects with heating damage in the light coupling part is greatly suppressed. The total design can be fabricated on monolithic integration platform using the state of the art of electron beam lithography (EBL) pattern writing technique to define the nano-structure in nanometer scale.

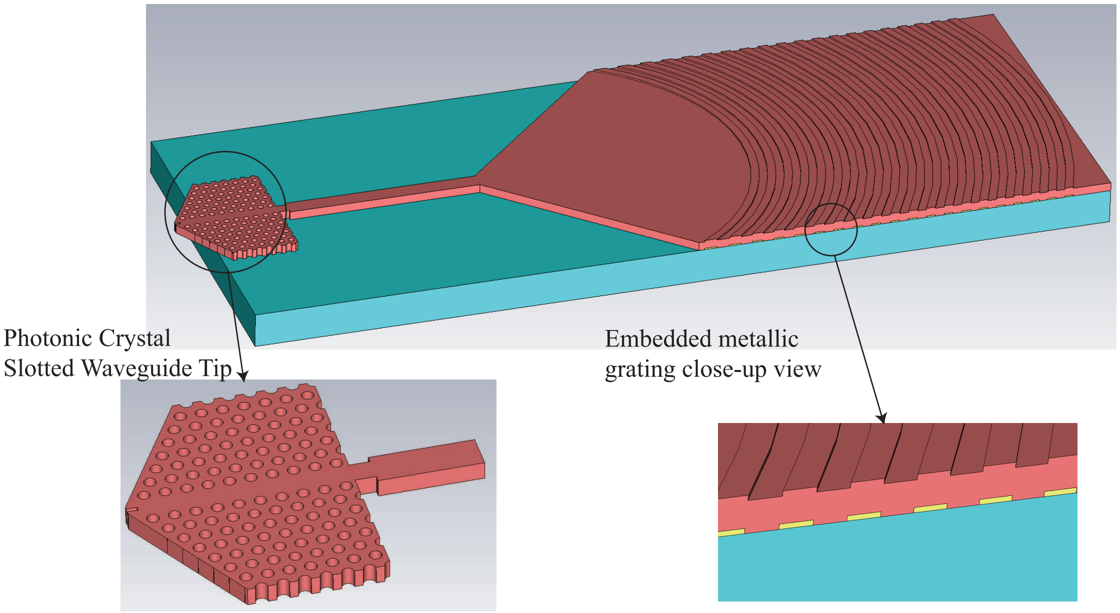

Figure 2.4: Schematic of the proposed light confinement probe tip formed by PhC nano-resonator tip and the embedded metallic grating coupler as a whole system. The geometry is only for illustration purpose and cannot be scaled.

2.2.1 Embedded metallic grating focus coupler

Conventional light coupling technologies to subwavelength waveguide include bulky back plate prism coupling, which is not suitable for compact dense system integration [54], and optical fiber end fire coupling with waveguide facet, which requires stringent alignment accuracy [55, 56], especially at visible wavelength range due to the even smaller waveguide core size. The concept of on-chip grating coupler design has been extensively researched at longer IR communication wavelength due to the rapid development of telecommunication industry and the SOI fabrication technologies during the last several decades. The grating structure is defined by either metal lift-off on top of the waveguide layer [57] or etching the grating grooves partially or fully into the higher index waveguide layer from the top waveguide layer surface [58, 59]. The partial etching approach suffers from inaccuracy in etching depth control due to non-stopping layer etching. As it is shown by this study of the etched grating coupler, the etching depth is a very critical parameter for 3D far-field pattern control and coupling efficiency. In the fully etched grating case, which requires less on etching depth control, however, at least half of the light will unavoidably propagate into the substrate layer which strongly decreases the transmission efficiency into the optical fiber or free space [59]. In many grating designs, the high coupling efficiency with free space is the utmost design goal, and the light scattering into the substrate layer should be well managed to minimize the energy loss. For example, in the SOI grating design at IR wavelength, usually multiple layers Bragg reflectors formed by stacking oxide layers [60], is used to reduce the effective substrate index. The metal lift-off approach excels for its relative easy fabrication and low absorption loss of the thin metal layer thickness (usually less than tenth of the wavelength).

However their counterpart at visible wavelength did not share equal attention and met greater challenge, because of even smaller feature size restriction on fabrication and non-transparent property of silicon at visible range. For more accurate electromagnetic modeling, such as the FDTD method, extensive dispersion modeling of the dielectric properties of metals, need to be implemented to conform with the experimental data of the complex dielectric property of metal, due to the negative real part of its permittivity property. Subwavelength optical detection, such as in NSOM [61, 62, 63, 64] or through nano-optical antennas [65] and the silicon nitride PhC and nano-resonator on probe tip for near-field light localization have been demonstrated [66, 67]. All these designs mandate efficient and compact light coupling from subwavelength light processing circuits or vice versa. In this doctoral research, a compact noble metal grating coupler design for free space directional light coupling from or into subwavelength Si_3N_4 optical waveguide working at HeNe laser wavelength at 632.8nm is analyzed to fill the research gap from device modeling perspective for noble metal grating by placing it just below the waveguide layer to block coupling loss into the substrate. The fabrication of the proposed noble metal grating coupler is compatible with silicon micro-machining technology and it offers a new concept of light coupling at 632.8nm wavelength, with comparable coupling efficiency as the IR wavelength counterpart.

This research also exploits the possible fluorescence signal enhancement by the proposed metallic grating coupler. The current state of the art in the fluorescence detection strongly depends on directive light propagation property and the surface modification techniques that control the affinity between fluorescent molecule and the active light emitting surface. Most of the fluorescence detection modifies the metal surface, such as gold or silver, which also weakens the fluorescence signal due to the quenching effects [68]. The proposed light coupling device can overcome the quenching issue through isolating the metal layer and the active affinity surface by dielectric material of Si_3N_4. And the surface modification can be realized in top of the Si_3N_4 surface [69]. Due to the 1st order diffraction angle dependence on light wavelength, the fluorescence signal can be further extracted and distinguished from the excitation source through radiation pattern difference by low aperture objective lens in free space. By separating the fluorescent light propagation and exciting source light coupling with large angle at 10°, the background light noise can be greatly suppressed to enhance the weak fluorescence light detection.

Compared to large size non-focusing grating design [70, 71, 72], the proposed compact metallic focus grating size also makes large scale nano-system integration possible to provide a mechanism for both light coupling and fluorescence signal extraction to detect large quantities of the nano scale localized protein or DNA binding process simultaneously within one single silicon or glass chip. The far-field radiation patterns of silver or gold at both excitation and fluorescence wavelengths are quantified through FDTD simulation results, and it agrees well with grating diffraction theory.

2.2.2 Photonic crystal nanoresonator based light confinement probe tip

Near-field scanning optical microscopy (NSOM/SNOM) is a microscopy technique for nano-structure investigation that breaks the far-field resolution limit by exploiting the properties of evanescent waves with lateral resolution of 20nm and vertical resolution of 2-5nm has been demonstrated. However, the current widely used NSOM probe by metal coated tapered optical fiber has intrinsic disadvantage of confining light in an inefficient manner due to its strong light propagation mode mismatch at the tip aperture as illustrated in Figure 2.5. The light propagation inside a pulled optical fiber can be modeled by the tapered cylindrical waveguide. In the case of metal coated optical

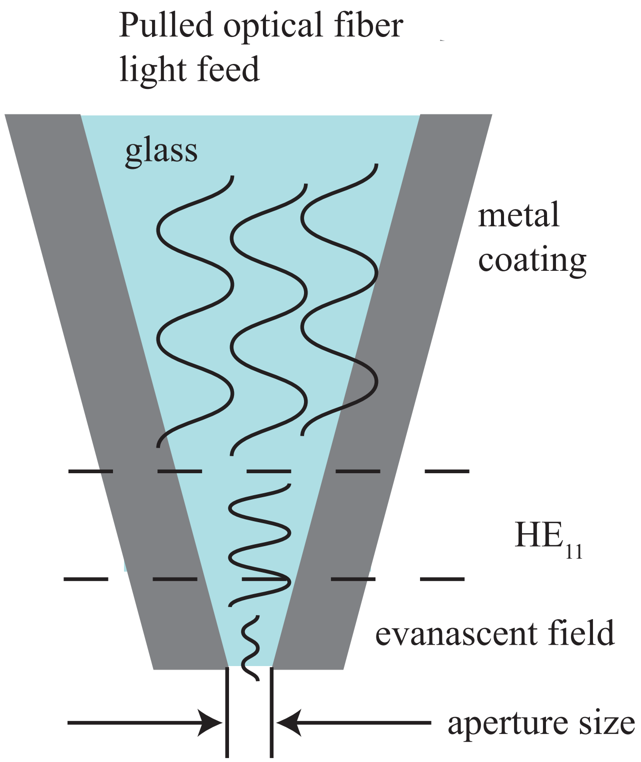

Figure 2.5: Metal coated pulled optical fiber probe tip model with HE_{11} mode illustrated. Figure replotted from Figure 5 in [11].

fiber tip, only the optical fiber fundamental mode, e.g. hybrid electric mode HE_{11}, can propagate out the probe body at the near-field in evanescent wave form [11]. Similar to the microwave waveguide counterpart, the metal coated pulled optical fiber also have the cut-off frequency, and the light throughput for such probe is extremely low (about $1 \times 10^{-8} - 8 \times 10^{-6}$ for aperture size of 70nm) due to the mode mismatch and the metal absorption loss [73]. Similarly most of the plasmonic based probes use metal to generate the surface plasmon polaritons (SPPs) wave to make subwavelength resonance at some nanometer probe aperture, like monopole antenna. For this type of probe, metal has to be applied to confine the light not only in the probe body, but on the nano probe metal tip. But in optical wavelength range, strong absorption loss and heating damage effects are unavoidable problems that need to be addressed.

In this doctoral research, a PhC based probe tip is proposed and analyzed by numerical methods to enhance the light transmission rate through embedded nano-resonator on the probe tip. The resonator near the probe tip aperture overcomes the impedance mismatch between the probe body and the near-field free space medium, which causes strong reflections in the pulled metal coated optical fiber based probe designs. The nano slot aperture not only forms single lobe inside the probe body by the continuous electric displacement field boundary condition as mentioned in the last section for TE mode excitation, but also removes the impedance mismatch in the probe tip, since the medium in both the near-field and the air slot region are the same. Thus no impedance mismatch exists between the slot tip aperture and the near-field free space. In this research both the bulk resonator cavity designed through placing the shrunk air holes with certain resonating distance, and the compact nano-resonator through controlling the slot length itself to form the optical monopole antenna are analyzed in detail using numerical simulation tools. Compared to normal single slot waveguide, the PhC based slot waveguide prohibits light penetration into the bulk PhC material. Light has no place to go except stay inside the PhC waveguide line defect. Thus the slot resonator is driven by well insulated light source in a loss free manner, which explains the high throughput. Compared to metal based optical waveguide, the bulk PhC boundary shows no light absorption due to Ohmic loss. Much stronger light transmission enhancement has been observed by the field distribution in the near-field using 3D FDTD simulation with zero material light absorption and minimal light propagation mode mismatch.

Chapter 3

Design of dielectric focus grating couplers

This chapter reviews the optical antenna theory and presents a design flow for a partially etched dielectric focus grating coupler through the numerical tools of the eigenmode expansion frequency domain method and FDTD simulation. The far-field antenna directivity is used to quantify the performance of the grating coupler designs. The etched dielectric grating coupler design flow serves as the reference design model that will be compared with the metallic embedded grating coupler in terms of loss and far-field directivity in the later Chapters.

3.1 Optical antenna principle

Based on optical antenna radiation theory, the far-field directivity radiation pattern and antenna radiation efficiency, can be used to quantify both the beam pattern and the transmission efficiency within certain angular range. In this section, the optical antenna radiation theory is briefly reviewed. The 3D radiation patterns in terms of far-field directivity for the grating couplers are quantified by 3D FDTD simulation to reveal the focusing and enhanced directivity properties.

The efficiency of a radio frequency (RF) antenna describes how efficient the local oscillating driving current is transformed into far-field radiation energy, P_{rad}, for radiation antenna or vice versa for receiving antenna. Since most of the RF antenna deals with lossless metal material, most of the RF antenna radiation efficiency loss is caused by strong impedance mismatch. However in the optical range, metal may no longer be simplified as lossless material due to the dispersive dielectric properties with negative imaginary part of dielectric constant. The radiation loss is largely caused by the absorption or Ohmic loss of the metal materials, P_{loss}, which cannot be ignored in the electric field calculation. If the impedance mismatch loss is simplified to be zero, the radiation efficiency of an optical antenna is defined as [74]

$$\varepsilon_{rad} = \frac{P_{rad}}{P_{rad} + P_{loss}}. \tag{3.1}$$

The radiation efficiency only quantifies the total radiation efficiency but not the radiation in certain direction. The total radiation power, P_{rad}, can be defined as the integration for all directions of the normalized angular radiation density, $P_n(\theta, \varphi)$ [74]

$$P_{rad} = \int_0^{\pi} \int_0^{2\pi} P_n(\theta, \varphi) \sin\theta d\varphi d\theta. \tag{3.2}$$

The average angular radiation intensity P_{av} of an equivalent isotropic radiator can be expressed as $P_n(\theta, \varphi)$ [74]

$$P_{av} = \frac{P_{rad}}{4\pi}, \tag{3.3}$$

that calculates the angular radiation intensity with the same total radiation power. The directivity of antenna is a dimensionless parameter that describes the focusing capability of radiation beam at certain angle at far-field. It is as quoted in the John D. Kraus's classic antenna textbook [75], "The *directivity* D of an antenna is given by the ratio of the maximum radiation intensity (power per unit solid angle) to the average radiation intensity (averaged over a sphere)", which refers to the maximum directivity direction at the far-field. For arbitrary directions, the angular directivity D is defined as [74]

$$D = \frac{P_n(\theta, \varphi)}{P_{av}} = 4\pi \frac{P_n(\theta, \varphi)}{P_{rad}}. \tag{3.4}$$

The gain of the antenna combines both the antenna directivity and the antenna efficiency

$$G = \varepsilon_{rad} D, \tag{3.5}$$

and is a parameter that relates to the antenna radiation efficiency in certain direction. In this chapter, both the angular directivity D and the maximum directivity will be used to describe the far-field radiation pattern of the grating coupler, since the radiation efficiency is almost a constant value due to zero Ohmic loss for dielectric material.

3.2 Etched dielectric grating coupler

In order to feed light efficiently into the photonic crystal probe tip or other similar nano-scale light processing circuits, the light feeding method has to be carefully examined for such a nanometer scale size probe tip to avoid unwanted light contamination and enhance signal to noise ratio for light detection or coupling. Before we discuss the embedded metal grating design, it is useful to analyze the partially etched grating coupler and evaluate its performance. The partially etched grating coupler is usually fabricated by electron beam lithography (EBL) and dry etching method [76]. Other grating fabrication methods, such as polymer based grating [77], deep UV lithography [78], achromatic interferometric lithography [79], etc., have also been found in literature. In IR wavelength, an out-of-plane grating coupler is adapted to efficiently butt-couple light from single mode fiber into ridged waveguide [76]. The grating coupler also achieves beam spot converting from the grating square into the narrow ridged waveguide. In this section, the eigenmode expansion technique is first used to estimate the optimal etching depth and the grating pitch period. Then a compact focus grating coupler is analyzed by 3D FDTD method in terms of far-field directivity and coupling efficiency. Finally the

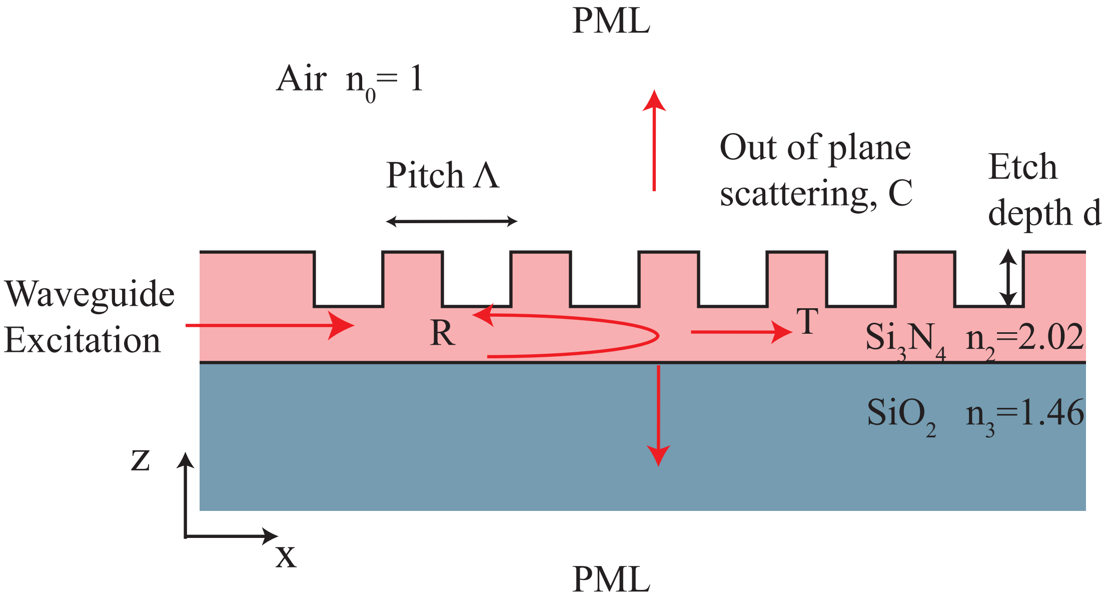

Figure 3.1: CAMFR calculation model on eigenmodes of the 1D partially etched grating coupler on Si_3N_4 waveguide layer on top of the SiO_2 substrate.

impact of etching depth on the far-field directivity is presented to illustrate the strong etching depth sensitivity.

3.2.1 Etched grating analysis by CAMFR

CAMFR is an eigenmode expansion frequency domain modeling tool to optimize the optimal grating pitch period and groove depth for the 1D grating in the 2D simulation domain in a time saving fashion with relatively good accuracy [80]. Only TE polarization (electric field parallel to the grating grooves) is considered in this study, since all the following PhC design is also based on TE mode calculation. As illustrated in Figure 3.1, the reflection rate R and transmission T rate can be calculated by finding the eigenmode of each discretized slab in the vertical direction. The total out-of-plane light coupling can be expressed as $C = 1 - R - T$. The peak reflection corresponds to

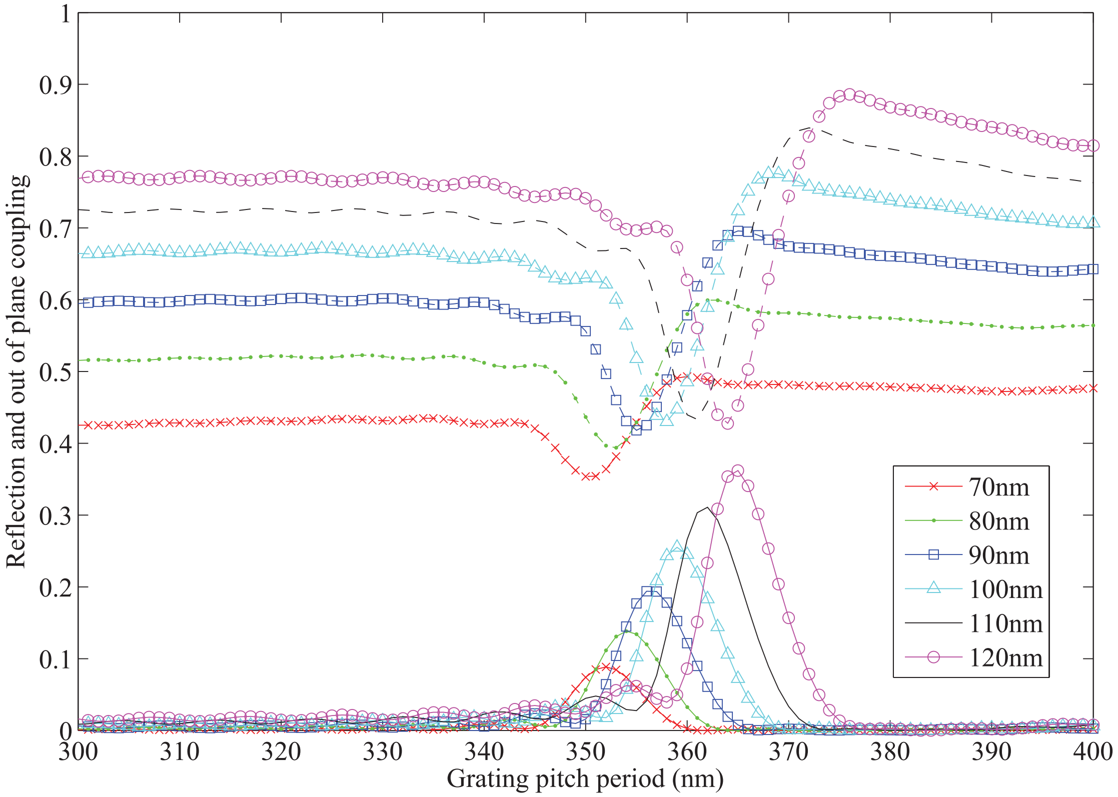

Figure 3.2: Reflection (bottom solid lines) and out-of-plane coupling (top dashed lines) rates as function of grating pitch period for etching depth ranging from 70nm to 120nm.

the grating coupler resonance condition that maximum out-of-plane coupling radiates in the vertical direction. In this grating structure, there is no special mechanism to prevent the light coupling loss into the substrate. Si_3N_4 of 250nm thickness is chosen as the waveguide layer due to its transparent optical property at 632.8nm wavelength. SiO_2 serves as the substrate layer. The CAMFR calculation domain is surrounded in upper and bottom boundaries with sufficient perfect matched layer (PML) thickness in order to reduce the light back reflection at the calculation boundaries. The CAMFR simulation code is listed in the Appendix I.

The reflection and out-of-plane efficiency is shown in Figure 3.2 by sweeping both the grating pitching size within the range from 300nm to 400nm in 1nm interval and the etching depth from 70nm to 120nm in 10nm interval with 50% grating duty cycle. At the reflection resonance pitch period Λ_p the out-of-plane light coupling curve also shows the minimum value due to strong reflection. At the same time, the out-of-plane coupling rate enhancement also increases the free space coupling rate. By finding out the pitch period that corresponds to the maximum out-of-plane coupling, the effective index of the waveguide grating composite structure can be calculated using effective index equation under vertical radiation condition

$$n_{eff} = \frac{\lambda_0}{\Lambda_p}. \tag{3.6}$$

It is found that 110nm etching depth with 361nm pitch period gives the maximum out-of-plane coupling rate with effective index of 1.7529 at the reflection resonance pitch period. For arbitrary out-of-plane coupling angle θ, the effective index can be estimated from the 1st order grating diffraction equation [77]

$$n_{eff} = n_0 \cdot \sin\theta + \frac{\lambda_0}{\Lambda_p}, \tag{3.7}$$

where n_0 is the refraction index of top cover material (free space in the proposed grating coupler), Λ_p is the grating pitch period, and λ_0 is the wavelength in free space.

3.2.2 3D far-field directivity of etched grating coupler

CAMFR provides a convenient way to predict the effective index for maximum out-of-plane coupling under vertical radiation condition as indicated by equation (3.6). However for arbitrary 3D grating coupler design with radiation angles other than vertical direction, the light coupling distribution has to be verified through 3D FDTD modeling. Such a 3D compact focusing grating coupler is modeled as in Figure 3.3 with azimuth angle φ and polar angle θ as indicated that are used to set the polar coordinates of the antenna directivity pattern. The origin point of the (x,y,z) orthogonal coordinates is located at dielectric rib waveguide end facet center as indicated in Figure 3.3. For polarized plane wave light source, the wave vector front is regulated by constructive interference according to the first order Bragg's diffraction theory. The focusing capability is realized by constructive interference of the wave front phase between the wave coming from the dielectric waveguide and the scattered wave from grating groove lines into the free space at the 1^{st} order diffraction angle. The 3D constructive interference on the center *xy* plane of the silicon nitride waveguide layer can be described by the phase matching equation below

$$q\lambda_0 = n_{eff}\sqrt{x^2+y^2} - xn_0 \sin\theta_0, q = 1,2,3,\ldots, \tag{3.8}$$

where q is the grating line numbers. In order to achieve focusing effects on *xy* plane, the Si_3N_4 waveguide ending facet needs to be positioned at the focal point of the elliptical curves [77]. It describes a set of ellipses that share a common focus point at $(0,0)$ on *xy* plane. At the $y=0$ cross line, the pitch period of the grating equals that in equation (3.6).

The electric field component E_y on the center plane of $y=0$ are plotted for the vertical maximum resonance case and the $\theta_0 = 10^\circ$ tilted case respectively as illustrated in Figure 3.4 based on 3D FDTD calculation results. A waveguide port with broadband excitation centered at 632.8nm wavelength is used as excitation source which is located at the single mode Si_3N_4 ridge waveguide of 250nm in thickness and 500nm in ridge width with TE mode linear polarization. All the boundaries are set up as open space with PML to reduce the back reflection calculation error. The size of the grating coupler is 10μm in y direction and 7μm in x direction which would fit the approximate core size of single mode optical fiber at 632.8nm wavelength. The overall relative small size of

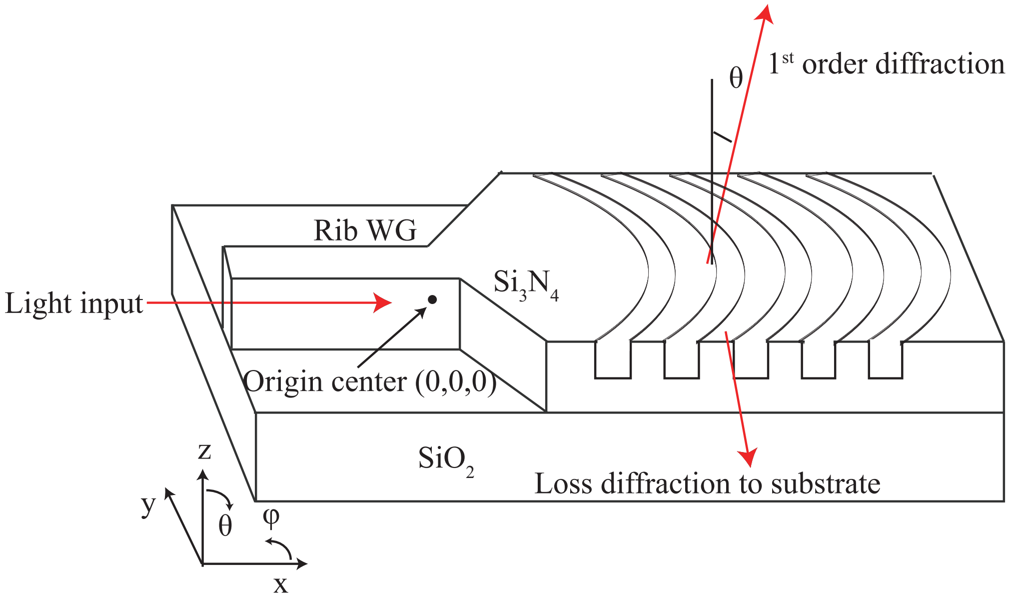

Figure 3.3: 3D FDTD model of the etched silicon nitride grating coupler design with spherical axis as labeled.

the grating coupler also helps greatly reduce FDTD calculation time. It is observed that the grating coupler design as shown in Figure 3.4(b) with $\theta_0 = 0^\circ$ and $n_{eff} = 1.7529$ as described by equation (3.8) has the light propagation pattern of the maximum vertical radiation resonance as predicted by CAMFR calculation. By only changing the tilted angle θ_0 in equation (3.8) with the same effective index, the light propagation is tilted correspondingly towards the free space as shown in Figure 3.4(c).

The grating coupler FDTD simulation can be treated as a typical optical antenna problem by converting the near-field light distribution into the far-field radiation pattern [81]. The far-field directivity of the etched compact grating coupler is shown in Figure 3.5, in which both vertical out-of-plane coupling of the peak reflection resonance case and the 10° tilted radiation of the same effective index are plotted. There are two radiation lobes for both the vertical radiation coupler and 10° tilted coupler. This

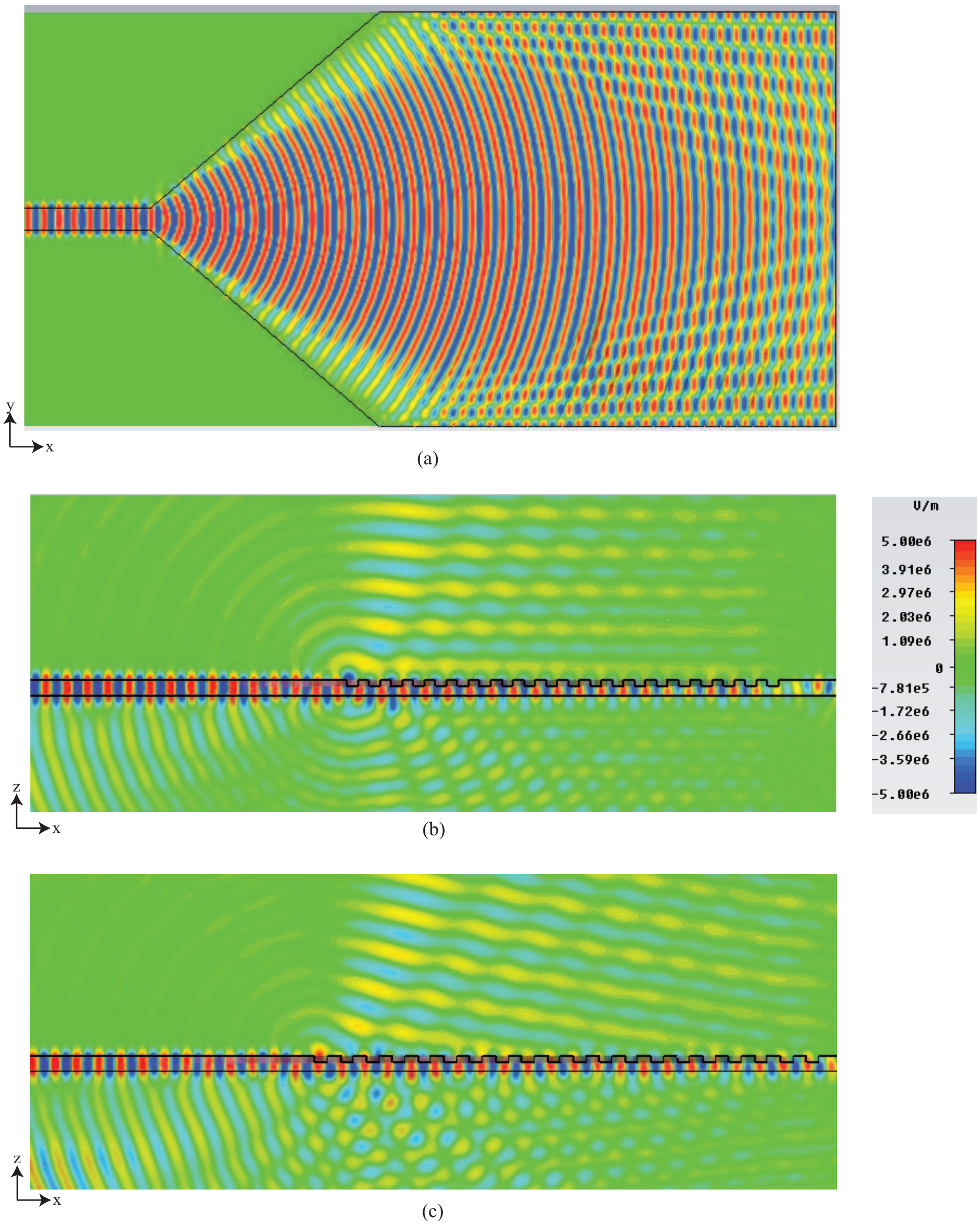

(a)

(b)

(c)

Figure 3.4: Electric field component E_y plot for etched grating coupler for vertical radiation and the $\theta_0 = 10^\circ$ grating couplers by 3D FDTD. (a) Vertical maximum resonance case for $n_{eff} = 1.7529$ on the center cross section xy plane of waveguide layer; (b) Vertical maximum resonance case for $n_{eff} = 1.7529$ on the $y = 0$ cross section plane; (c) Titled radiation case for $\theta_0 = 10^\circ$ on the $y = 0$ cross section plane of the same effective index. All the grating coupler here has 110nm optimized etching depth.

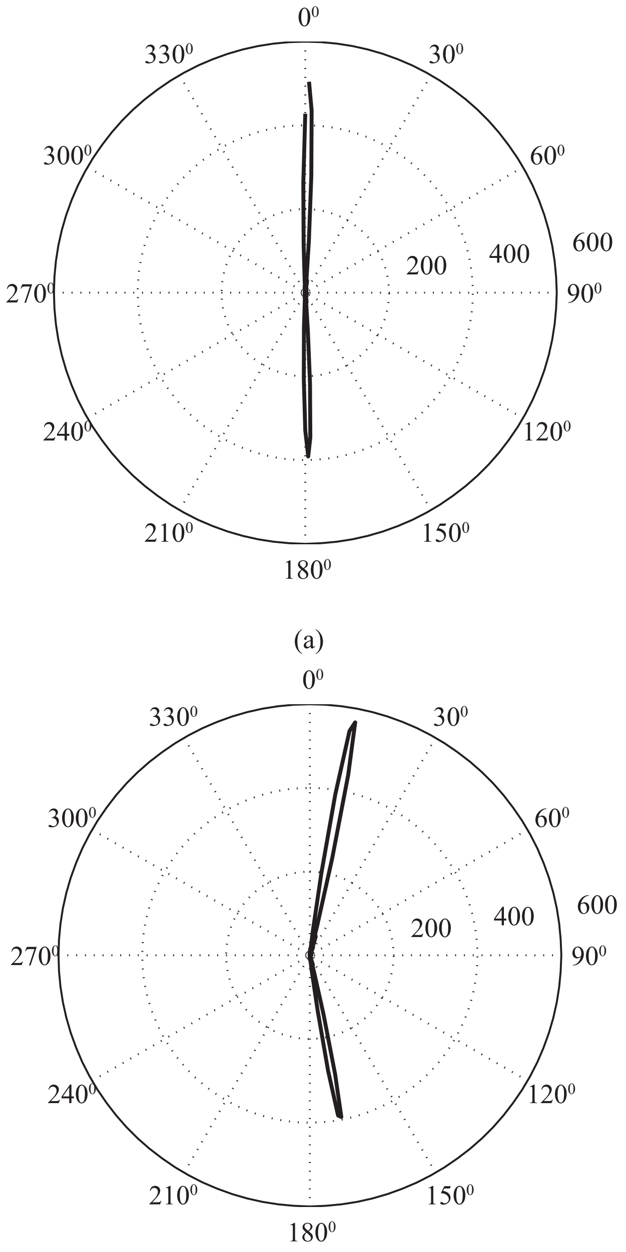

(a)

(b)

Figure 3.5: Far-field directivity plots of 3D focusing grating coupler fabricated by etching method for polar angle θ on $\varphi = 0^\circ$ plane. The grating etching depth is 110nm with effective grating index of 1.7529. (a) Coupler with peak reflection resonance (main lobe directivity 504); (b) Same effective grating coupler index but with tilted radiation angle of $\theta = 0^\circ$ (main lobe directivity 567).

demonstrates that the etching depth decides the effective index of the grating coupler in combination with the tilted angle as shown in equation (3.7). Once the maximum vertical radiation pitch period is optimized for accurate effective index of the grating coupler, the light propagation can be tilted in arbitrary angle just by changing the titled angle in the ellipse equation (3.8) for the new coupler design. The same principle will also be demonstrated in the compact embedded metallic grating coupler design in later chapters.

3.2.3 Impact of etching depth on far-field directivity

For non-optimized etching depth, the loss is even more due to the mode mismatch between the grating coupler and the ridged dielectric waveguide taper as shown by the S_{11} plot in Figure 3.6. The S_{11} parameter describes the energy reflection back to the waveguide source. The higher of S_{11} value, the more mismatch is between waveg-

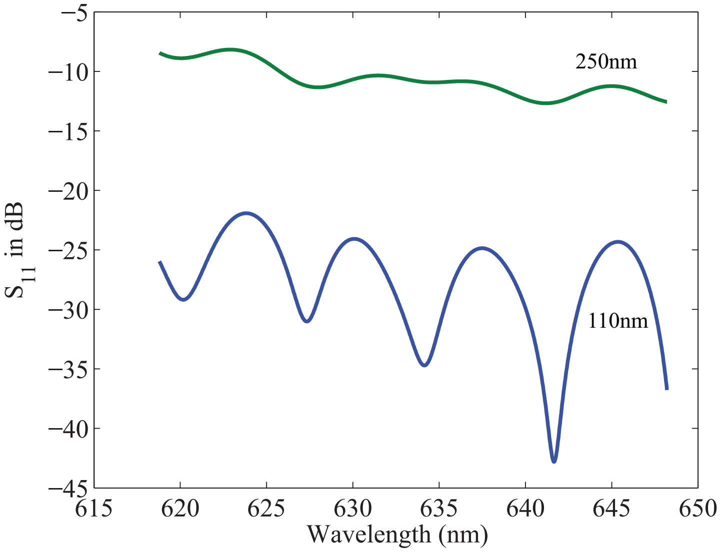

Figure 3.6: The S_{11} of 250nm etching depth (top line) and 110nm etching depth (bottom line) grating couplers.

uide and the optical grating structure. Since there is no special mechanism for blocking the radiation into substrate, almost half of the light energy is lost into the substrate even for the optimized etching depth of 110nm grating coupler design. As shown in the Figure 3.2, the grating etching depth is a very critical parameter that determines the out-of-plane scattering rate. Based on the 3D FDTD modeling, the etching depth also changes coupling efficiency and beam pattern dramatically.

The FDTD simulation of the 80nm (Figure 3.7) and 250nm (Figure 3.8) etching depth for the designed $n_{eff} = 1.7529$ with tilted radiation angle of $\theta_0 = 10^\circ$ futher confirms that the far-field radiation beam pattern and peak directivity strongly depend on the grating etching depth. For 80nm etching depth grating coupler, even there is a peak radiation towards free space at angle $\theta_0 = 13^\circ$, the main lobe is actually pointing towards the substrate direction, which indicates more light scattering loss into the substrate than into the free space direction. For 250nm etching depth grating coupler, due to the impact of the strong mode mismatch, the far-field directivity is not only reduced to <200 level, the direction of the radiation peak is also shifted from the original design for $\theta_0 = 10^\circ$ tilted angle.

3.3 Summary

The main design requirement on the free space grating coupler is to reduce the secondary radiation lobe into the substrate layer for enhanced free space coupling. Based on the CAMFR calculation, under maximal vertical radiation case, the total out-of-plane light coupling is 45% and the free space coupling rate is about slightly more than half of it as estimated from the far-field pattern, if lossless antenna radiation is assumed. So the free space coupling is quite low as compared to that of the embedded

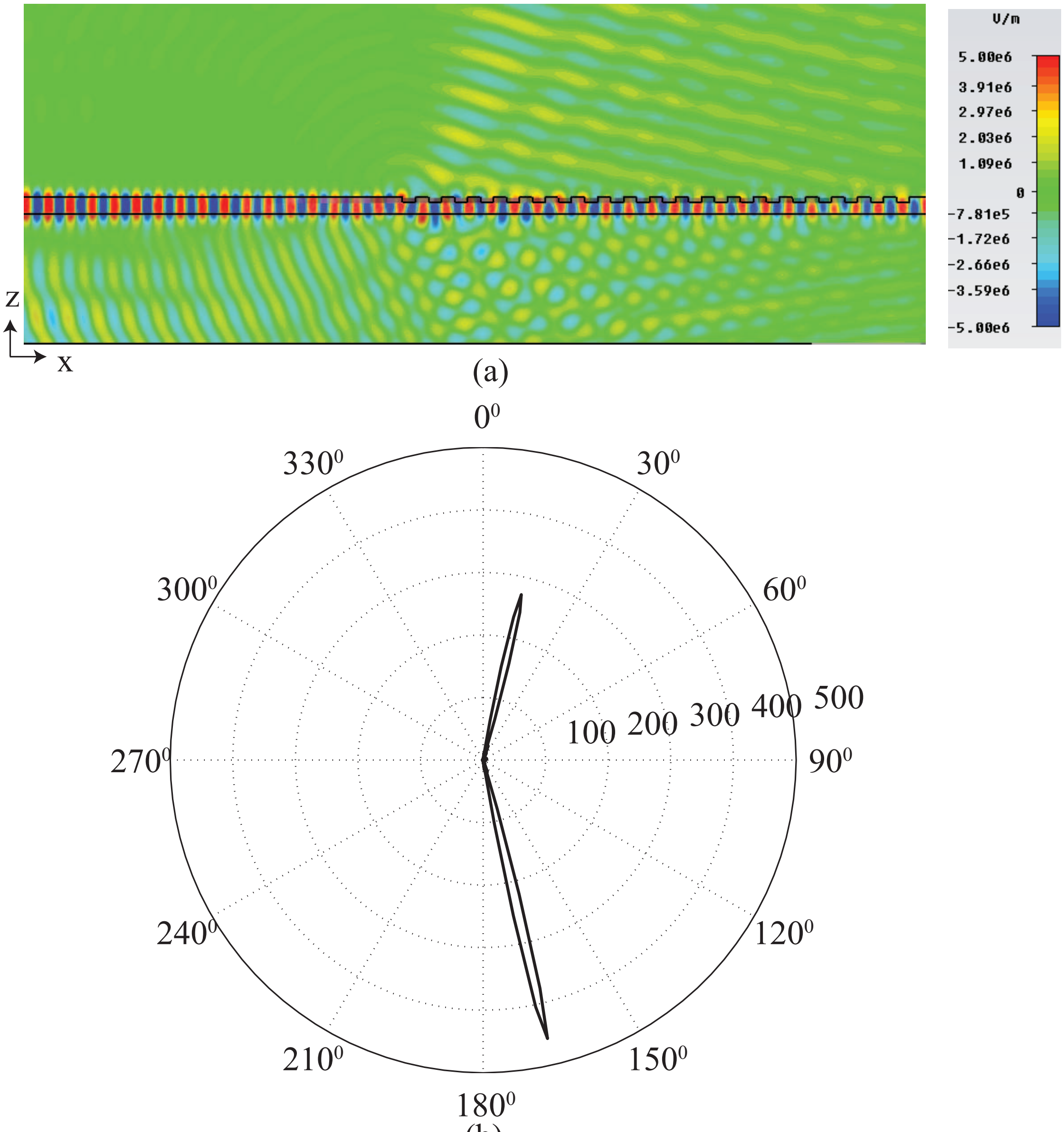

(a)

(b)

Figure 3.7: Etched grating design with same grating pitch as in Figure 3.5 but with 80nm etching depth. (a) E_y component distribution on $y = 0$ plane; (b) Far-field directivity on $\theta = 0°$ plane with main lobe towards substrate (peak directivity 457).

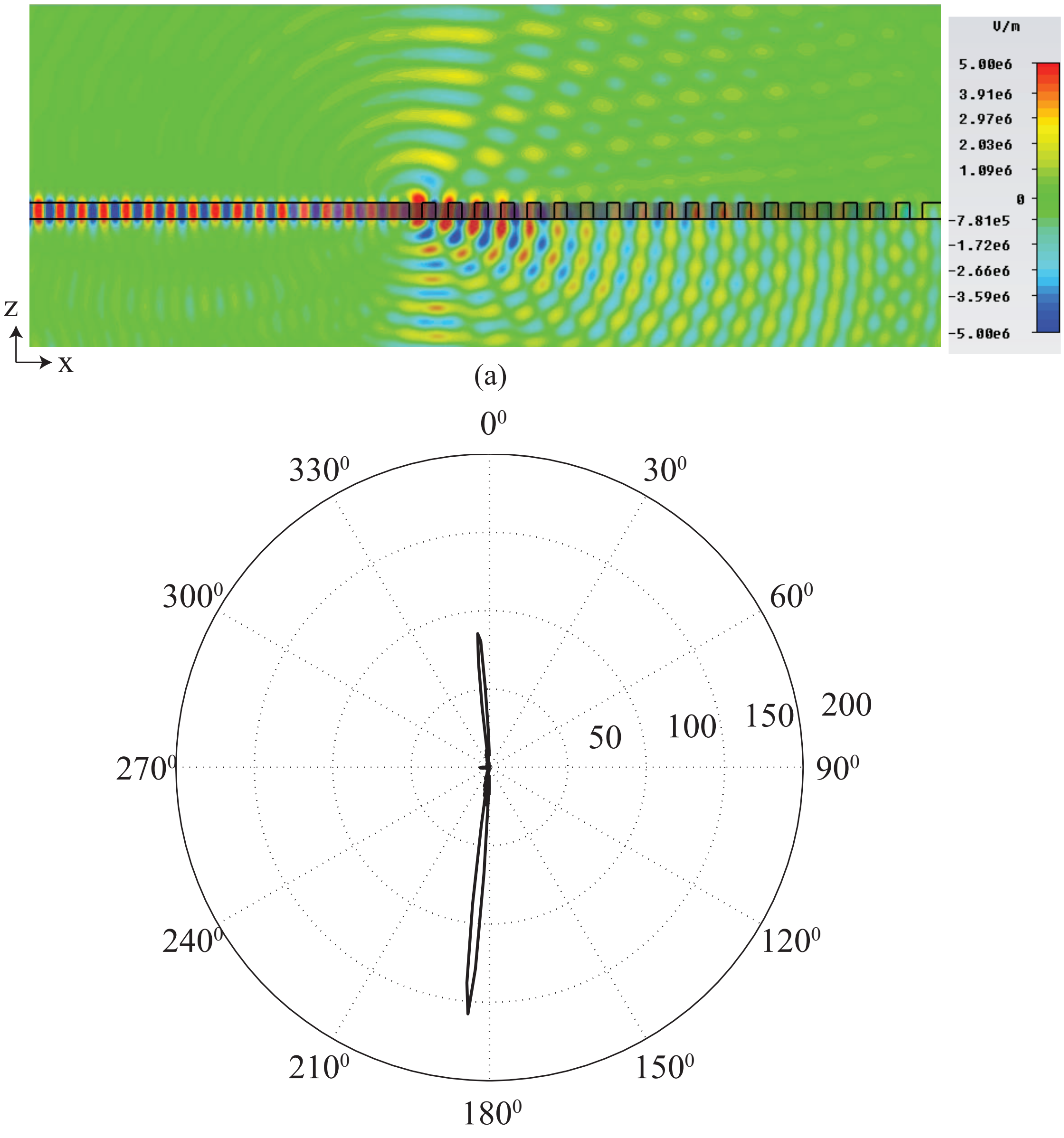

(a)

(b)

Figure 3.8: Etched grating design with same grating pitch as in Figure 3.5 but with 250nm etching depth. (a) E_y component distribution on $y = 0$ plane; (b) Far-field directivity on $\theta_0 = 0°$ plane with main lobe towards substrate (peak directivity 158).

metal ones as shown in later chapters. The main design requirement on the free space grating coupler is to reduce the secondary radiation lobe into the substrate layer for enhanced free space coupling. The reduction of the radiation into the substrate has been realized by introducing a distributed Bragg reflector by stacking multiple oxide layers with precise layer thickness requirement in the substrate layer as that shown in the IR grating coupler design based on SOI platform, but with extra burden on fabrication process [76]. Also as demonstrated in FDTD modeling, the etching depth control is very critical in beam control. But it is difficult to realize precise etching depth since the dry etching in this structure is essentially a non-stopping layer etching process. The only etching depth control parameter is etching time once the etching recipe is fixed. To summarize, Table 3.1 lists the relationships among etching depth, far-field directivity, main lobe directivity angle on $\varphi = 0^\circ$ plane for the designed $n_{eff} = 1.7529$ and tilted angle $\theta_0 = 10^\circ$. It also lists the directivity for the optimized vertical radiation grating. My approach to reduce substrate coupling will be investigated in this doctoral research by embedding the metal grating layer between the waveguide layer and the substrate layer without using the distributed Bragg reflector in the substrate.

Table 3.1: Impact of etching depth on far-field directivity and radiation directions

<table>
<tr><th colspan="5">Design parameters with $n_{eff} = 1.7529$ and $\theta_0 = 10^\circ$</th></tr>
<tr><th>Etching depth</th><th>Main lobe direction</th><th>Directivity main lobe peak</th><th>2^{nd} lobe direction</th><th>Directivity 2^{nd} lobe peak</th></tr>
<tr><td>80 nm</td><td>$\theta_1 = 167^\circ$</td><td>457</td><td>$\theta_2 = 13^\circ$</td><td>271</td></tr>
<tr><td>110nm</td><td>$\theta_1 = 10^\circ$</td><td>567</td><td>$\theta_2 = 169^\circ$</td><td>393</td></tr>
<tr><td>250nm</td><td>$\theta_1 = 185^\circ$</td><td>158</td><td>$\theta_2 = 355^\circ$</td><td>85</td></tr>
<tr><th colspan="5">Design parameters with $n_{eff} = 1.7529$ and $\theta_0 = 0^\circ$ (vertical radiation)</th></tr>
<tr><td>110nm</td><td>$\theta_1 = 0^\circ$</td><td>509</td><td>$\theta_2 = 180^\circ$</td><td>386</td></tr>
</table>

Chapter 4

Design of embedded metallic focus grating coupler

This chapter presents a novel method to solve the high loss problem into the substrate layer in the etched grating coupler design. Noble metals, like silver (Ag) and gold (Au), are used as the active grating material due to its strong index contrast with the waveguide layer. The limited penetration depth in the visible wavelength range explains the low loss into the substrate layer. From the numerical modeling results, optimal grating geometry is quantified through the field distribution and coupling efficiency. There are two sections in this chapter. The first section studies the dispersive optical properties of the two typical noble metals and the material modeling method. Based on the dispersion model of metal dielectric property, the far-field radiation pattern for such coupler is investigated by the peak radiation lobe angle and the peak directivity towards the free space in the second section.

4.1 Noble metal dispersive optical properties

The compatibilities with EBL, stable chemical properties at ambient environment, and low loss make Ag and Au excellent candidates for grating materials at visible wavelengths. For the noble metals, such as Ag and Au, the real part of the permittivity is negative (well less than -10) throughout the visible range, and the imaginary part is only weakly positive [82]. The metallic grating grooves serves as the diffraction element leading to the directional radiation due to its refraction index contrast with that of the waveguide layer material. Also due to the high negative permittivity, the surface plasmonic resonance waves exist on top of the metal surface [83]. Therefore the propagation distance of the waves on the lateral grating plane is greatly restricted which helps reduce the coupler size without the need of a stop grating. The main lobe size in the far-field radiation pattern is also reduced which enhances the far-field directivity. The absorption loss for 632.8nm wavelength for Ag and Au are even smaller due to the smaller loss tangent, as compared to their IR counterparts. The relative permittivities of Ag and Au are modeled as dispersive materials by Drude-Lorentz (DL) model

$$\varepsilon(\omega) = \varepsilon_\infty - \frac{\omega_D^2}{\omega + i\gamma_D\omega} + \sum_n \frac{\sigma_n \cdot \omega_n^2}{\omega_n^2 - \omega^2 - i\omega\gamma_n} \tag{4.1}$$

where ω_D is the plasma frequency, γ_D is the damping term, γ_n represents spectral width, ω_n represents oscillator strength of the Lorentz oscillators, and σ_n stands for weighting factor [84, 85, 86].

The DL model with two Lorentzian terms for both metals is calculated by least-squares nonlinear curve-fitting method with experiment data in [82] for optical wavelength range from 500 nm to 1000 nm which cover the interested wavelength of 632.8nm

Table 4.1: Drude-Lorentz parameters optimized for dispersive dielectric properties of Ag and Au in 500 nm to 1000 nm wavelength range for FDTD modeling.

	ω_∞	$\omega_D/2\pi$ (THz)	$\gamma_D/2\pi$ (THz)	$\omega_1/2\pi$ (THz)	$\gamma_1/2\pi$ (THz)	σ_1	$\omega_2/2\pi$ (THz)	$\gamma_2/2\pi$ (THz)	σ_2
Ag	2.8049	2207	2.28	700.9	10.03	0.1267	1186.7	1634.2	0.5128
Au	5.2518	2089.7	16.07	564.1	103.23	0.1543	654.6	64.53	1.0827

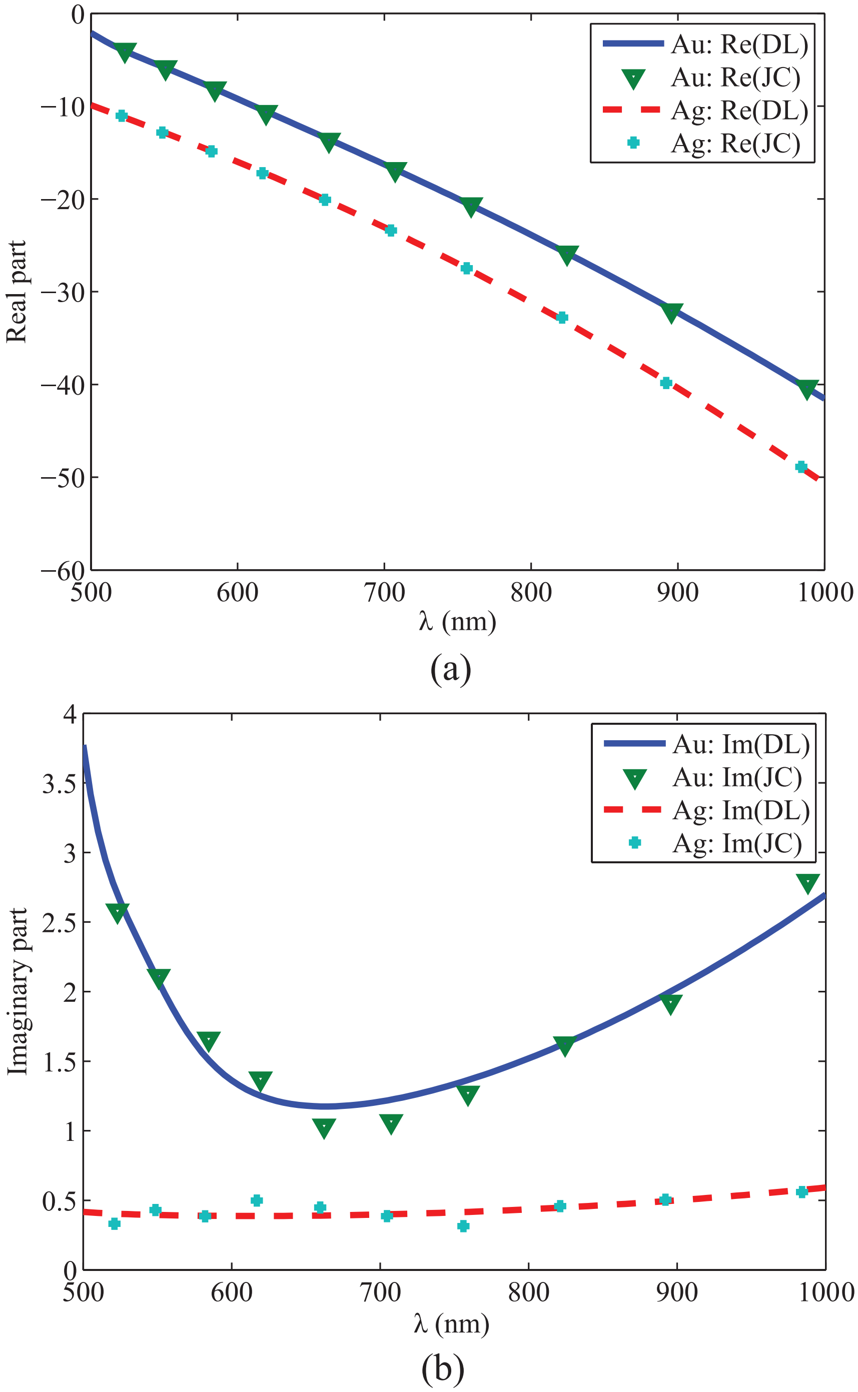

Figure 4.1: Relative permittivity as calculated by Drude-Lorentz (DL) model as compared with the experiment data in [82] by Johnson and Christy (JC) for both Ag and Au for wavelength range from 500 nm to 1000 nm. (a) real part of permittivity; (b) imaginary part permittivity.

as listed in Table 4.1 with data plotted in Figure 4.1. At the wavelength of 632.8nm, the imaginary part of both metals, especially Au, shows minimal value as compared to other wavelengths.

4.2 Compact embedded metallic focus grating coupler

As demonstrated in [57] for IR wavelength, a metal grating can be placed on top of the waveguide layer to form a grating coupler on SOI platform which makes the design fully compatible with CMOS fabrication. However the free space coupling efficiency is greatly related to the buried oxide thickness, since maximum upward coupling only occurs when constructive interference forms between wave reflection from oxide substrate interface and the upward light propagation [57]. In this section, I use 2D and 3D FDTD modeling of the proposed grating coupler to derive the optimal grating design parameters and the 3D far-field directivity.

4.2.1 Compact embedded metallic grating coupler overview

In order to avoid the oxide thickness control restriction, a bottom placed metallic grating coupler is illustrated in 2D vertical cross section view in Figure 4.2(a) and 3D overview of the 3D FDTD model in Figure 4.2(b). A metal grating layer of 40nm is placed on top of the SiO_2 layer with duty cycle of 50%, which can be defined by EBL and fabricated by metal lift-off method. Only one EBL alignment is needed to align the Si_3N_4 waveguide pattern that is finalized by dry etching. Si_3N_4 with thickness of 250nm is chosen to form the single mode (TE_0, E field polarized in y direction) rib waveguide with cross section width of 500nm for its relative high index ($n = 2.02$) and zero absorption loss at 632.8nm wavelength. Other transparent waveguide layer material with

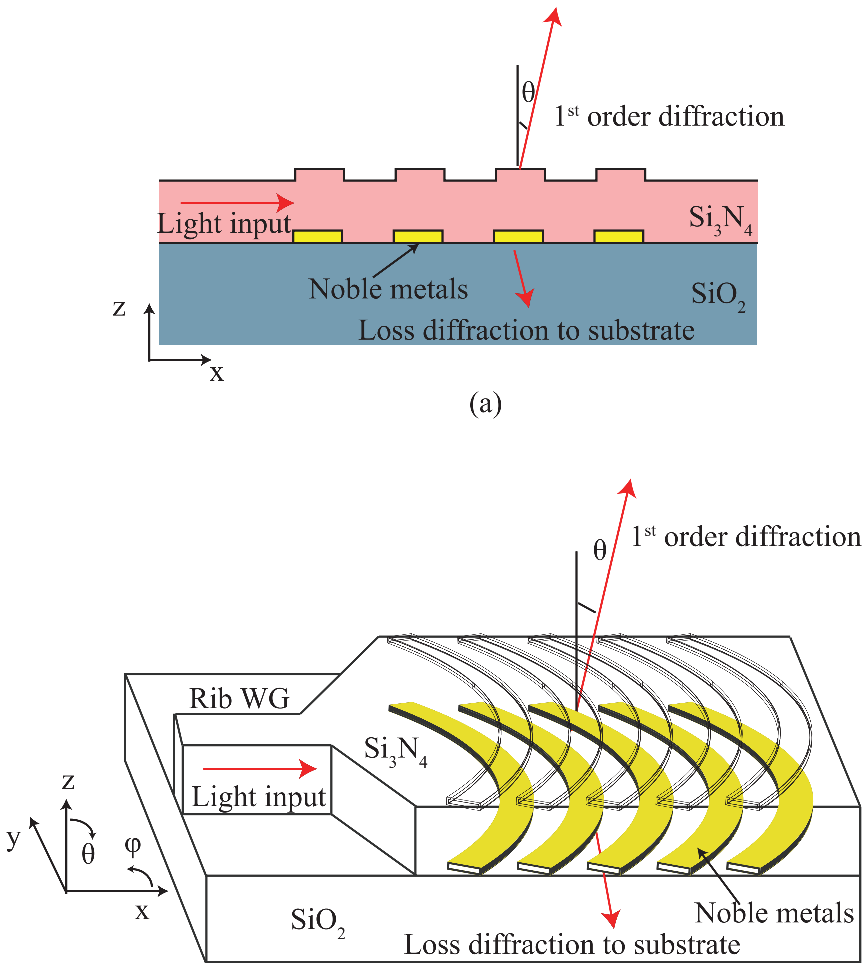

(a)

(b)

Figure 4.2: Noble metal grating on top of the SiO_2 layer for interfacing far-field free space and Si_3N_4 dielectric rib waveguide (geometry not to scale). (a) Vertical cross section view on xz plane where the 1^{st} order diffraction angle is θ from z axis; (b) 3D illustration of the coupler including the metal focus grating ellipses and Si_3N_4 single mode dielectric rib waveguide.

relative high index like Indium Tin Oxide (ITO) can also be used. The non-annealed ITO layer grown by sputtering deposition also provides similar index as Si_3N_4 and low transmission loss. The conducting material property of ITO also alleviates the common charging phenomena in the EBL pattern definition process. The ITO waveguide can also be patterned through lift-off process by using low power ITO sputtering deposition process, instead of dry etching. In this chapter, Si_3N_4 is selected as a modeling norm material due to its zero loss at visible range. Also Si_3N_4 is compatible with silicon fabrication technology and can be deposited by either low pressure chemical vapor deposition (LPCVD) or plasma enhanced chemical vapor deposition (PECVD). The annealing temperature for Si_3N_4 can be achieved at around 800°C [87]. So Ag and Au are compatible with Si_3N_4 deposition since their melting points are 1064°C and 962°C respectively [88]. Also the fused silica can be used as the SiO_2 substrate material for its low thermal expansion and annealing temperature above 1000°C [88]. The bottom placement of the metal layer under the waveguide layer also further enhances the free space light coupling efficiency by reducing the light energy diffracted with higher order modes into the silicon dioxide substrate given by the penetrating properties of such noble metals. The top conformal grooves pattern is also modeled to simulate the uniform conformal Si_3N_4 growth. The top Si_3N_4 conformal grooves does not serve as an active grating element due to its thin thickness and low index contrast.

4.2.2 2D FDTD analysis of the embedded grating coupler

A 2D FDTD model that requires less computing time, other than CAMFR (lossy metal is hard to model with stability problem) or computational intensive and time consuming 3D FDTD, has been implemented to estimate free space coupling efficiency before extending it to the 3D model [89]. In this 2D FDTD model as illustrated in Figure 4.2(a) and also in Figure 4.4(a), a light source of TE_0 waveguide mode is launched from the Si_3N_4 rib waveguide ending at $x = 0$. For each pitch period, FDTD calculations are performed twice to separate the incident and reflected field. The first FDTD calculates field distribution of a simple Si_3N_4 waveguide without grating coupler perturbation

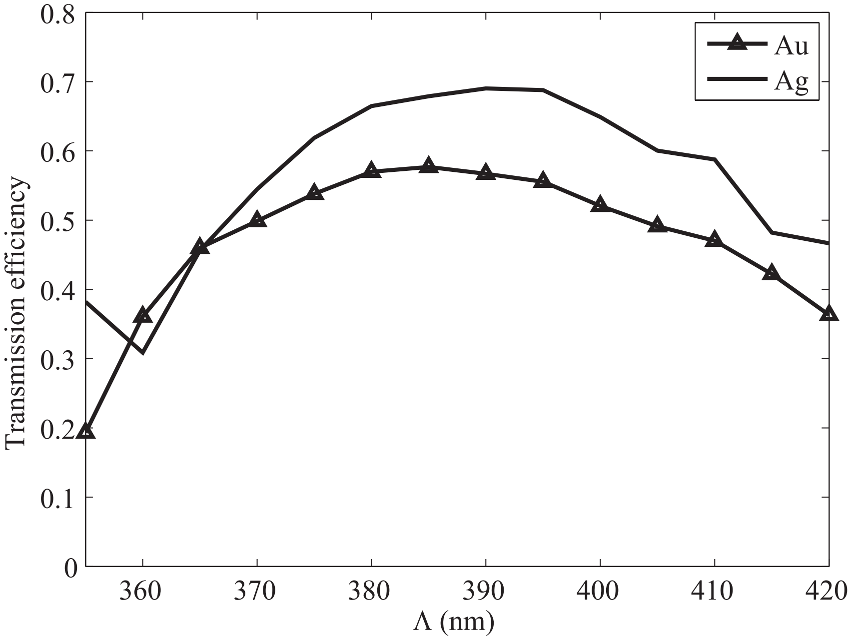

Figure 4.3: Free space transmission efficiencies by sweeping grating pitch period from 355 nm to 420 nm for Au and Ag through 2D FDTD model.

to separate out the incident fields. The second FDTD calculates the field distribution of the grating coupler [18]. The free space transmission efficiency, as shown in Figure 4.3, is calculated using the ratio between flux of electromagnetic energy through 5μm line along x direction at 4μm above the grating coupler center and the incident flux energy at the waveguide input. The 5μm line length in x direction models a typical single mode optical fiber at 632.8nm wavelength, though the 2D FDTD model does not count the coupling loss into the optical fiber. A Gaussian broadband current source with center wavelength at 632.8nm is used as the excitation signal with metal dispersive permittivity property described by the DL model. The flux of the electromagnetic energy is derived from the Fourier transformed field into frequency domain [89]. In this 2D FDTD model, PML layers surround the calculation domain to avoid back reflection error. Since only the total flux across the defined line in x direction is involved in this calculation, the free space transmission efficiency only quantifies the energy flux without taking account of the directional radiation information. The directional radiation pattern will be quantified through far-field directivity by the 3D FDTD model. The Ag grating and the Au grating give peak free space coupling efficiencies of 68% and 55% respectively. The free space coupling for both metals grating couplers are much higher than those of the etched grating coupler with the same waveguide layer material. The smaller loss tangent of Ag explains the higher transmission rate than that of the Au one. The higher transmission rate for Ag grating is also demonstrated by the higher free space radiation directivity calculation in the following 3D FDTD simulation.

4.2.3 Far-field radiation patterns

To verify the field distribution and far-field radiation pattern, a 3D FDTD model is carried out in this research and one term DL model has been used to simplify the 3D model [81]. Based on optical antenna radiation theory, the far-field directivity radiation pattern, combined with antenna radiation efficiency, can be used to quantify both the beam pattern and the transmission efficiency within certain angle range. In this section the 3D radiation patterns in terms of far-field directivity for both Au and Ag grating material are quantified by 3D FDTD simulation to reveal the focusing and enhanced directivity properties of such embedded metal focus grating coupler.

The design of the grating coupler needs to achieve two aims, efficient light coupling and compact coupler size. Also the size of the grating coupler needs to match that of the free space source or detector for maximal coupling efficiency. At the cross section plane of $y = 0$, the elliptical grating pitch period is a constant as defined in the 2D FDTD model. The effective index of the Si_3N_4 dielectric waveguide can be calculated from equation (3.6). Following similar design ideology as the etched grating coupler for compact focusing on xy center plane at the waveguide layer, equation (3.8) can be further expanded in elliptical curve form as follows

$$\frac{\left(x-\frac{q\lambda n_0\sin^2\theta_0}{n_{eff}^2-n_0^2\sin^2\theta_1}\right)^2}{\left(\frac{q\lambda n_{eff}}{n_{eff}^2-n_0^2\sin^2\theta_1}\right)^2}+\frac{y^2}{\frac{q\lambda}{\sqrt{n_{eff}^2-n_0^2\sin^2\theta_1}}}=1 \tag{4.2}$$

to design the embedded metallic grating coupler. Equation (4.2) describes a set of ellipses that share a common focal point at $(0,0)$ on xy plane. By fixing the grating pitch period and the diffraction angle in free space, the focus grating curves can be exactly determined. The size of the grating coupler is determined by the starting grating number of q, and can be adjusted for different free space source size or detector size. To achieve focusing effects on xy plane, the Si_3N_4 waveguide ending facet needs to be positioned at the focal point of the ellipse curves.

The size of the focusing grating coupler is set as 10μm in y direction with 20 grating grooves of 50% duty cycle and the distance from the nearest grating line center to the waveguide is set as 7μm to cover the optical fiber ending facet size. An E_y waveguide port current source with broad wavelength range of center wavelength at 632.8nm is modeled as the excitation source for the 3D structure. The surrounding boundaries of the calculation domain are set as open absorbing boundary condition. And the E_y field distribution are plotted in Figure 4.4, based on the 3D FDTD simulation results of Au focusing grating coupler with center pitch period of Λ_p = 397.5nm. The center pitch period in 3D FDTD model is chosen by optimizing the directional radiation angle at $\theta_0 = 10^\circ$. Figure 4.4(a) demonstrates the directional radiation along the 10° tilt direction as designed. Shown in Figure 4.4(b), the light exit from the waveguide facet has matched wave front that collides with the grating curvatures on the lateral center plane which

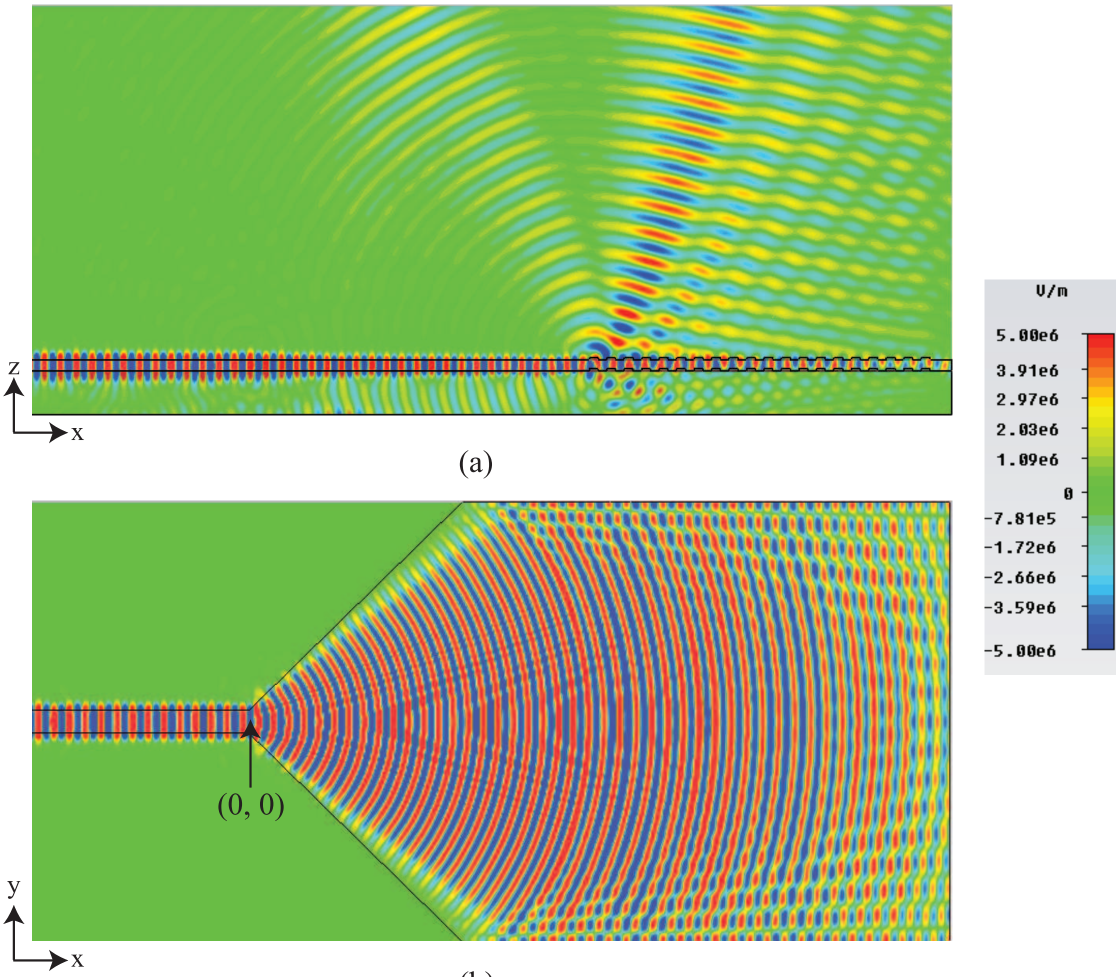

(a)

(b)

Figure 4.4: E_y field plots of an optimized Au focusing grating coupler excited by 632.8nm TE_0 waveguide source on the center cross section planes of the coupler. (a) Field plot on xz center plane; (b) Field plot on xy plane along the Si_3N_4 slab center. The focusing point at $(0,0)$ on xy plane is as indicated. Grating pitch period $\Lambda = 397.5$nm, thickness of Au layer = 40nm, Si_3N_4 waveguide layer thickness = 250nm.

greatly reduces the impedance mismatch loss. The Ag grating coupler has similar field distribution but with slightly higher field intensity in the free space direction radiation which will be demonstrated in the following far-field distribution patterns discussion.

To quantify the radiation difference, the 3D far-field radiation pattern is derived from near to far-field conversion for these two materials as shown in Figure 4.5. The effective refraction indexes of Ag and Au grating coupler are 1.7711 (397.5nm center pitch) and 1.7611 (400nm center pitch) respectively for optimized directional radiation for the 1st order diffraction angle $\theta_0 = 10^\circ$. The far-field radiation pattern shows strong directional angular radiation pattern oriented in $\theta_0 = 10^\circ$ for 1st diffraction angle. The pitch period for peak free space coupling as calculated by 2D FDTD model is not used for the 3D FDTD model due to the fact that 2D FDTD does not take account of the directional radiation information. Thus correspondingly the 2D free space coupling efficiencies for the 3D designs are reduced to be 65% and 50% for Ag and Au respectively as read from Figure 4.3. As expected, there is also a side lobe pointing towards the substrate layer which counts for the light coupling loss but with much smaller magnitude as compared to the etched one. The peak free space directivity is also greatly increased for both metallic grating designs. This phenomenon also echoes with the initial design discussion for bottom placement of the metallic grating. The radiation intensity difference is not apparent as shown in the directivity plot in Figure 9(c) due to the dBi unit used. However both grating structures show a 4.2° 3dB angular width for the main lobe radiation pattern. On the other hand the total radiation efficiencies for the Ag and Au grating coupler are 85% and 75% respectively, which also explains the lower transmission efficiency for Au grating coupler design due to high loss tangent for Au material. From radiation antenna point of view, this kind of far radiation pattern corresponds to the super high gain or directivity antenna, which is suitable for directional light coupling or detection with minimal sway light loss.

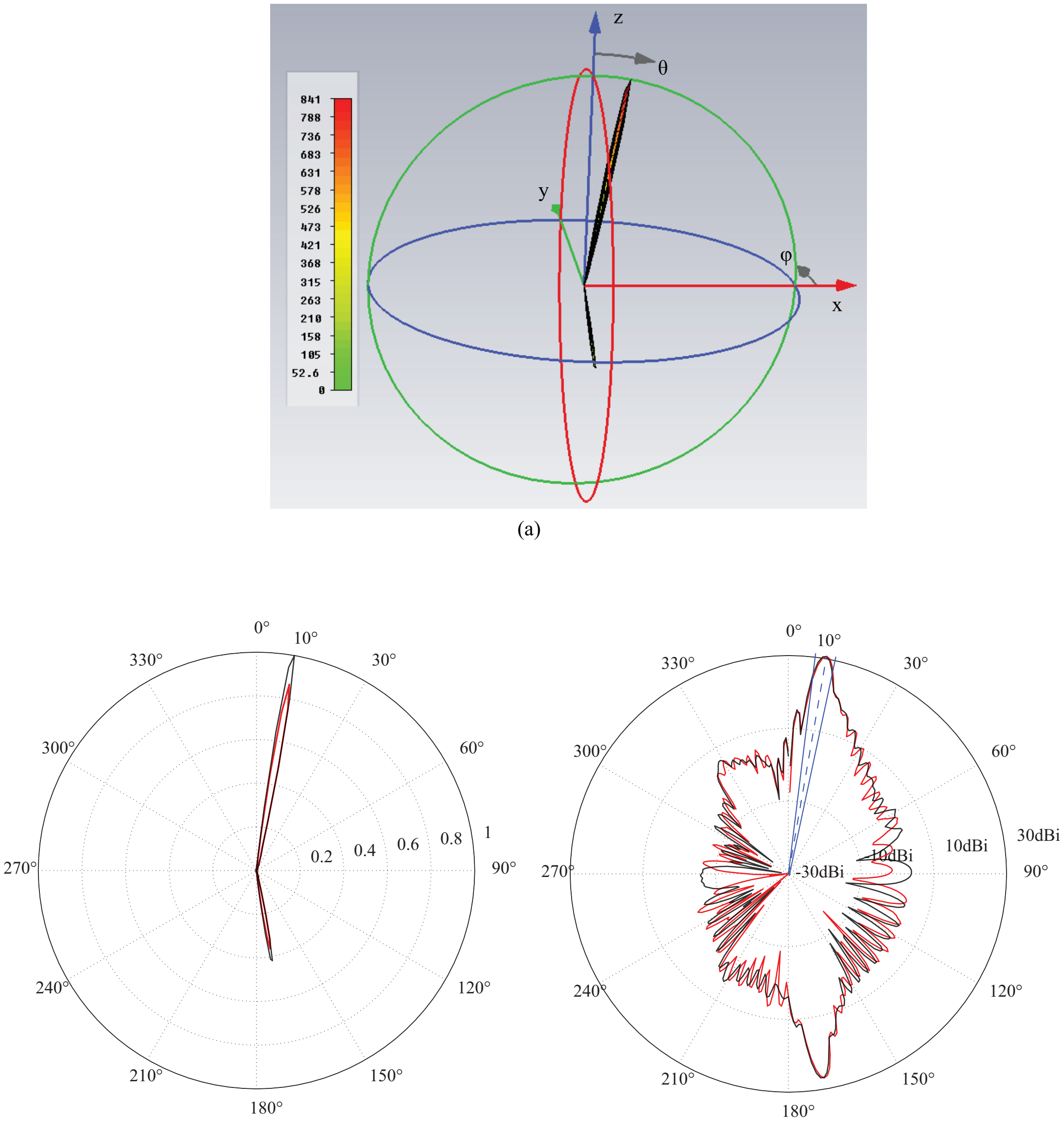

(a)

(b)

(c)

Figure 4.5: Far-field radiation pattern for incident waveguide source light at wavelength 632.8nm. (a) 3D directivity pattern as functions of spherical angles for Ag grating coupler with peak directivity of 841; (b) Normalized far-field power radiation pattern as function of θ on $\varphi = 0^\circ$ plane; (c) Far-field directivity as function of θ on $\varphi = 0^\circ$ plane in unit of dBi. The black curve represents Ag grating and red one is for Au grating.

4.2.4 High tilted radiation angle analysis

In order to test the design accuracy, a 3D FDTD simulation with changed design radiation angle $\theta_0 = 25^\circ$ is implemented for Au grating coupler. The equation (3.7) is only valid by assuming equal effective index in the grating region and the waveguide region, and it is only fulfilled for shallow gratings less than 50nm [77]. The metal grating grooves only has 40nm thickness which can be regarded as shallow grating. As it is observed from equation (3.6), by finding out the effective index of the grating coupler at $\theta_0 = 10^\circ$ and simplifying it as a constant for all radiation angles, the optimized grating pitch period for $\theta_0 = 25^\circ$ peak radiation is only related to the designed radiation angle. By calculating the model using the updated grating pitch period, the 3D compact metallic focus grating ellipses can also be uniquely derived for new 1^{st} order diffraction angle. Thus the effective index of the grating coupler is a very important parameter for grating coupler design to control main lobe radiation angle. Figure 4.6 shows the radiation pattern for $\theta_0 = 25^\circ$ with exact same effective index estimation as $\theta_0 = 10^\circ$ for Au grating coupler. The high 1^{st} order diffraction angle enables longer light propagation distance on top of the grating grooves, which explains slightly higher material loss. The total radiation efficiency only reduces slightly to 73% for $\theta_0 = 25^\circ$ case, but the free space directivity is greatly enhanced with strongly suppressed side lobe towards substrate. The side lobe for $\theta_0 = 25^\circ$ towards the substrate is only half of the lower diffraction angle case. And the main lobe towards the free space is enhanced to 1200. The side lobe is generated from the light leakage into substrate and regulated by the metallic grating. The magnitude of the side lobe is strongly dependent on the penetration depth of the evanescent wave on top of the metal layer. The electric field of light reaches $1/e$ of its maximum value on the metal surface at the penetration depth that is defined

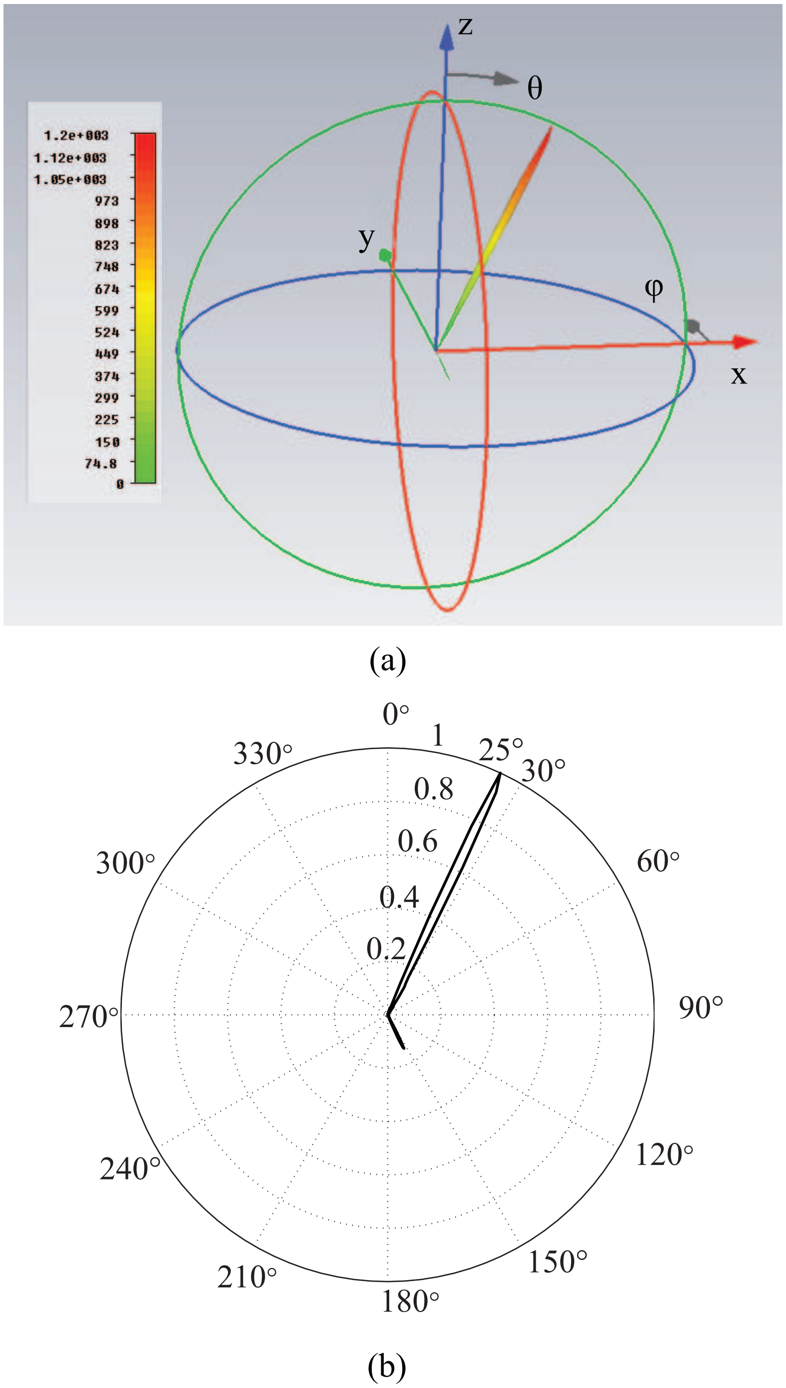

(a)

(b)

Figure 4.6: Far-field radiation pattern for 1st diffraction angle of $\theta_0 = 25^\circ$ with same effective index estimation as Figure 4.5 for Au material. (a) 3D directivity pattern as functions of spherical angles for Au grating coupler with peak directivity of 1200; (b) Normalized far-field power radiation pattern as function of θ on $\varphi = 0^\circ$ plane.

as [90]

$$d(\theta_0) = \frac{\lambda_0}{2\pi\sqrt{n_m^2 \sin^2\theta_0 - 1}} \tag{4.3}$$

where λ_0 is wavelength of the light, n_m is the refraction index of metal, and θ_0 is the light incident angle. As it shows in equation (4.3) , the penetration depth of light reduces for higher incident angle, which causes less light propagating through metal layer and lowers the side lobe magnitude for the directivity far-field pattern. Even though most grating coupler designs including the one in this contribution choose the near vertical 1st order diffraction angle to avoid the possible secondary reflection, the proposed embedded metallic grating design has unique advantage of better free space transmission for higher radiation angle. The Ag grating design for $\theta_0 = 25°$ with n_{eff}=1.7711 has much higher free space gain as listed in Table 4.2 due to its lower material loss rate, though the directivity of it has slightly less value as that of the Au one. And the 2nd directivity main lobe of Ag grating coupler with $\theta_0 = 25°$ is only one third of the $\theta_0 = 10°$ Ag grating coupler.

4.2.5 Light focusing effects

The previous sections study the light out-coupling from the waveguide since it is easier to calculate the maximal light coupling angle and the far-field free space directivity. To demonstrate the compact focusing effects, it is insightful to calculate the field intensity inside the dielectric waveguide by the external excitation of a plane wave source with TE polarization. It is essentially an equivalent problem to calculate light coupling from the free space into the dielectric waveguide in terms of the coupling efficiency based on the reciprocity theorem that has been proved mathematically by using Maxwell's equations [91]. As illustrated in Figure 4.7, a plane wave source with poynt-

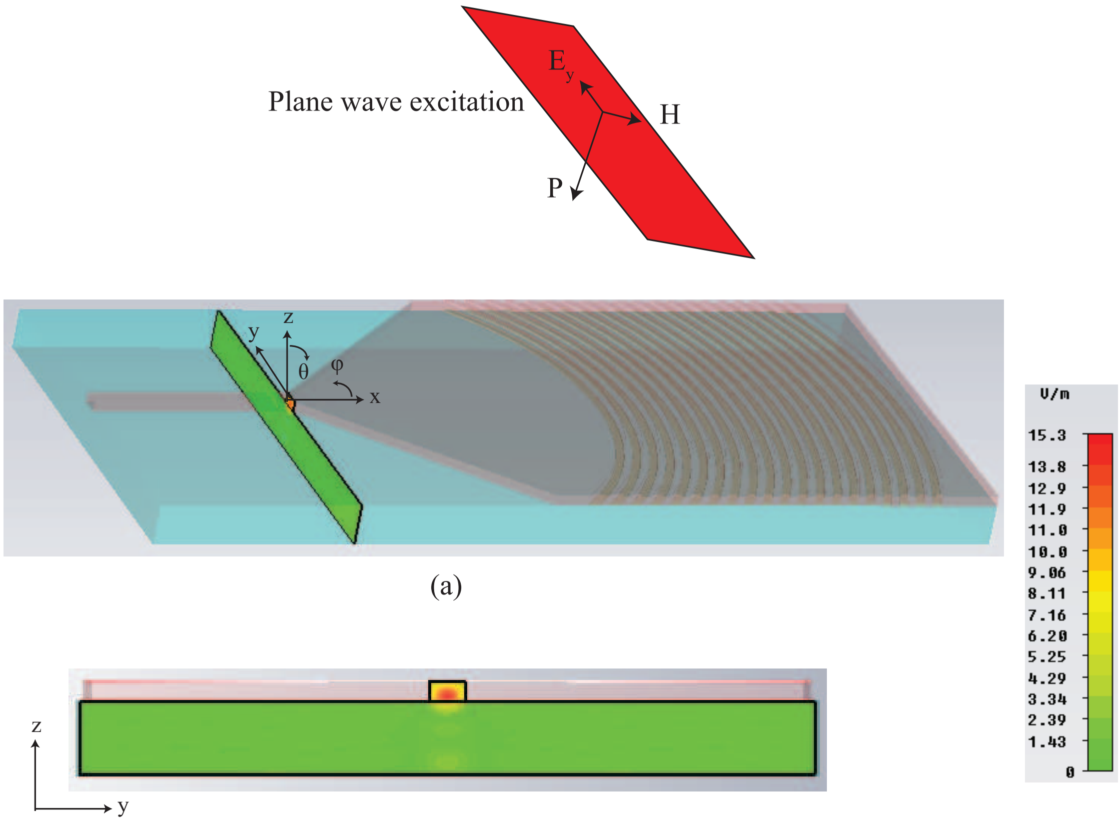

(a)

(b)

Figure 4.7: Plane wave excitation on the embedded metallic grating coupler. (a) TE mode excitation with tilted poynting vector ($\theta_0 = 10°$) illustrated in 3D; (b) 2D surface plot of the electric field amplitude on $x = 0$ cross plane with $\theta_0 = 10°$.

ing vector of $\boldsymbol{P} = -\sin\theta_0 \cdot \boldsymbol{x} - \cos\theta_0 \cdot \boldsymbol{z}$ covers the whole simulation domain that contains the grating coupler assuming actual laser beam spot size is much bigger than the coupler size. For typical linearly polarized laser source, the focused beam spot size is well above 700μm in diameter. Enough PMLs surround the simulation domain to minimize back reflection errors. A unit $|E_y|_{max} = 1$V/m is assumed for the plane wave source. A single mode light with TE$_0$ mode is found to confine and focus on the dielectric rib waveguide end facet with minimal impedance mismatch. For the tilted angle of $\theta_0 = 10°$, the center peak electric component amplitude of $|E_y|_{max}$ at the waveguide facet at $x = 0$ enhances

15.3 times with that of the plane wave source. In terms of light intensity, the light intensity enhances $|E_y|^2_{max} = 234.09$ times of the incident plane wave light source. The grating coupler design of $\theta_0 = 25^\circ$ has also been calculated with plane wave source tilted at $\theta_0 = 25^\circ$ under the same plane wave intensity to find slightly higher 16.8 times enhancement of the $|E_y|$ component. Thus the corresponding light intensity enhancement factor is 282.24 for $\theta_0 = 25^\circ$ grating coupler. The higher tilted angle design as mentioned in last section has higher free space directivity which also explains the higher focused light intensity. Due to the calculation time and computer memory requirement lengthens in 8 times with the calculation domain size enlargement, larger size grating coupler is not simulated. For larger size of the grating coupler, more light energy will be collected from the plane wave source and focused onto the dielectric waveguide.

4.3 Summary

By embedding the metallic grating layer between the waveguide layer and the substrate, a novel visible light grating coupler has been proposed and analyzed in this chapter that demonstrates the higher free space directivity without artificially manipulating the substrate optical properties. The metallic grating layer provides a light penetrating barrier to limit the light energy loss into the substrate. Due to the surface plamonic effects on the metal material, light propagation distance is greatly restricted and there is no need to place a stopping grating part as found in the etched grating coupler designs in IR wavelength range. The Ag and Au show minimal material light absorption at visible wavelength. Even there are some material loss and reduction of radiation efficiency up to 10% compared to that of the etched grating coupler design, the embedded metallic ones show much higher free space directivity enhancement and overall much higher free space coupling efficiency. Table 4.2 lists the radiation efficiency, optical antenna gain, effective grating index and radiation angle design parameter as analyzed in this chapter.

The embedded metallic grating couplers not only can out-couple light into free space with high directivity, but provide a way to focus free space angular plane wave source into the single mode light spot that can be fed into the dielectric rib waveguide for further light processing. The single mode light source size, however, is still not in extreme subwavelength scale. Thus more light processing steps need to be done to realize deep subwavelength light focusing especially at the near-field of the probe tip. I propose a novel light processing device based on PhC nano slot resonator technology in the following chapter. Combined with the enhancement factor by the PhC nano slot resonator for near-field light enhancement, the total light enhancement factor has enormous improvement compared with that of the pulled metal coated optical fiber probe tip design.

Table 4.2: Embedded metallic grating coupler performance list

Waveguide port excitation

Metal	n_{eff}	Main lobe direction θ_0	Radiation efficiency	Directivity main lobe peak	Gain of main lobe	2^{nd} lobe direction θ_2	Gain of the 2^{nd} lobe peak
Ag	1.7711	10°	0.86	841	723	170°	303
Au	1.7611	10°	0.75	792	598	170°	254
Ag	1.7711	25°	0.84	1174	988	155°	111
Au	1.7611	25°	0.73	1198	876	154°	123

Plane wave excitation

Metal	n_{eff}	$\boldsymbol{P}$ direction in θ_0	$\lvert E_y \rvert_{max}$ enhancement factor	Light intensity peak enhancement factor
Au	1.7611	10°	15.3	234.09
Au	1.7611	25°	16.8	282.24

Chapter 5

Design of photonic crystal waveguides for near-field light focusing

In this chapter the concept of slotted PhC nano-resonator based probe tip is proposed and analyzed by 2D and 3D FDTD method. As discussed in the introduction chapter and the device design approach chapter (chapter 2), the conventional metal coated based probe tip has heating damage effect due to light absorption by metal. Also the metal-dielectric structure needs manual assembly to achieve certain plasmonic based light confinement. Though the metallic material can be implemented in the relative large area of the grating coupler and has relative larger heat dissipating area, it is hard to be justified on probe tip design due to much stronger light focusing on nanometer scale spot which would cause strong heating damage to the nanometer structure that severely changes the optical properties of the probe design. My approach to this problem is to avoid metal as light confinement mechanism in the nanometer confinement space. And the structure of the probe tip is fully compatible with planar Si micro- or nano-machining and CMOS fabrication technology. Light propagates through the well impedance matched PhC light processing network composed of nano slot and nano resonator to confine light in subwavelength scale. The light throughput enhancement is achieved by nano light resonator. The PhC material supports the light confinement in the lateral plane with minimal light penetration, unlike some optical fiber based tip in which strong impedance mismatch due to metal Ohmic loss severely lowers excitation intensity of the tip based optical antenna structure. Both a center placed nano resonator formed by shrunk air hole evenly distributed aside the center line defect and a $\lambda/4$ slot monopole optical antenna based resonator at the probe tip are analyzed in detail in this chapter. It is found enormous light throughput can be realized by pure dielectric material in the near-field of the probe tip and still confined in the <50nm size for $\lambda_0 = 632.8$nm.

5.1 Fabry-Pérot resonator based photonic crystal

In this section a nano resonator formed by placing shrunk air holes aside the center slot is analyzed by 3D PBG diagram and 2D FDTD method for near-field light confinement. By 3D PBG calculation, the lattice constant for low loss light transmission through PhC waveguide is optimized. The 2D FDTD modeling of the probe tip structure is implemented to solve the light distribution both inside the probe body and at the near-field of the probe tip. Subwavelength light confinement size is demonstrated to have a proportional relationship with the slot width. And so is the light throughput. Even the smallest 15nm slot width design shows much higher throughput than that of the metal coated pulled fiber based light confinement probe tip.

5.1.1 Photonic band gap diagram

The slotted PhC waveguide is designed to propagate the TE mode light and still strongly confine the light within the air slot. In order to find the optimal slotted PhC waveguide design parameters, such as lattice constant, the center defect size and the slot width, the PBG diagram of the slotted PhC waveguide needs to be obtained in order to find the guided mode. Fully-vectorial eigenmodes of Maxwell's equations with periodic boundary conditions were computed by preconditioned conjugate-gradient minimization of the block Rayleigh quotient in a planewave basis, using a freely available software package MIT Photonic-Bands (MPB) [20].

Not like the 2D infinite PhC waveguide, the exact mode nomenclature is no longer valid for the 2D slab PhC waveguide [92]. Thus the light polarization is better defined as z-even modes as the H_z is symmetric along z direction. From the band diagram of Figure 5.1(c), the guided modes should be within the PBG, below the light line, and above the slab modes. The group velocity $v_g = \frac{d\omega}{dk}$ should be positive for the guided mode. Thus even there are two guided modes (mode 13 and 14) in the PBG, only guided mode 14 is used, due to its positive group velocity. At the first Brillouin zone edge for $k_x = 0.5\frac{2\pi}{a}$, the v_g is zero, due to the symmetric band diagram at the Brillouin zone edge. Thus it is not appropriate to choose the guided mode point at the edge. The guided mode of the slotted PhC waveguide gives the lattice constant of $a = 0.3568\lambda_0 = 227$nm, bulk air hole radius $r = 0.3a = 68$nm, slot width $0.2a = 45$nm, and side ridge size $0.91a = 206$nm. Also from Figure 5.1(a), the guided mode has a center peak at the slot region and side lobes in the side ridge region. The light distribution is well confined in the vertical direction within the optimal slab thickness of $1.2a$ due to the total internal reflection (TIR) as shown in Figure 5.1(b) [93].

5.1.2 Probe tip without nano-resonator

Since the H_z distribution is derived from the frequency mode method, the more accurate light distribution needs to be verified by FDTD method. Simulations were performed with the FDTD method [18], using a freely available software package with subpixel smoothing for increased accuracy [89, 94]. The geometry of the slotted PhC waveguide is strictly derived from the MPB calculated design parameters at $\lambda_0 = 632.8$nm as shown in Figure 5.2. The light propagation has loss with side peaks along the slotted

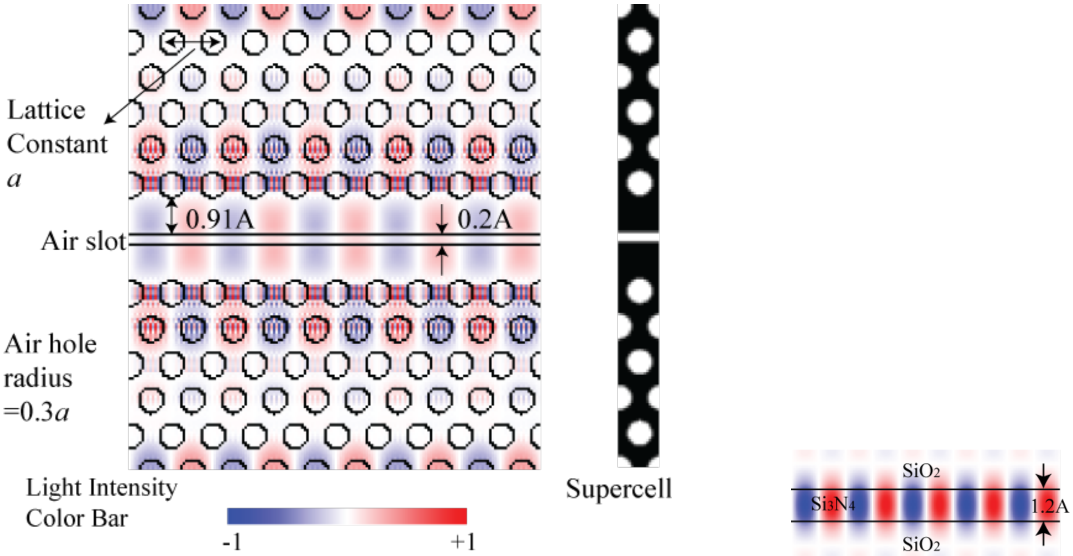

(a) H_z distribution on xy center cross section plane.

(b) H_z distribution on xz center cross section plane.

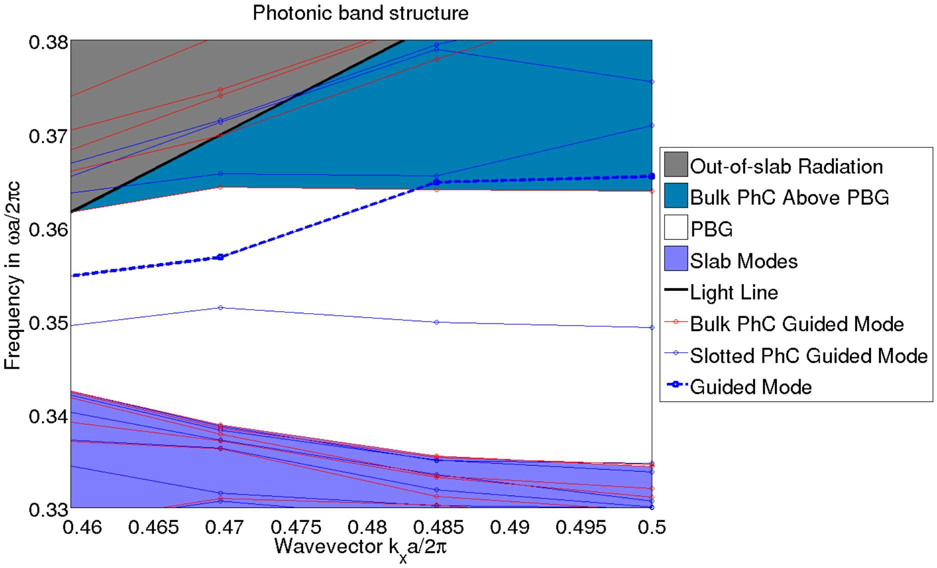

(c) H_z distribution on xz center cross section plane.

Figure 5.1: PBG diagram by MPB method. H_z distribution on (a) xy center cross section plane (b) xz center cross section plane by 3D supercell MPB calculation for z-even mode 14 of the slotted PhC waveguide at the first Brillouin zone edge for $k_x = 0.5(2\pi/a)$ [92]. The supercell display is extended for 10 period along the waveguide direction ΓK direction for better illustration. (c) The PBG diagram of the slotted PhC waveguide. The guided mode locates within the PBG, and below the light line, and above the slab modes. Also the group velocity of the guided mode should be positive.

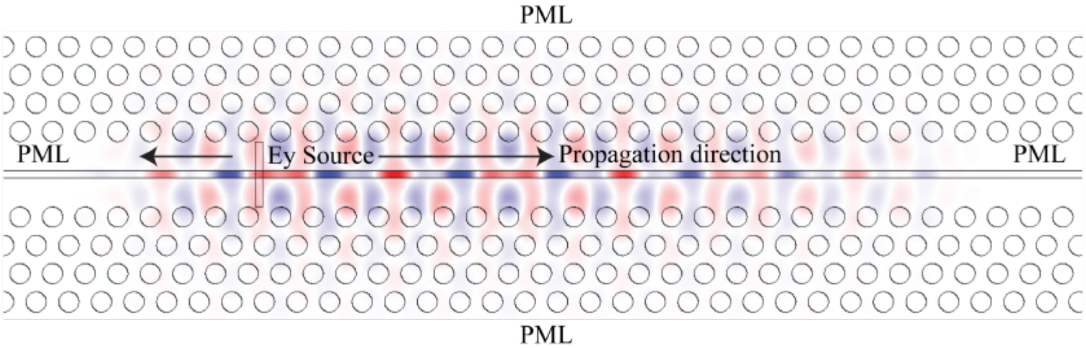

(a) E_y distribution

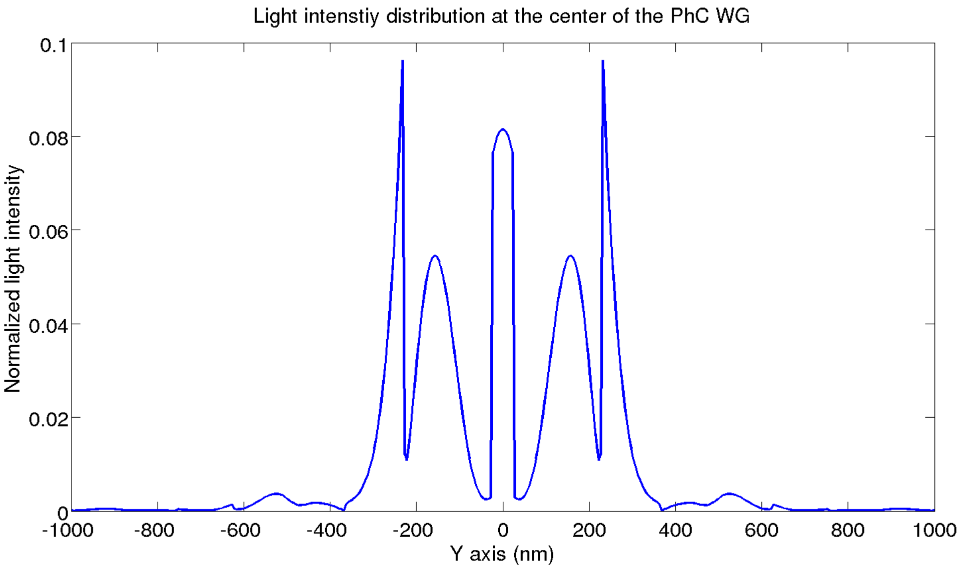

(b) $|E_y|^2_{max}$ distribution at the slotted PhC waveguide center

Figure 5.2: FDTD model of the straight slotted PhC wavguide. (a) 2D FDTD modelling result for the E_y distribution along the center cross section on xy plane for the slotted 2D slab PhC waveguide with PML boundary layers around the calculation cell. The continuous unit source is located at where it is indicated in the plot. (b) $|E_y|^2_{max}$ distribution at the slotted PhC waveguide center along y direction.

slab PhC waveguide at the guided mode as derived from the MPB calculated PBG diagram. But the center peak can be located at the center slot. The side peaks correspond to the MPB band diagram results of mode 14 as in Figure 5.1 (a). Because mode 13, which is a non-guided mode, is too close to mode 14, it is hard to separate the two numerically. Thus it causes propagation loss and strong side peaks. Also since the Si_3N_4 material has lower refraction index, it is difficult to design non-loss PhC waveguide. In order to compensate the propagation loss, the length of the slot PhC waveguide should be within a reasonable range, and nano resonators needs to be incorporated to reduce the light throughput loss as discussed in the next section. Before continuing onto the next section, it is interesting to show the light distribution with simple straight slotted PhC waveguide 120° tip cut along the ΓK direction with air interface without incorporating any nano resonators as shown in Figure 5.3 as a reference structure.

The mode transition adapter will convert the light from the 3 lines defect (3W) ridged waveguide into the slotted PhC waveguide as illustrated in the Figure 5.3(a). It was demonstrated that the coupling efficiency from the ridged waveguide to the slotted PhC waveguide when the phase difference changed by the adapter in the propagating direction is about π. This also means the mode transition adapter length should be half wavelength in the propagating medium [95]. This kind of mode transition adapter design avoids the long tapered mode transition adapter.

However it also increases the resonances around the adapter as it can be observed in Figure 5.3(b). But in this research the mode transition adapter design is not a main point and the resonance at the slotted PhC waveguide entrance will not harm the overall performance of the proposed probe design. Also later in this chapter, the resonance at the slot entrance concept will be used to design $\lambda/4$ monopole optical antenna structure.

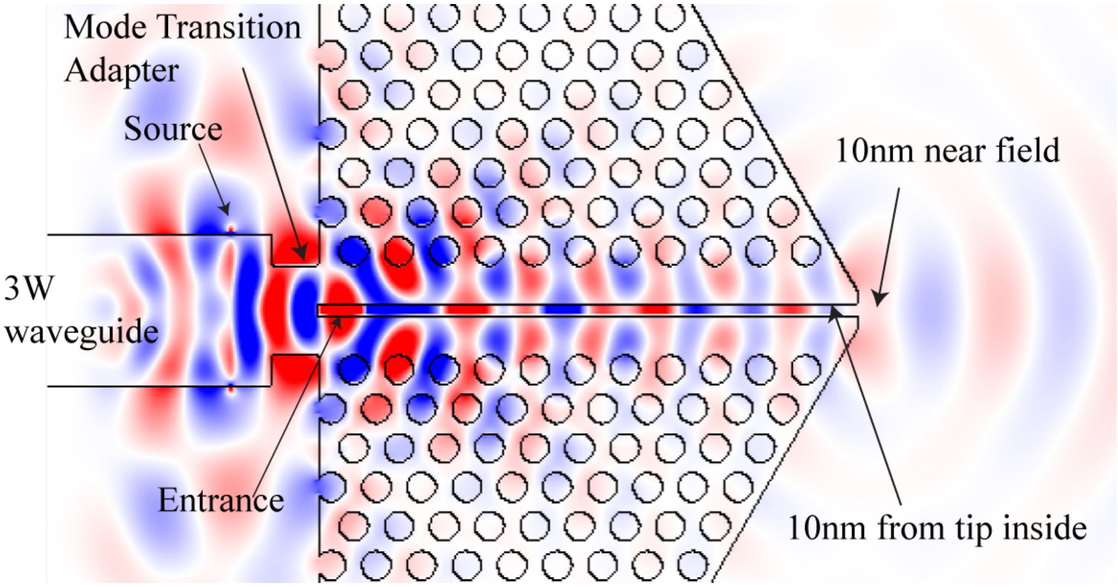

(a) E_y distribution

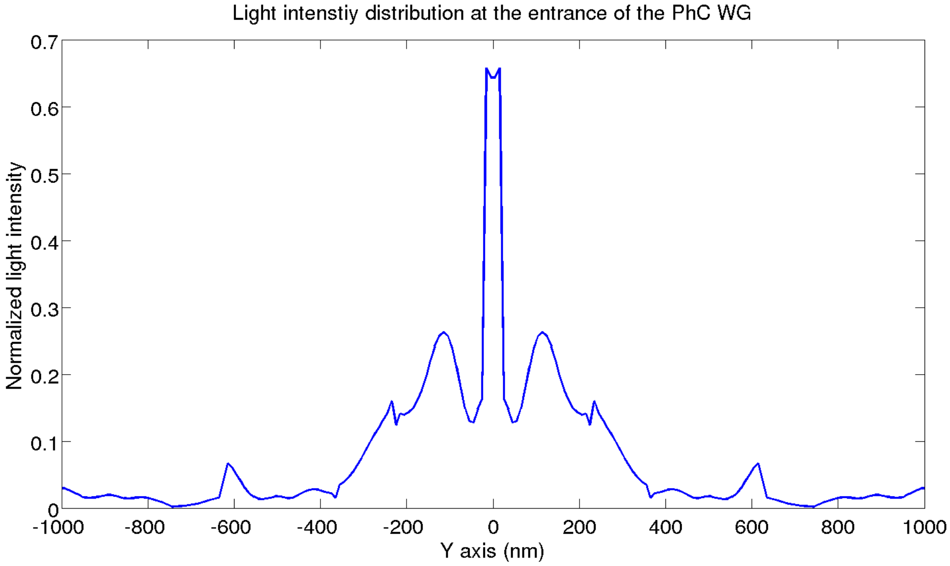

(b) $|E_y|^2_{max}$ distribution at the slotted PhC waveguide tip entrance

(continued on next page)

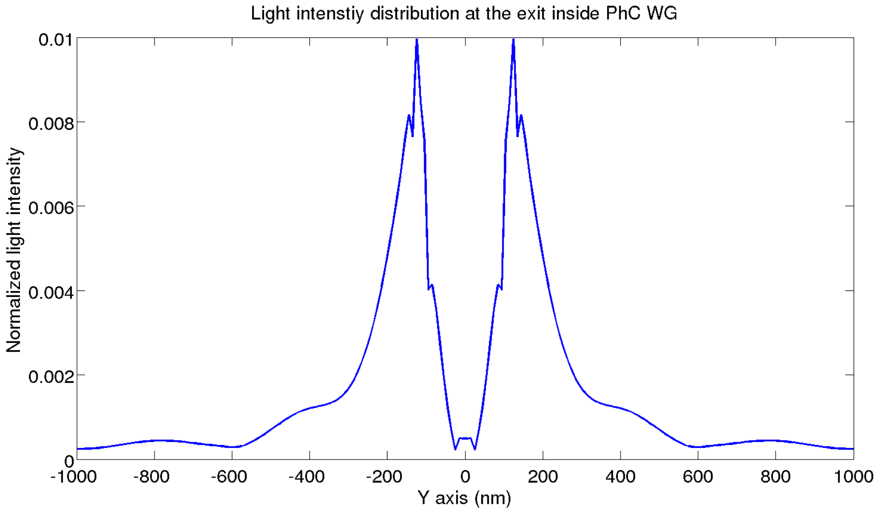

(c) $|E_y|^2_{max}$ distribution 10nm away from tip (inside)

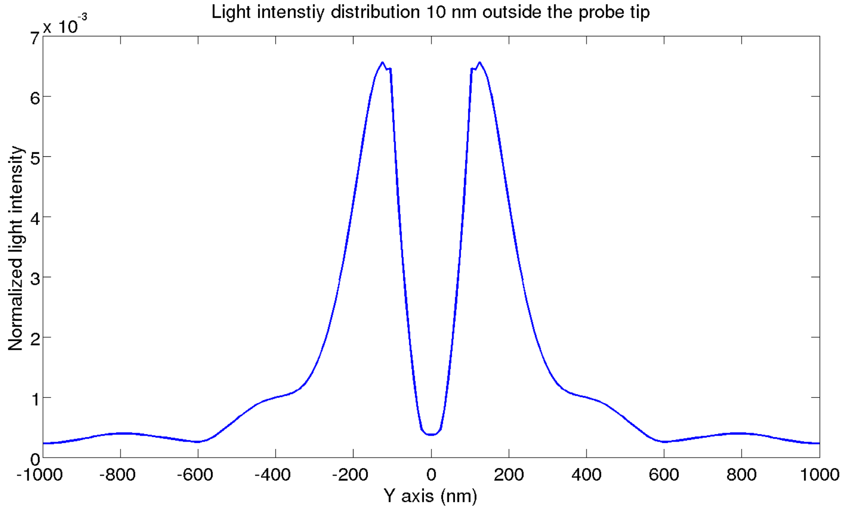

(d) $|E_y|^2_{max}$ distribution 10nm away from tip (near-field)

Figure 5.3: Probe tip FDTD analysis of the slotted PhC waveguide without embedded nanoresonator. (a) 2D FDTD modelling result for the E_y distribution along the center cross section on xy plane for simple straight slotted PhC waveguide 120° tip cut along the ΓK direction with air interface PML boundary layers surround around the calculation cell to avoid reflection from the boundaries. The slot size is $0.2a$, which is 45nm. The continuous unit source is located at where it is indicated in the plot. (b) $|E_y|^2_{max}$ distribution at the entrance of the slotted PhC waveguide tip body along y direction. (c) and (d) $|E_y|^2_{max}$ distribution at 10nm inside the tip and outside the tip respectively along y direction.

Due to the air boundary at the tip exit, there is strong reflection that causes strong side peaks without any light confinement in the slot center at both 10nm inside and outside the tip exit. The light throughput is really low in the 10^{-3} order. This kind of probe is not suitable for near-field light confinement applications. In order to remove the side lobes and still keep the center peak, it is necessary to add some light processing devices like nano resonators as it will be shown in the next section.

5.1.3 Nano-resonator based photonic crystal probe tip

Optical resonator enhances light concentration inside the cavity by constructive interference due to multiple reflection from the mirrors in order to form an enhanced standing wave. The ideology has been extensively applied in the laser source cavity designs [96]. The beam shape inside the cavity needs to be well controlled without too much spreading. This type of resonators can serve two purposes: (1) enhancing the light concentration inside the cavity; (2) beam shape controlling. The typical resonators, as used in micro optical chips, are FP cavities for its simple fabrication, where the reflecting mirrors are flat, symmetrically located, with distance of integer times of the half wavelength in the propagating medium. If the appropriate nano resonators are embedded with the slotted PhC waveguide tip, the light throughput can be greatly enhanced and the light beam inside the cavity can also be well controlled. One of such nano resonators embedded slotted PhC waveguide tip is proposed as shown in Figure 5.4 with $0.2a$ (approximately 45nm for $\lambda_0 = 632.8$nm) slot size, where two double side air holes with $0.7r$ radius occupy the adjacent PhC air hole positions in the ridged region. Since the distance between the mirror air hole is about 1.5λ, where λ is the wavelength in the Si_3N_4 medium, just by removing two air holes between the reflecting air holes (the guided mode is close to the first Brillouin zone edge), a FP cavity is formed. Figure 5.4

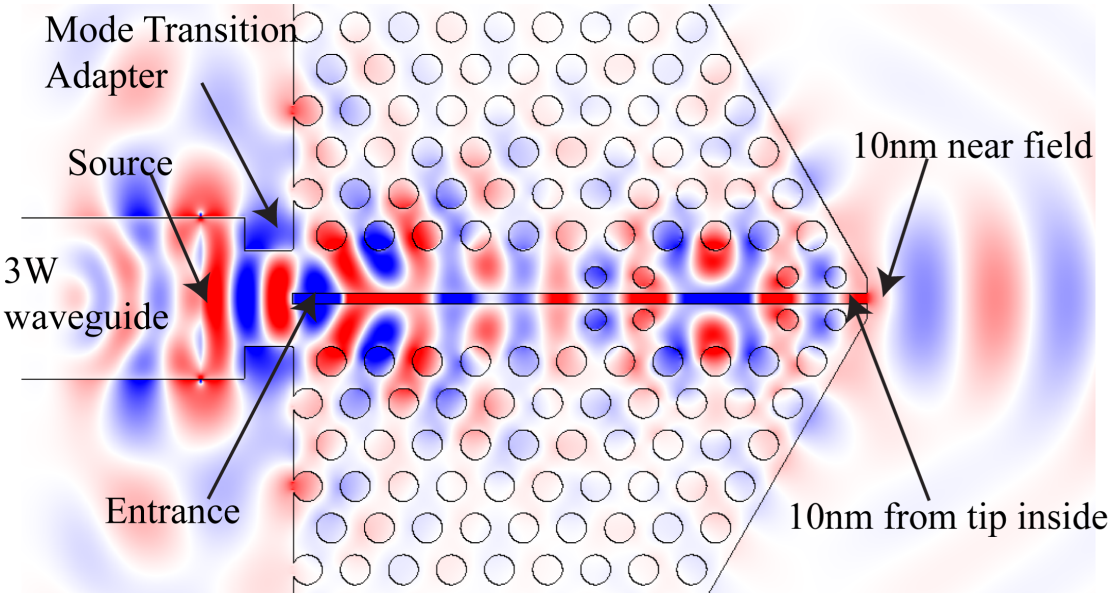

(a) E_y distribution

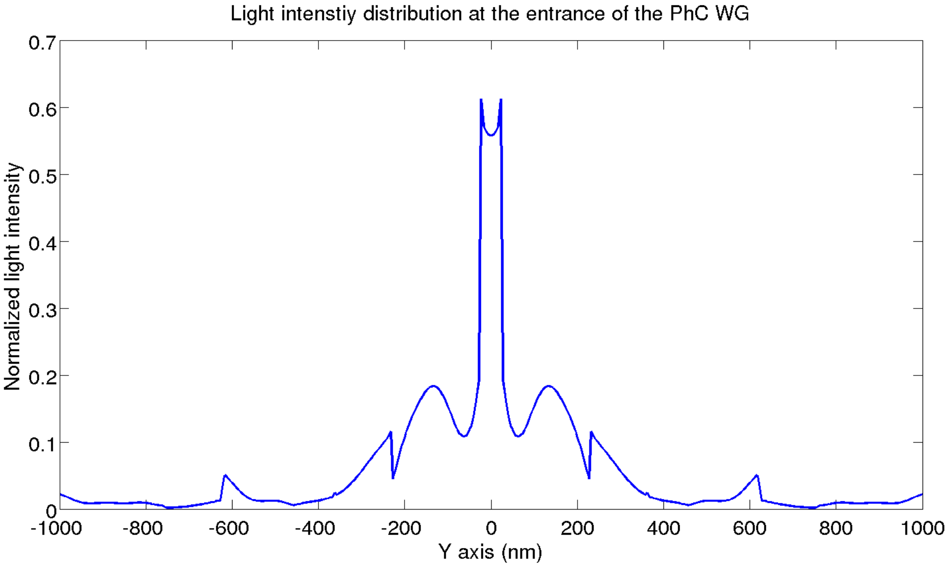

(b) $|E_y|^2_{max}$ distribution at the slotted PhC waveguide tip entrance

(continued on next page)

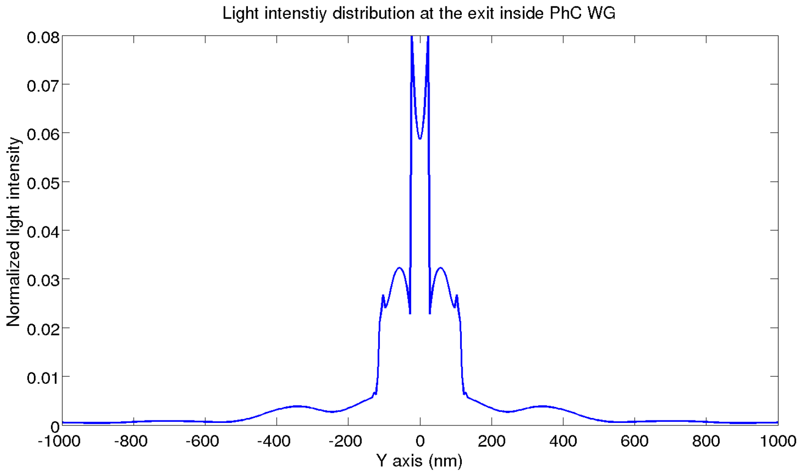

(c) $|E_y|^2_{max}$ distribution 10nm away from tip (inside)

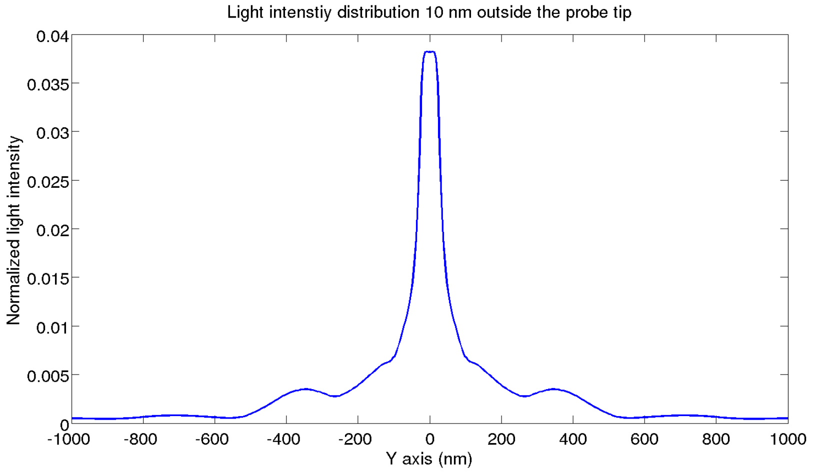

(d) $|E_y|^2_{max}$ distribution 10nm away from tip (near-field)

Figure 5.4: 2D FDTD model of the slotted PhC nanoresonator probe tip near-field analysis for slot width of 20nm. (a) 2D FDTD modelling result for the E_y distribution along the center cross section on xy plane for the slotted PhC waveguide 120° tip cut along the ΓK direction with air interface PML boundary layers surround around the calculation cell to avoid reflection from the boundaries, embedded with double side nano resonators. The two reflecting mirrors for the nano resonators are formed by the reduced radius air hole (radius is $0.7r$, where r is the bulk PhC air hole radius) in the ridged region. The cavity size for the resonator is about 1.5λ, which is equivalent to removing two bulk air holes. The continuous unit source is located at where it is indicated in the plot. (b) $|E_y|^2_{max}$ distribution at the entrance of the slotted PhC waveguide tip body along y direction. (c) and (d) $|E_y|^2_{max}$ distribution at 10nm inside the tip and outside the tip respectively along y direction.

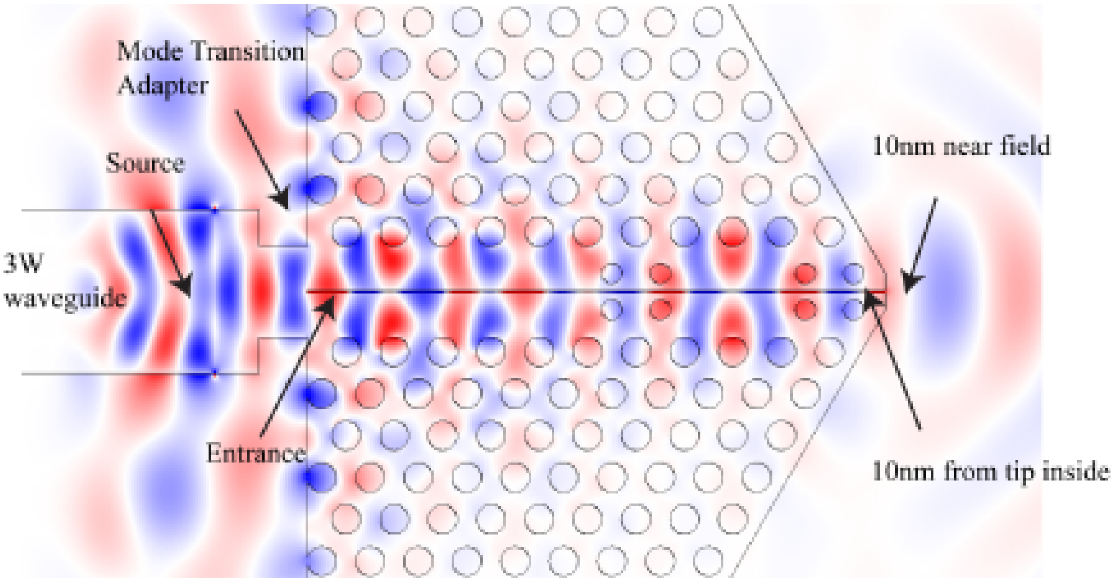

(a) E_y distribution

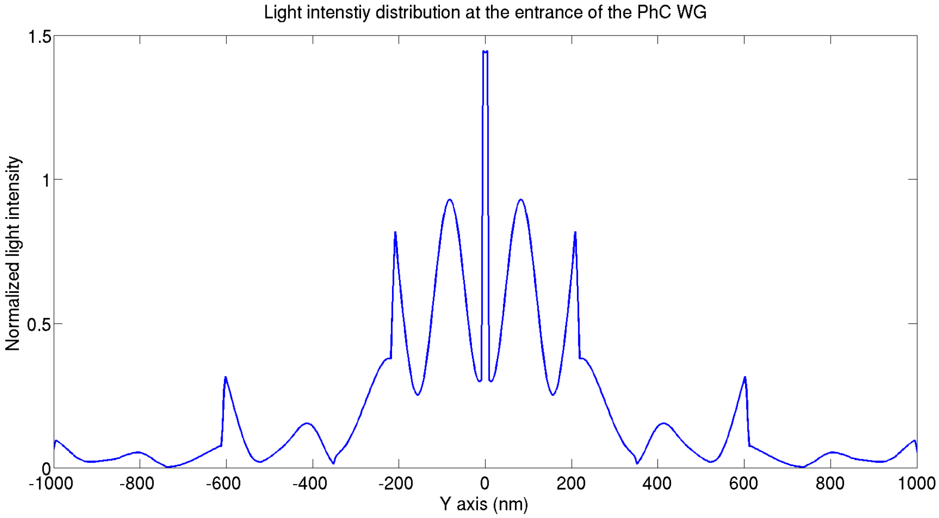

(b) $|E_y|^2_{max}$ distribution at the slotted PhC waveguide tip entrance

(continued on next page)

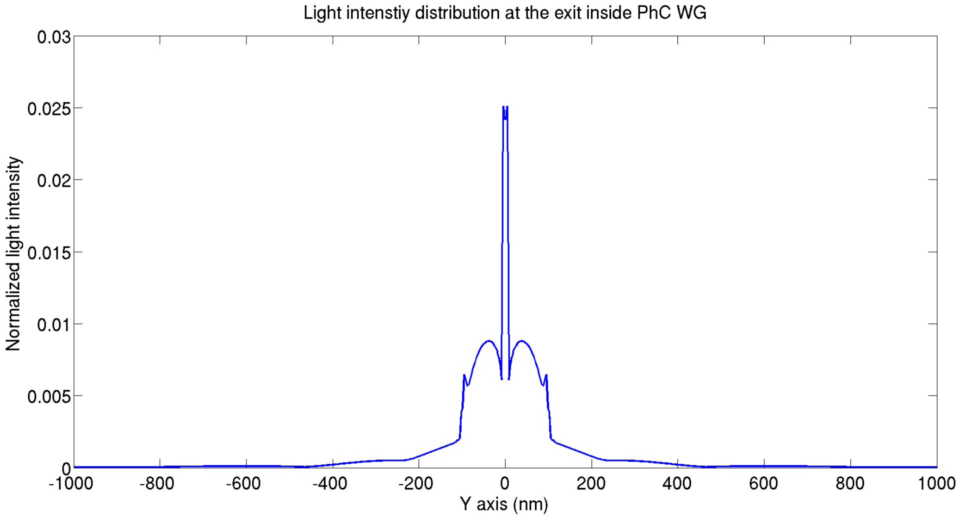

(c) $|E_y|^2_{max}$ distribution 10nm away from tip (inside)

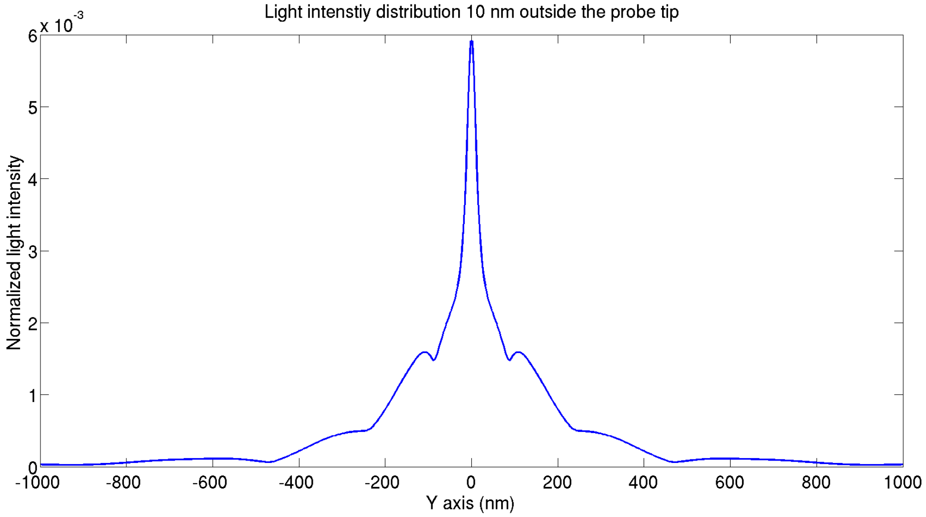

(d) $|E_y|^2_{max}$ distribution 10nm away from tip (near-field)

Figure 5.5: 2D FDTD model of the slotted PhC nanoresonator probe tip near-field analysis for slot width of 15nm. (a) 2D FDTD modelling result for the E_y distribution along the center cross section on xy plane for similar slotted PhC tip as in Figure 5.4, but with the reduced slot size of 15nm. The continuous unit source is located at where it is indicated in the plot. (b) $|E_y|^2_{max}$ distribution at the entrance of the slotted PhC waveguide tip body along y direction. (c) and (d) $|E_y|^2_{max}$ distribution at 10nm inside the tip and outside the tip respectively along y direction.

also shows the light distribution at some typical locations along the *y* direction, which demonstrates the light confinement in the slot region inside the probe body. The full width at half maximum (FWHM) of the near-field light beam at 10nm away from the tip exit is about 50nm.

The near-field FWHM of the light beam is proportional to the PhC slot size. To prove it, another slotted PhC waveguide tip with slot size of 15nm is simulated as in Figure 5.5. The bulk PhC parameters and the ridged region width are kept the same as in Figure 5.3. The near-field FWHM of the light beam for the 15nm slotted PhC waveguide tip is about 25nm. It is observed that the light throughput for the 15nm slot PhC tip is reduced about 10 times compared with that of the 45nm slot PhC tip due to the smaller aperture opening. Through the slotted PhC waveguide embedded with nano resonators light confinement tip, the near-field light confinement can reach the $\lambda/15$ level, and the light throughput is about 1000 times compared with that of the commercial tapered optical fiber with metal coating tip [73]. The proposed probe does not use any metal material as a light confinement mechanism, and still achieves high throughput with subwavelength light confinement. There are some merits regarding the proposed probe: (1) The metal free structure reduces the fabrication complexity; (2) The light confinement is controlled by the slot size; (3) Low impact on the light confinement performance by index change in the near-field medium, like water membrane as discussed in the biological application chapter.

Probe tip design proposed in this section indeed has some drawbacks such as impedance mismatch due to the local resonance at the slot entrance, light throughput proportional to slot opening size (lower throughput for smaller light confinement), and too closely packed nanoresonator air holes that cause sensitive intolerance of the fabrication inaccuracy. Although the designed nanoresonator is inside the probe body and near the probe tip exit, the local resonance only occurs in the center of the resonator that is still too far way from the near-field of the probe tip. This explains why the light throughput at the probe tip near-field is still in low level range compared to some nano optical antenna based on metal material utilizing the plasmonic effects. To overcome this issue, a resonator design by $\lambda/4$ monopole slot resonator is studied in next section so that the light throughput is no longer restricted by the aperture opening size.

5.2 Quarter wavelength slot photonic crystal probe tip

Most optical antennas are illuminated from far-field by a light source (especially plane wave source) and the focus size is diffraction limited, just like the embedded grating coupler design as mentioned in chapter 4. The large illumination area causes the background light contamination that other fancy techniques, like Raman scattering enhancement [97], two photon luminescence [98] or fluorescent emitters [99], are needed to overcome the contamination issues. Recently a $\lambda/4$ monopole optical antenna has been modeled and tested in the metal generated plasmonic resonance waveform as an effective nano light subwavelength focusing probe tip [100]. Though it avoids the background noise contamination issues by mounting the monopole optical metal antenna on the pulled optical fiber with circular aperture opening, the intrinsic low transmission rate by the pulled optical fiber severely obstructed the final subwavelength localized light intensity. The metal structure in the nanometer scale has the light absorption that causes heat damage to the probe tip. Moreover the probe metal tip is manually fabricated by focused ion beam (FIB) milling which hinders its mass fabrication potential. In this section, I study the PhC waveguide made by pure low index dielectric material to drive the nano slot resonator that has strong light localization and enhancement in the near-field of the probe tip. By considering the light feeding part (PhC waveguide) and the focus part (nano $\lambda/4$ slot resonator) as a whole system, the light transmission is greatly improved and still in subwavelength focusing size in the near-field. The first step is to find the optimized PhC waveguide with minimal back reflections through calculation of S parameters. The optimized PhC waveguide serves as the highly efficient antenna driving light source that there is no place for light in PBG to escape except towards the slotted probe tip aperture. Based on the self resonance of the slot with $\lambda/4$ length, strong resonance occurs in the slot region that enhances the light localization intensity and the light throughput at the subwavelength level.

5.2.1 S parameters analysis

In the last section, the MPB diagram of the slotted PhC is used to optimize transmission rate, so that low loss slotted PhC waveguide serves as the design platform to embed the center placed nano resonators. It is essentially a frequency domain method. Compared to the PhC waveguide discussed in the last section, the PhC waveguide for the $\lambda/4$ slot resonator is strictly a single line defect (1W) PhC waveguide, since there is no need to make extra space to accommodate the FP resonators by shrunk air holes in the center PhC defect. Thus the transmission rate for such a 1W PhC waveguide is anticipated to have greater value.

In order to directly derive the light transmission through PhC waveguide without center slot, I calculate the S_{11} parameter for PhC lattice constant in certain range to lower the S_{11} with minimal value in the time domain. A 250nm Si_3N_4 slab thickness is assumed for the FDTD model as illustrated in Figure 5.6. Two normal dielectric rib waveguides are interfaced on both sides with the PhC waveguide slab. The width of

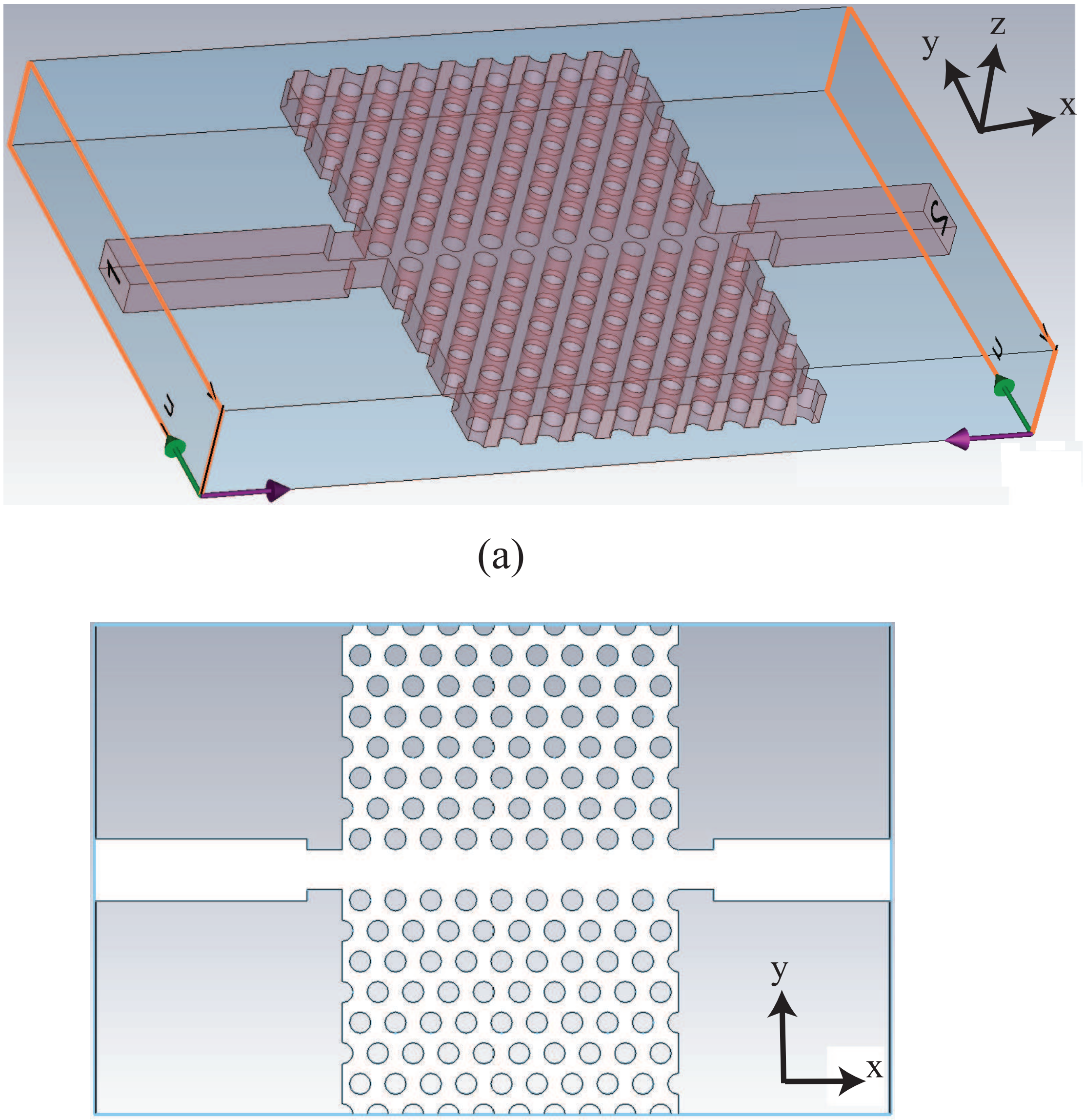

(a)

(b)

Figure 5.6: 1W PhC waveguide model with half wavelength mode transition adapter. (a) 3D model of the PhC waveguide with waveguide ports as illustrated; (b) *xy* center cross section plane.

the dielectric rib waveguide is 500nm and it conforms with rib waveguide design in the embedded metallic grating coupler design. Since it is straight single mode waveguide,

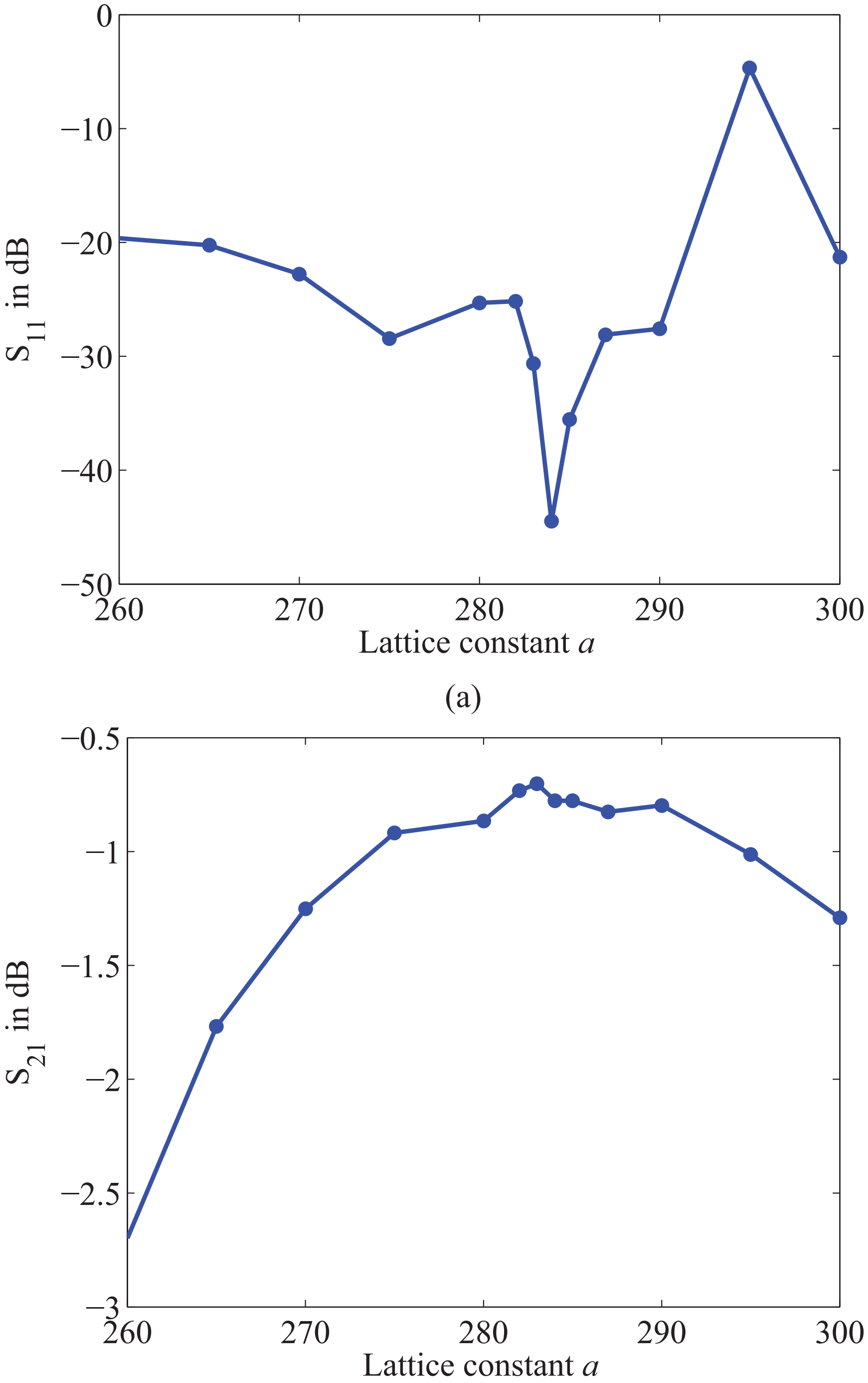

(a)

(b)

Figure 5.7: 1W PhC waveguide S parameter plot as function of lattice constant *a* based on FDTD calculation. (a) S_{11}; (b) S_{21}.

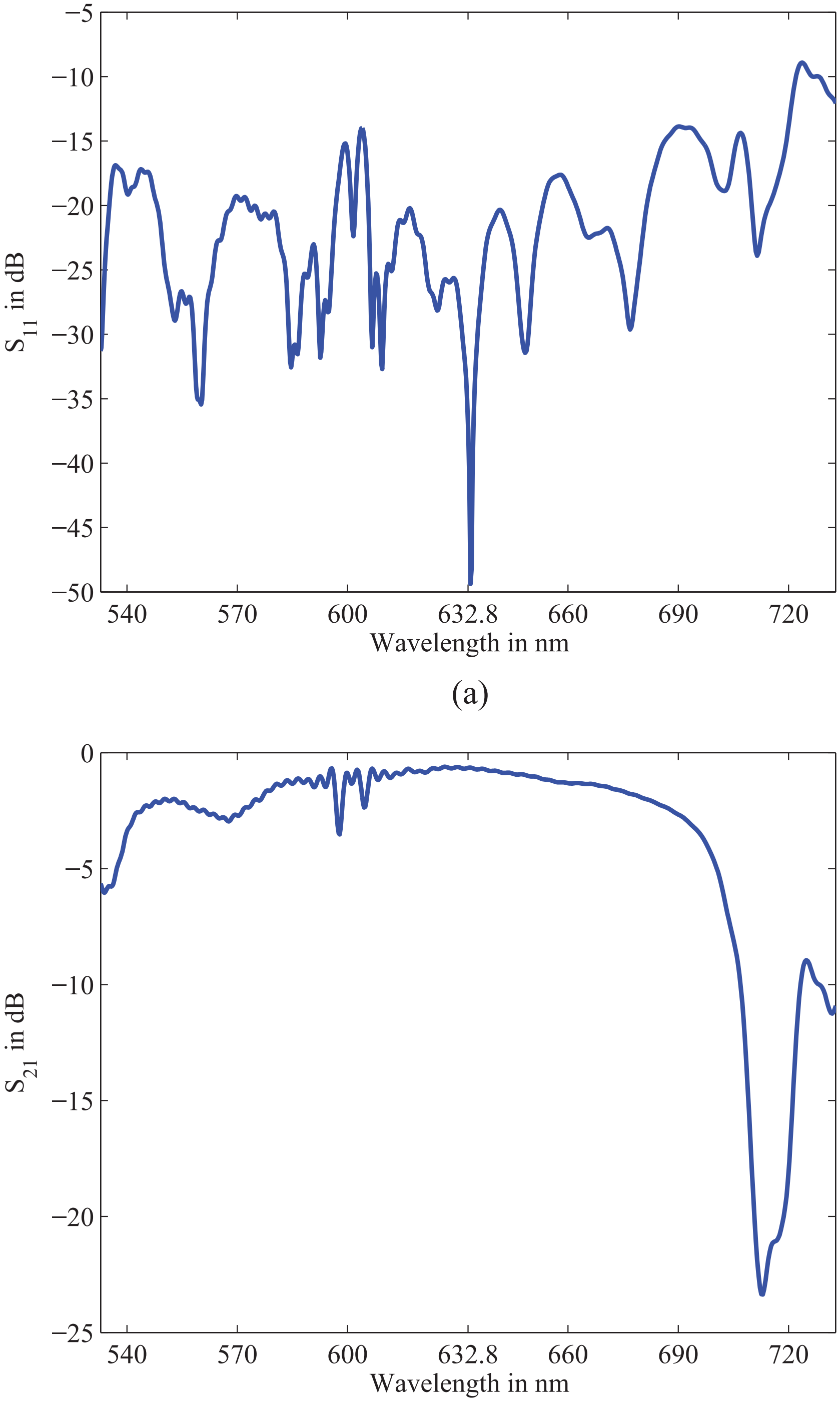

(a)

(b)

Figure 5.8: 1W PhC waveguide S parameter plot as function of wavelength for lattice constant of $a = 284$nm. (a) S_{11}; (b) S_{21}.

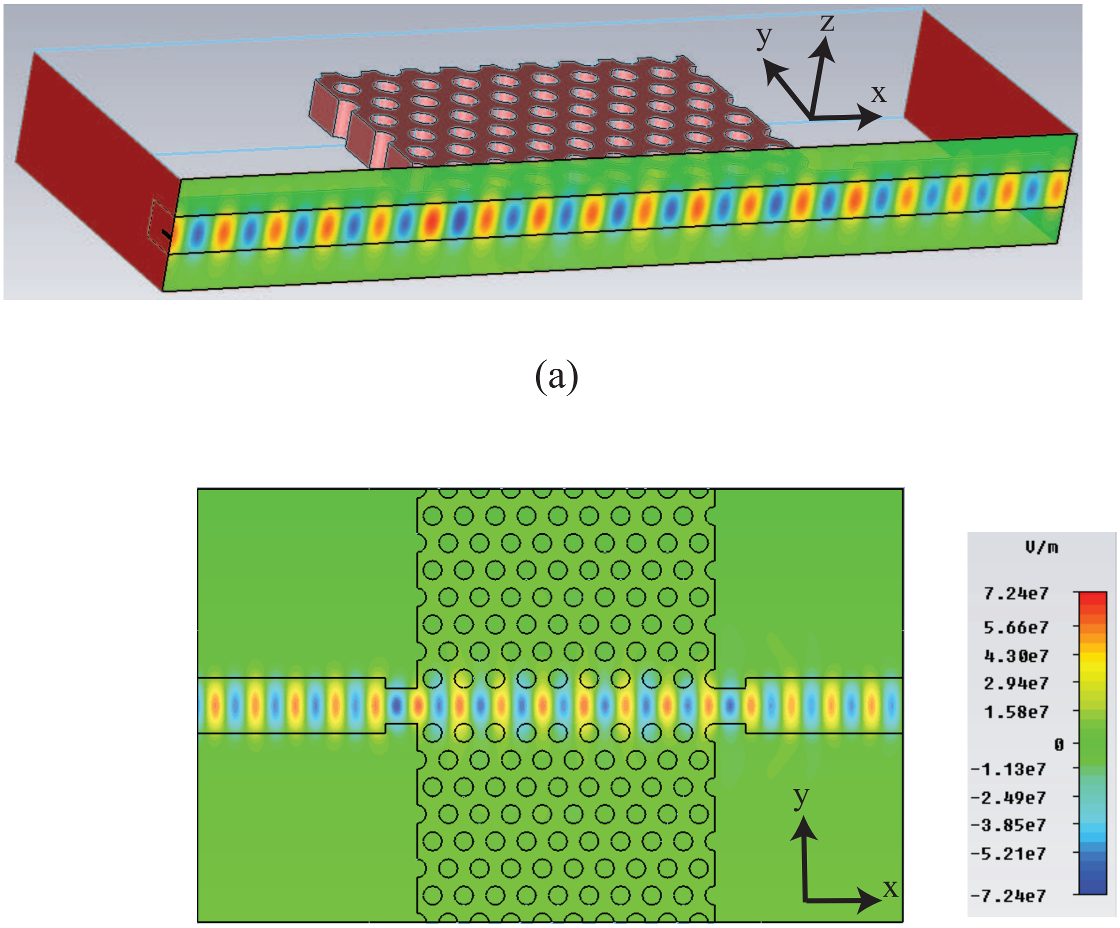

(a)

(b)

Figure 5.9: $|E_y|$ distribution plots at cross section planes for 1W PhC waveguide with lattice constant of $a = 284$nm at wavelength 632.8nm. (a) $|E_y|$ on xz center cross plane; (b) $|E_y|$ on xy center cross plane.

the loss of the rib waveguide can be ignored. In order to avoid long adapting length of the mode size difference between rib waveguide and that of the 1W PhC waveguide, half wavelength mode adapters are also used on both sides of the PhC waveguide. By assuming a single waveguide mode, the transmission and reflection of the structure can be calculated by FDTD method. A waveguide port excitation in TE polarization (with

E_y component only) is set in the rib waveguide on port 1 with total power of 1 watts (Figure 5.6(a)). In the following simulations, the field calculations and their units are all based on this total power input assumption.

The optimal lattice size of the 1W PhC waveguide can be determined from the reflection and transmission plot of the structure as shown in Figure 5.7. At lattice constant $a = 284$nm, the reflection S_{11} reaches minimum and the transmission S_{21} reaches maximum indicating the lattice constant value for the lowest loss for 1W PhC waveguide. The peak transmission rate as indicated by S_{21} parameter is 92.8% where the negligible loss is due to the slight resonance of the transition adapter and the out of plane radiation. To further prove this, a 3D FDTD model for lattice constant $a = 284$nm calculates the E_y distribution in the structure at excitation wavelength at 632.8nm as shown in Figure 5.8 and 5.9. The light propagates along the $\boldsymbol{x}$ direction with no light penetrating the PhC regular lattice area and in the slab vertical direction light is limited by the TIR which indicates the PhC waveguide guided mode at 632.8nm works under the light line (Figure 5.9). The half wavelength mode transition adapter also changes the mode size from 500nm to the 1W size with minimal resonance without using longer length adiabatic transition adapter. The single mode light inside the rib waveguides is kept in both the input and out direction. Though the PBG is not calculated, the time domain method that plots the S_{11} and S_{21} parameters in Figure 5.8 indicates the 632.8nm wavelength locates in the band gap center. It is observed the 3dB transmission bandwidth in terms of wavelength ranges from 570nm to 690nm for PhC 1W waveguide with lattice constant $a = 284$nm by the S_{21} plot in Figure 5.8(b). It suggests the proposed PhC 1W waveguide also supports light propagation in this 3dB wavelength range which also fits the possible fluorescence signal wavelength for excitation wavelength at 632.8nm. For example, the Cy5 fluorophore emission wavelength for 632.8nm excitation is around 690nm. In the biological application chapter of this thesis, the detection scheme by collecting nanometer scaled fluorescence emission is also simulated to assess the performance of the probe.

5.2.2 Transmission line model

$\lambda/4$ based devices can be commonly found in the microwave range for electromagnetic wave impedance matching with maximum power delivery into the load device like RF antennas. A typical transmission line based impedance matching device is a quarter-wave impedance transformer. Another $\lambda/4$ idea based microwave device is $\lambda/4$ monopole antenna or slot antenna. The monopole and slot antennas are essentially complementary structure that can be analyzed by similar current resonance distribution method. The same $\lambda/4$ idea can also be used to design the resonators. In this part of the thesis, I propose a $\lambda/4$ slot resonator embedded in PhC waveguide for maximal light energy delivery in the near-field free space. And due to the boundary condition in the slot, the resonance in a standing wave form is located inside the slot region with light intensity peak near the very end of the probe aperture tip under ideal impedance matching condition.

Before analyzing the $\lambda/4$ slot optical resonator in depth, a transmission line based model calculates the voltage (electric field) and current distribution in a typical $\lambda/4$ impedance transformer. As illustrated in Figure 5.10 in the segment of the transmission line input, there is no electromagnetic wave reflection back at the input point due to the impedance match, since the input impedance looking into the $\lambda/4$ transformer is exactly the same as the transmission line characteristic impedance. To achieve such impedance matching condition, there are two conditions that need to be met: (1) The length of the matching segment is $\lambda/4$ long to cause the light reflected back from load to

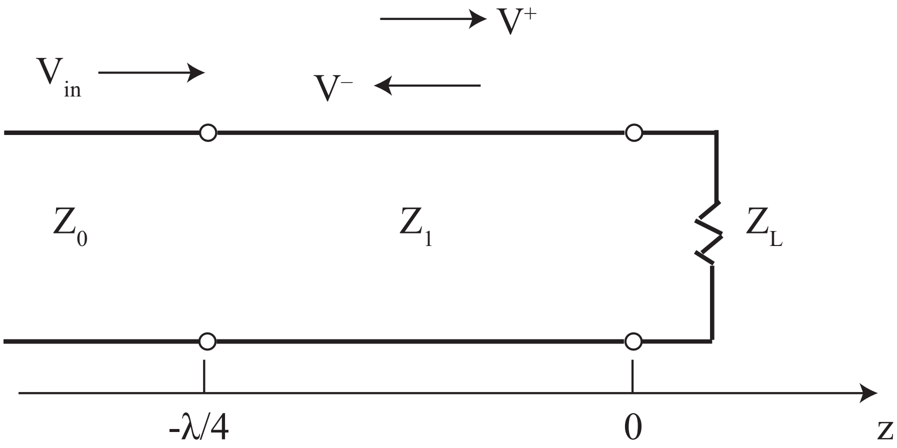

Figure 5.10: Transmission line model for the $\lambda/4$ impedance transformer. The voltages at each segments are as indicated.

have 180° phase change for each round trip; (2) The impedance of the $\lambda/4$ transformer is the geometric mean of the load impedance and the transmission line input impedance $Z_1 = \sqrt{Z_0 Z_L}$. It is useful to derive the voltage or electric field distribution along the standing wave region, since it is ultra important for near-field analysis.

The input signal from the transmission line with impedance Z_0 is expressed in time harmonic form

$$V_{in} = V_i e^{j\omega t - j\beta z} \tag{5.1}$$

where ω is the radian frequency and $\beta = \dfrac{2\pi}{\lambda}$ is the wave number. The voltage along the transmission line in the $\lambda/4$ impedance transformer region are composed of both the positive z propagation component V^+ and the reflected back wave V^- from the load mismatch

$$V(z) = V^+ e^{j\omega t - j\beta z} + V^- e^{j\omega t + j\beta z}. \tag{5.2}$$

Similarly the current distribution in the transformer region can be decomposed into the the two components as well (the negative sign for the reflected component is due to the wave propagation direction)

$$I(z) = \frac{V^+}{Z_1} e^{j\omega t - j\beta z} - \frac{V^-}{Z_1} e^{j\omega t + j\beta z}. \tag{5.3}$$

By setting the boundary condition at the input junction for $V(-\frac{\lambda}{4}) = V_{in}$, one can have $V_i = V^+ - V^-$. The boundary condition at the load junction gives that $Z_L = \frac{V(0)}{I(0)} = Z_1 \cdot \frac{V^+ + V^-}{V^+ - V^-}$. Thus the equation (5.2) for the voltage distribution in the transformer region under impedance matched condition can be rewritten in terms of the input voltage and the impedances

$$V(z) = V_i \left[\left(\frac{\frac{Z_L}{Z_1} + 1}{2} \right) e^{-j\beta z} + \left(\frac{\frac{Z_L}{Z_1} - 1}{2} \right) e^{j\beta z} \right] e^{j\omega t}. \tag{5.4}$$

The equation (5.4) describes a standing wave distribution along the $\lambda/4$ transformer. As an example the impedances for input transmission line and the load are assumed to be $Z_0 = 50\Omega$ and $Z_L = 377\Omega$ with voltage and current distribution amplitude envelopes plotted in Figure 5.11. For slot waveguide resonator, the near-field free space can be simplified as free space wave impedance with $Z_L = 377\Omega$, just as most aperture based antenna structure. The peak voltage amplitude occurs at the load terminal based on the plots of Figure 5.11 which also indicates the peak electric field locates at the near-field aperture for aperture type antennas. The same phenomena also happens for arbitrary combination of Z_0 and Z_L based on the observation of equation (5.4). For instance as demonstrated in microwave range the strong electric field near the slot aperture towards free space can excite Argon plasma in atmospheric pressure by $\lambda/4$ slot waveguide [101]. The plasma intensity distribution along the slot region conforms with the electric field distribution. At the end of the slot aperture the electric field reaches the highest value.

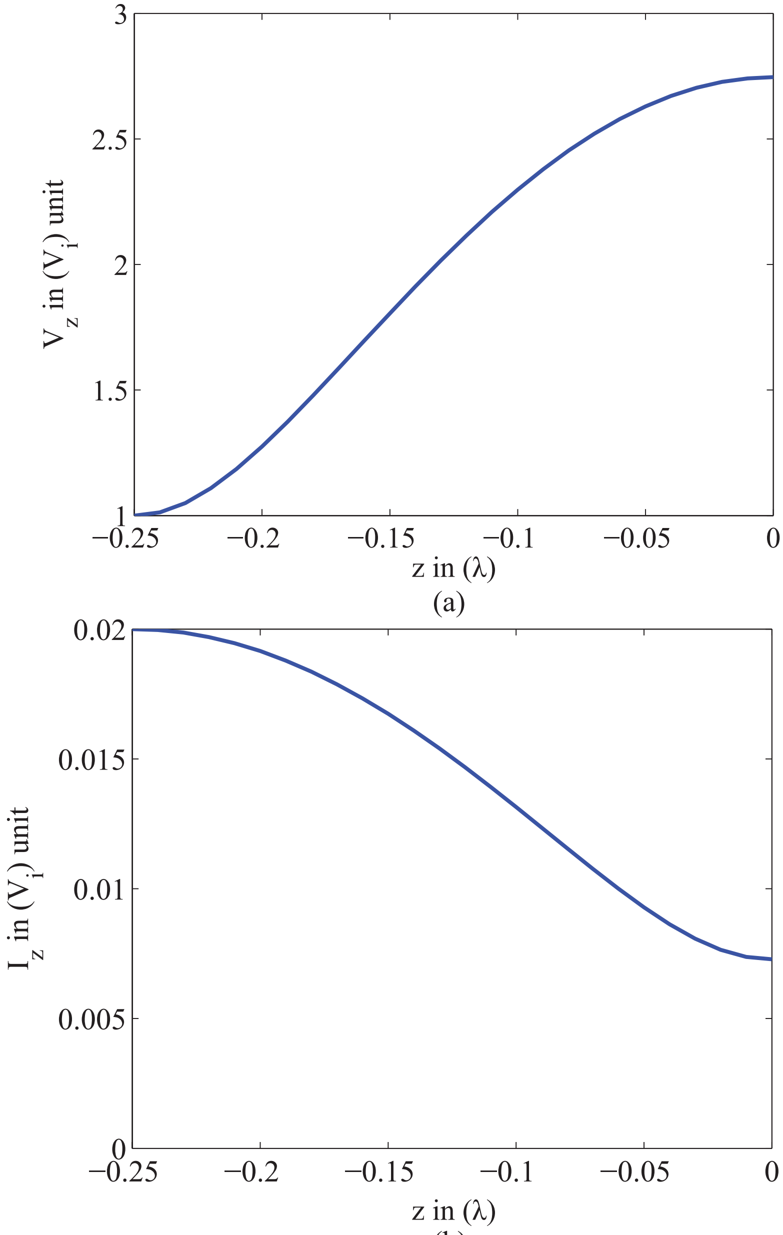

(a)

(b)

Figure 5.11: Voltage and current amplitude for standing wave in the $\lambda/4$ impedance transformer with assumption of matched condition with $Z_0 = 50\Omega$ and $Z_L = 377\Omega$.

5.2.3 Probe tip analysis

The $\lambda/4$ resonance idea can be adapted to design the near-field optical confinement probe. The $\lambda/4$ monople antenna made by metal at visible range has been realized by FIB etching the metal coated pulled optical fiber in optical wavelength range just as the monopole RF antenna [100]. The pulled optical fiber aperture tip serves as confined light excitation source but in an inefficient manner. There exists strong impedance mismatch between the optical fiber traveling mode and the monopole resonance mode due to the coned optical fiber aperture structure, which causes much less light transmission efficiency, since they behave much like two separate systems.

Compared to the microwave counterpart made by metal slot, the proposed optical slot is made from the pure dielectric material without absorption loss as illustrated in Figure 5.12. The embedding of the nano slot inside the PhC waveguide combines the excitation source and the $\lambda/4$ slot resonance part as a whole system. The 1W PhC waveguide provides a light insulation platform for exciting the dielectric slot without mode mismatch restriction. It also serves as the equivalent ground plane at the input end of the slot. The boundary condition of continuous electric displacement field causes the high electric field inside the air slot for TE polarization waves. The electric field in the metal rod in the RF monopole antenna is distributed on the metal surface. Instead for optical slot in the proposed structure the electric field locates right inside the so called “air rod” and wave bounces back and force in the similar manner as RF metal rod. The only difference is no Ohmic loss and electric field focuses inside the center of the “air rod” which helps light focused with one single lobe in the center of the probe tip at the near-field. So the proposed $\lambda/4$ nano slot embedded with PhC waveguide behaves similarly as the grounded $\lambda/4$ monopole antenna in RF range.

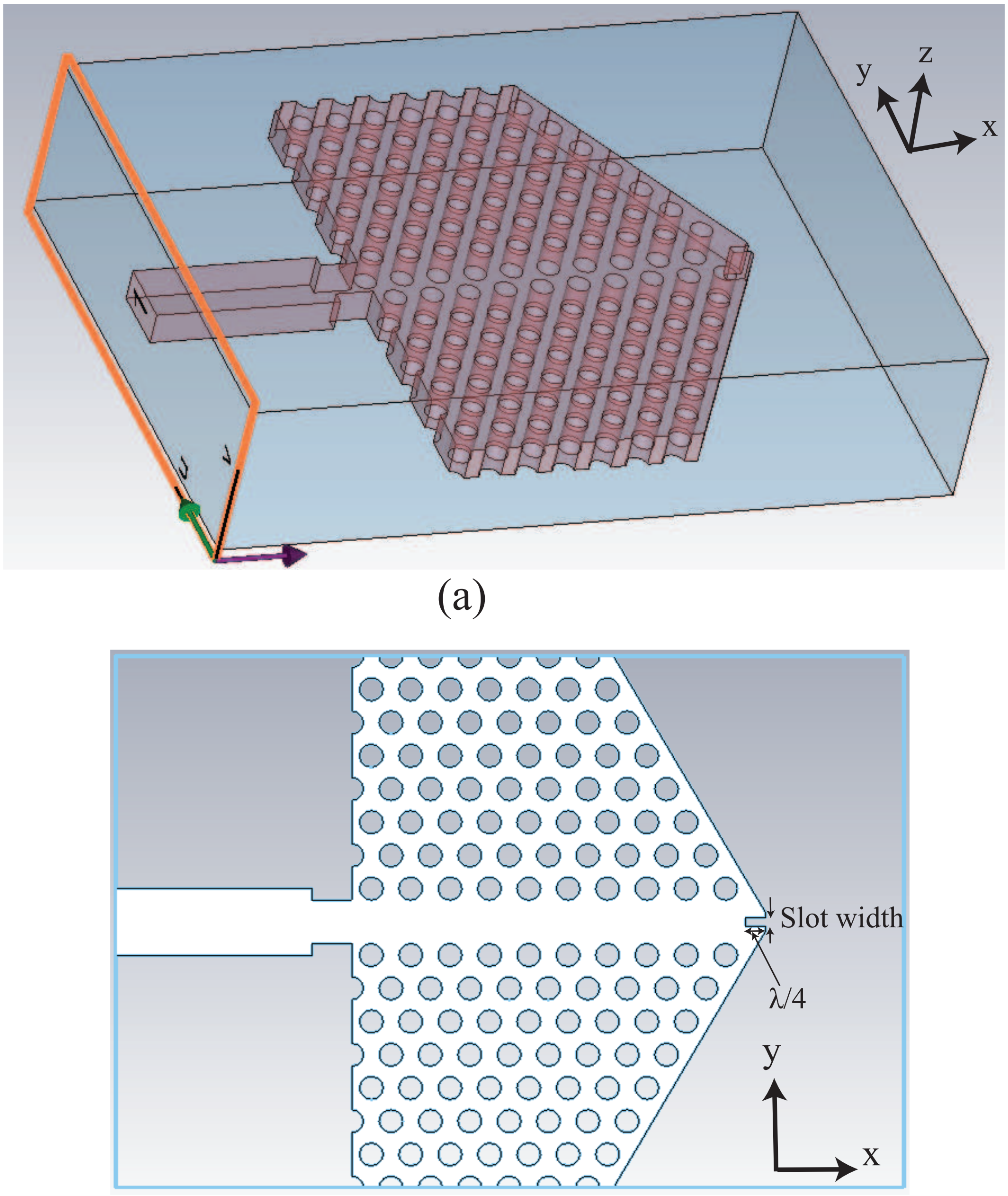

(a)

(b)

Figure 5.12: $\lambda/4$ nano slot embedded in 1W PhC waveguide. (a) 3D model of the $\lambda/4$ nano slot embedded in 1W PhC waveguide with waveguide port as illustrated; (b) *xy* center cross section plane with slot aperture opening and slot length as indicated.

The transmission line model simplified the problem into the ideal impedance matched scenario. As discussed in the transmission line model, the first condition for impedance match at optical wavelength is easy to fulfill by just fixing the slot length to be $\lambda/4$. However the second condition for controlling the characteristic impedance in the slot region is hard to achieve without changing the slot design such as by adding other delicate tuning structures into the slot region. And in such nano scale it is not realistic to put too much extra structure during the fabrication process. In this design I make a compromise between the ideal impedance match and the system complexity to still achieve strong light resonance in the probe tip. Even in non-ideal case, the light also distributes heavily in the right part of the slot towards the free space load, which is also proved by the numerical modeling.

In the 3D FDTD model the structure is excited from single mode waveguide port E_y source with wavelength center at 632.8nm. The rib waveguide, the half wavelength adapter structure and the 1W PhC waveguide all have same values as the optimized ones in the 1W PhC structure as indicated by Figure 5.9. The nano slot length is half PhC lattice size (equivalent to the $\lambda/4$) with arbitrary subwavelength slot width which is only limited by the fabrication limit. So the typical EBL feature size definition capability limit of 20nm is chosen as the slot width in the model. The amplitude of the E_y component is calculated by 3D FDTD method and the results are plotted in Figure 5.13. Though the characteristic impedance in the slot region is not optimized for ideal impedance match, it still presents the highest resonance peak at the right part of the slot towards the probe tip aperture as predicted by transmission line model and the close up plot of the E_y field amplitude at the probe tip aperture as shown in Figure 5.14. The resonance peak can be located by close up center cross line plot of the E_y field on Figure 5.15 locating at $x = -35$nm which echoes the discussion of the transmission

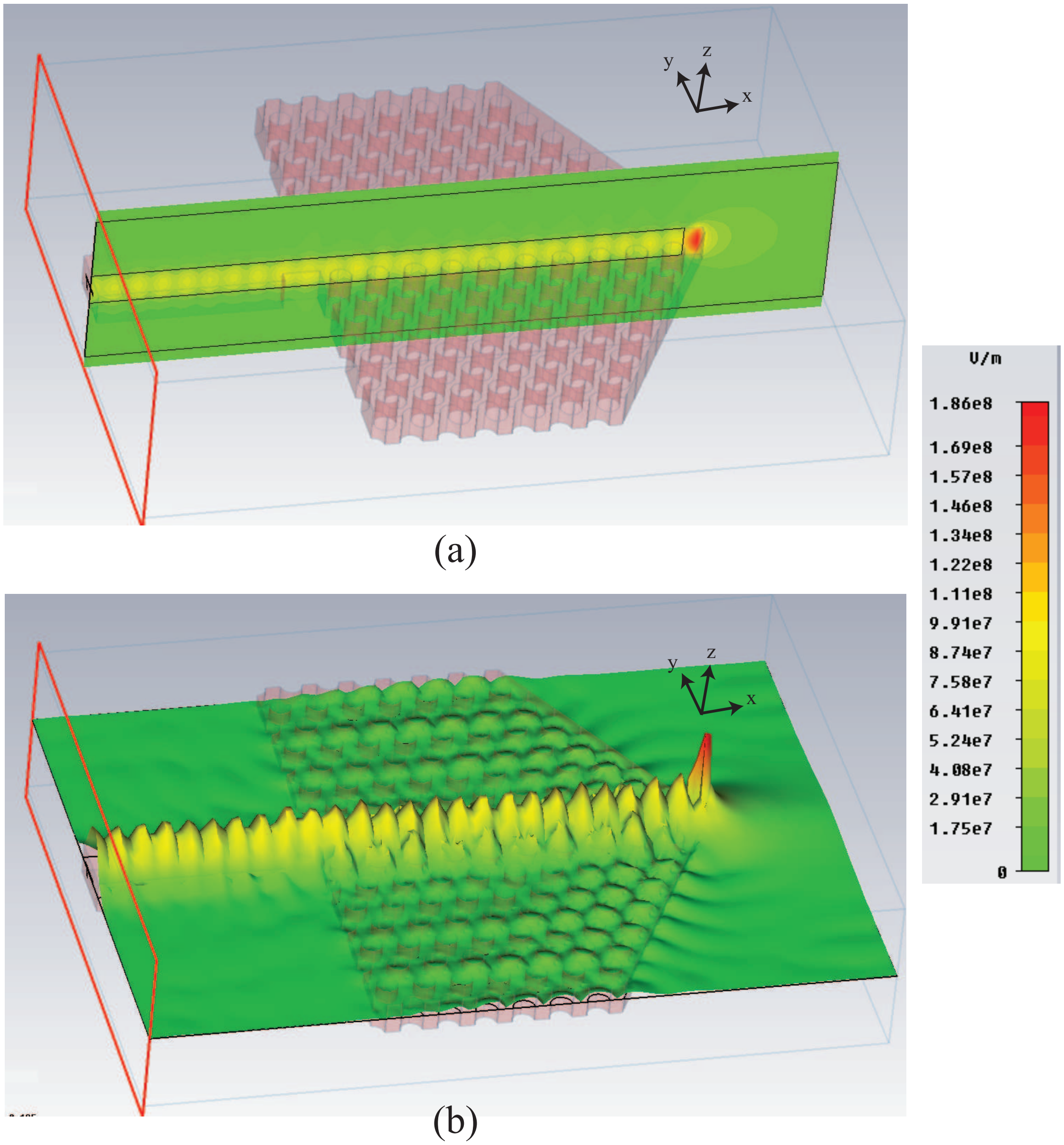

Figure 5.13: $|E_y|_{max}$ field plots of the $\lambda/4$ slot resonator embedded in 1W PhC waveguide by 3D FDTD method. (a) $|E_y|_{max}$ amplitude contour plot on xz center plane; (b) $|E_y|_{max}$ amplitude contour plot on xy center plane.

line model. Compared to the waveguide excitation source center intensity, there is ×3.6 enhancement on $|E_y|_{max}$ amplitude. In the vertical direction, the TIR keeps the light

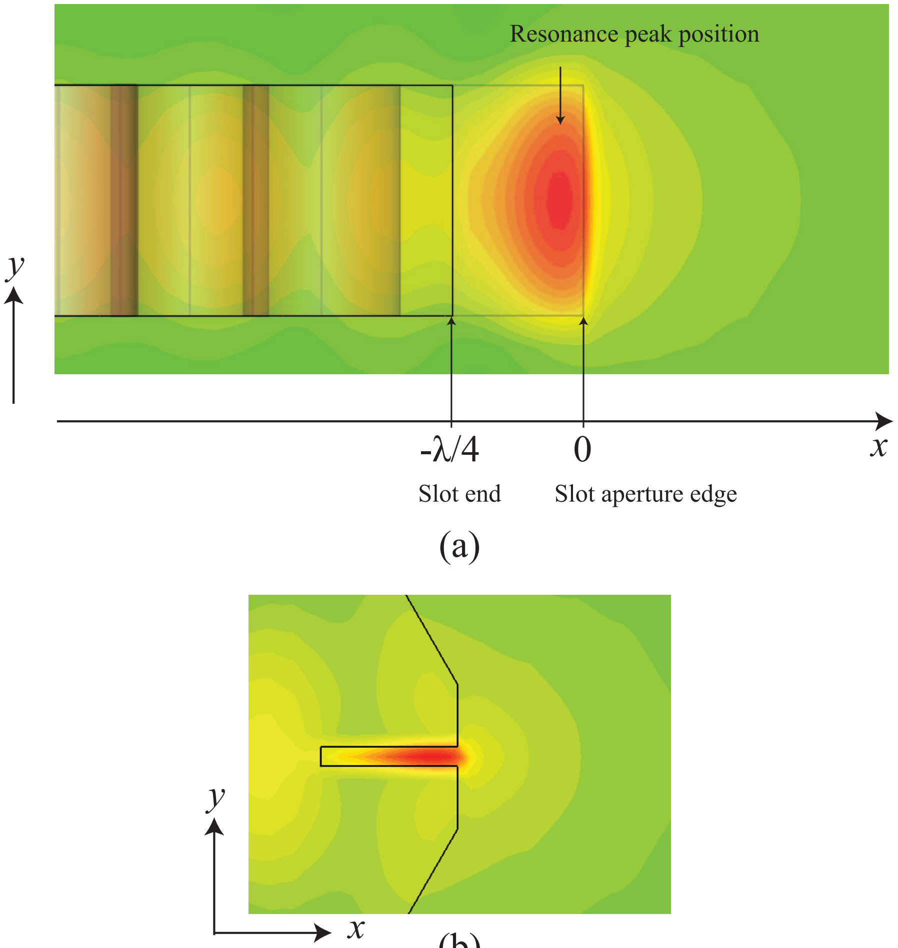

(a)

(b)

Figure 5.14: $|E_y|_{max}$ field amplitude plots at the probe tip aperture of the $\lambda/4$ slot resonator embedded in 1W PhC waveguide by 3D FDTD method. (a) $|E_y|_{max}$ amplitude contour plot on xz center plane near probe aperture; (b) $|E_y|_{max}$ amplitude contour plot on xy center plane near probe aperture. The plots has the same intensity color bar as that of Figure 5.13.

confined in the vertical direction. The resonance peak light is confined in the air slot region on the center xy lateral plane due to the continuous electric displacecment field across the slot/air boundary. Not like the center placed nano slot PhC resonator probe tip design, there is no other strong resonance points inside the structure except the one near the probe tip aperture which greatly help reduce the back reflection and enhance

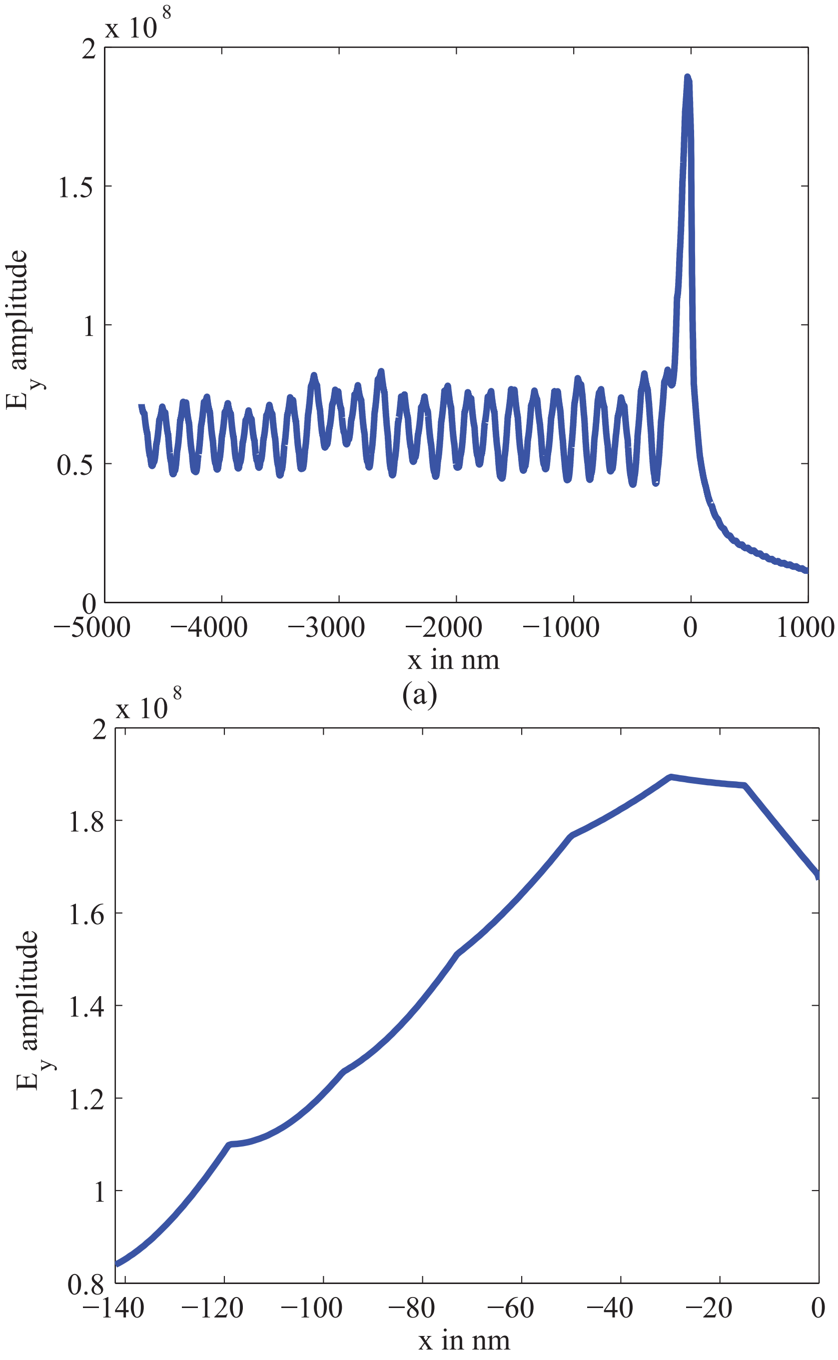

(a)

(b)

Figure 5.15: $|E_y|_{max}$ field amplitude along the $\lambda/4$ slot resonator embedded in 1W PhC waveguide center line in x direction. (a) $|E_y|_{max}$ field amplitude in unit of V/m along x direction for the whole calculation domain; (b) $|E_y|_{max}$ field in unit of V/m amplitude in the $\lambda/4$ slot region along x direction.

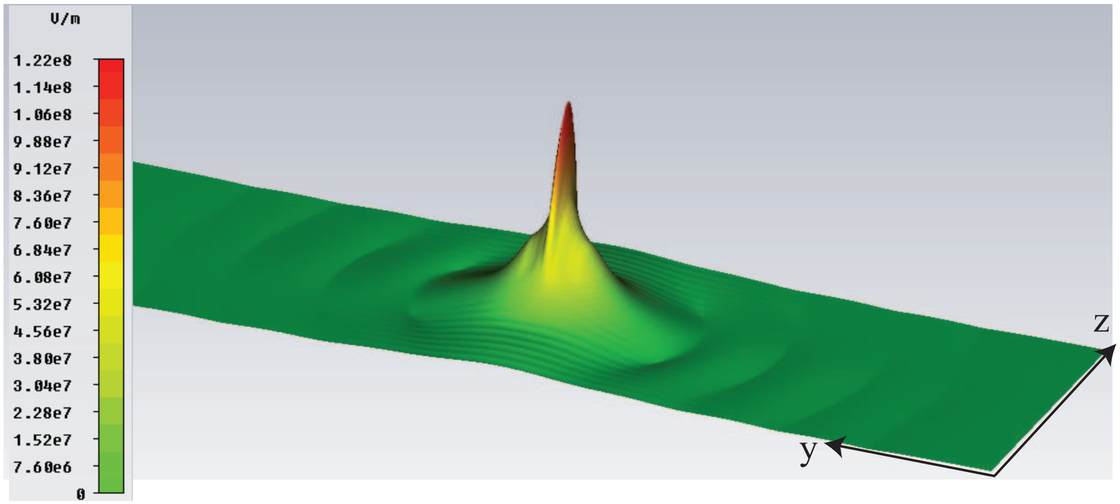

Figure 5.16: $|E_y|_{max}$ field amplitude on yz cross plane at near-field with $x = 10$nm for the $\lambda/4$ slot PhC probe tip.

the transmission of the probe.

It is expected that the near-field light is also confined due to the aperture beam pattern inside the probe body. Figure 5.16 plots the $|E_y|_{max}$ amplitude field in 3D surface form at $x = 10$nm yz cross plane based on 3D FDTD results. There is only one main center lobe at the probe aperture center and the beam size in y direction is proportional to that of the slot width. Figure 5.17 shows the $|E_y|^2_{max}$ light intensity amplitude at $x = 10$nm along y direction. It is found the FWHM of the light beam at $x = 10$nm is 32.3nm which is only 12.3nm larger than that of the slot width. The beam size is well below the subwavelength level for $\lambda = 632.8$nm, which is about $\lambda/20$. In the vertical direction the beam size is about $\lambda/3$. However compared to the center distributed nano resonator and that of the pulled metal coated optical fiber probe tip, the light intensity is enormously enhanced to be $\times 4.2$ higher than that of the waveguide excitation center intensity as demonstrated in the normalized intensity plot in Figure 5.17.

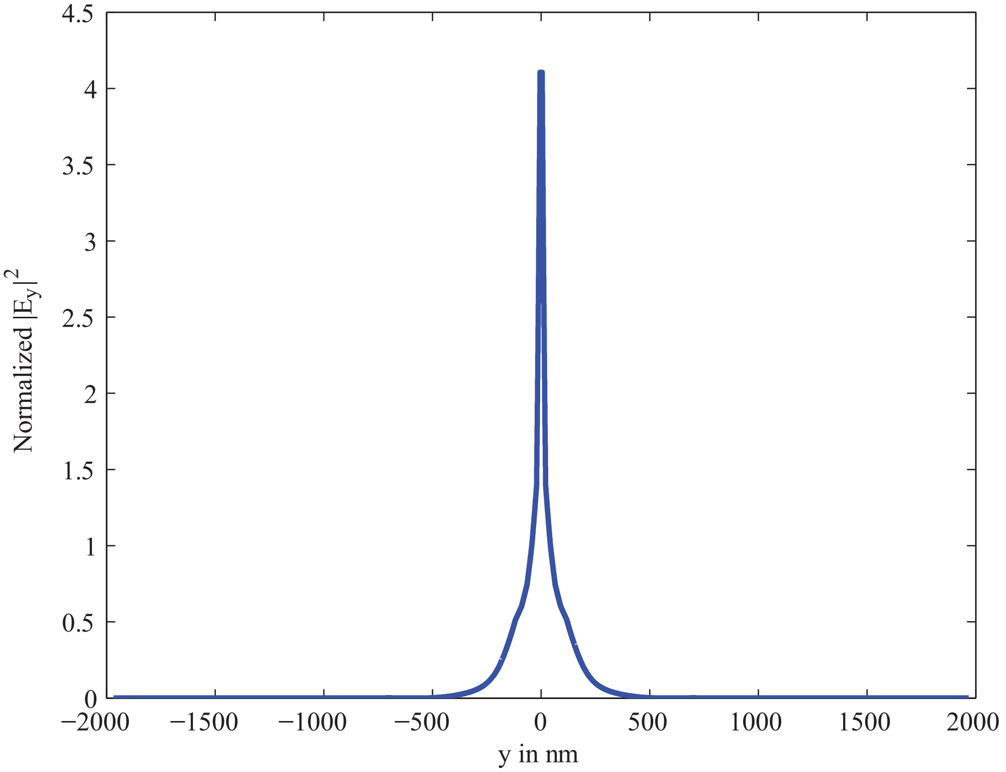

Figure 5.17: $|E_y|^2_{max}$ field normalized amplitude on yz cross plane at near-field with $x = 10$nm for the $\lambda/4$ slot PhC probe tip.

5.3 Summary

In this chapter two sets of PhC waveguide based nano resonator designs have been proposed and verified by numerical modeling. The first set of design uses center placed nano resonator embedded in slotted PhC waveguide center defect. The resonance inside the probe body enhances the light intensity in the near-field to be in 4% level. The second set of design places the $\lambda/4$ “air rod” at the very end of the probe tip, so that light is unrestricted due to the electric field resonance. Combined with the previous proposed embedded metallic grating coupler design which enhances the light coupling from free space light source intensity to ×282.24 level, the total light intensity enhancement factor towards the probe tip near-field at $x = 10$nm is $\times 1185.41$ if the light loss in the rib dielectric waveguide is in the minimal level. Both designs achieves $\lambda/20$ level by just adjusting the slot width to subwavelength level. The throughput in the $\lambda/4$ slot resonator design is not restricted by the slot width due to voltage resonance occurs right at the impedance load as predicted by the transmission line model. These kinds of designs solve the light absorption issues met by other plasmonic based metal probe tip and still achieves comparable light enhancement.

Chapter 6

Applications in biosensing and imaging

In this chapter, biological applications of the proposed grating coupler and slotted PhC nano-resonator based probe tip are analyzed using numerical modelings on biological water membrane impact of near-field light confinement performance, and enhanced subwavelength Cy5 fluorescence signal detection. The first section includes the simulation of the typical biological application to verify the performance of the proposed nano light confinement of PhC probe tip under water rich environment. The embedded metallic grating coupler itself can also serve as a μm scale fluorescence signal extraction device as investigated in the second section. The second section also includes the modeling results of Cy5 fluorescence signal detection at emission wavelength 690nm by the $\lambda/4$ slot embedded in 1W PhC waveguide with structure parameters optimized at the excitation wavelength at 632.8nm.

6.1 Biological application of photonic crystal based probe tip

In chapter 5.1, a pseudo-1W based PhC nano slot resonator probe tip is demonstrated to have $\lambda/15$ level light confinement at the near-field. However due to the limit size of the 1W line defect, the air holes that forms the nano resonator has critically small gap distance between the air hole edge and that of the nano slot, which increases the requirement on the patterning accuracy during the fabrication. To lessen the requirement, a pseudo 3 lines defect (3W) based PhC nano slot resonator probe tip is designed to have near-field light enhancement and confinement compared to that of the non-resonator case. The FDTD modeling in this section in 2D form, so as the PBG diagram calculation.

6.1.1 Design parameters optimization

The 2D PhC material is formed by arranging triangular air holes with radius $r = 0.3a$, where a is the lattice constant, through substrate material, as shown in Figure 6.1(a). The minimum light confinement realized by the 2D PhC waveguide is around a half wavelength through a 1W defect [66]. Other light processing devices, such as the slot waveguide and nano-resonator, are needed to further confine light to the sub-wavelength level. The dielectric air slot waveguide provides a low loss transport mechanism for TE-mode light, where the electric field is linearly polarized in the y direction (Figure 6.1)(a)) [47]. The light intensity peak concentrates in the air slot region with the FWHM beam size proportional to that of the air slot due to the continuity boundary condition of the TE displacement field [46]. A slot PhC waveguide serves as the base structure by placing an air slot with size of $0.2a$ along the ΓK direction of the triangular lattice in the center of the waveguide defect. By setting $D_t = 1.48a$, which defines the distance between the bulk PhC air hole and the air slot, the PhC waveguide defect approximates a pseudo-3W defect size. With the larger D_t, the new design relaxes the critical fabrication requirement, as compared to the slotted 1W PhC waveguide design [66]. So the nano-resonator air holes later on can be placed around the center defect with ease without destructing the overall device features. The photonic band diagram, calculated by plane wave expansion method using a supercell, as indicated at the right of Figure 6.1(b), yields the guided mode, under which the optimal lattice size can be derived [20]. A guided mode in the gap center is chosen near the first Brillouin zone

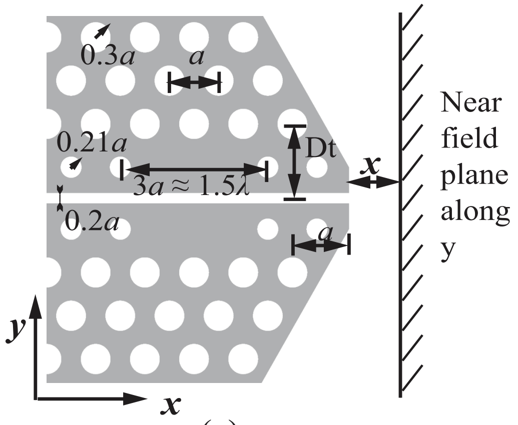

(a)

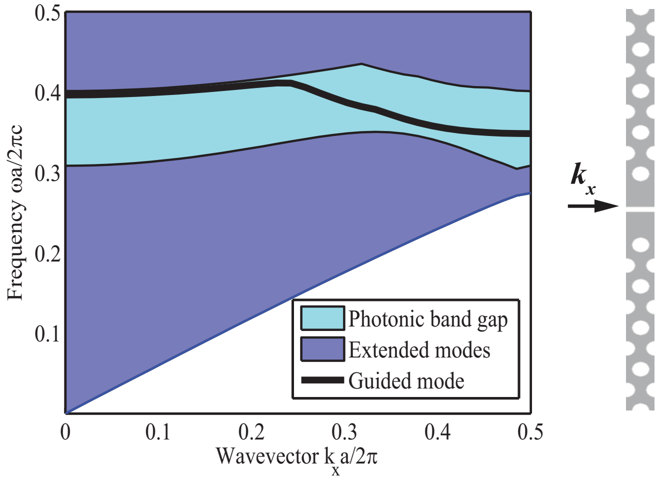

(b)

Figure 6.1: Design of 2D slot FP PhC nano-resonator based probe on triangular air holes lattice for 3W waveguide. (a) Probe design illustrated in terms of lattice constant a where $D_t = 1.48a$. White and gray color represent air and low refraction index material respectively. (b) Projected band structure along x direction of the slot PhC waveguide without nano-resonator formed by air hole radius of 0.3a (refraction index $n = 2 : 02$) for TE mode with the super cell lattice shown on the left.

edge for the device design, because the magnetic field (Hz) distribution pattern is symmetric in the y direction for the TE mode, which excites symmetrically across the slot and provides light localization in the slot region. At the chosen guided mode, there is

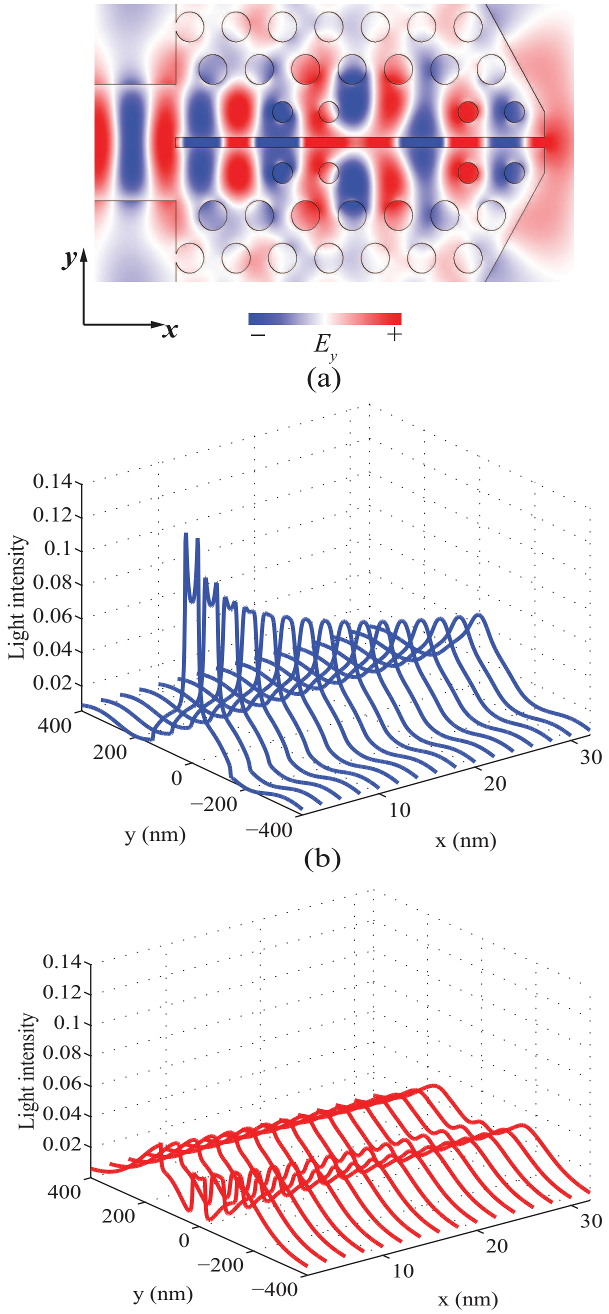

(a)

(b)

(c)

Figure 6.2: FDTD analysis of light confinement on probe without any perturbations. (a) Surface plot of electric field $|E_y|_{max}$ distribution pattern of the slot PhC FP probe with bulk PhC index $n = 2.02$. (b) Light intensity distribution at near-field of the probe, where x is the near-field distance from the tip aperture, ranging from 0 to 30nm with 2nm step. (c) Light distribution at near-field of the probe without embedding nano-resonators.

$\frac{\omega}{2\pi c} = 0.356$, where c is the speed of light in free space. For wavelength $\lambda_0 = 632.8$nm, the lattice constant a is derived as $a = 0.356\lambda_0 = 226$nm, and the slot size $0.2a$ equals 45nm, which decides the minimum feature size of the overall device. The probe tip is shaped by removing the bulk PhC air holes along the ΓK direction, forming a 120° cone probe body. The probe body side cutting edges are aligned with the next line bulk PhC air hole edges. The final flat aperture surface is aligned in the y direction positioned $0.5a$ in the x direction away from the nearest mirror air holes. The probe is modeled by the FDTD method (Figure 6.2) with a grid size of 2nm and a PML thickness of 1μm surrounding the four boundaries of the calculation domain to reduce the reflections errors [94, 89]. A TE light source with a Gaussian profile launches in a rectangular ridged waveguide with the same size of the PhC center defect. The FDTD calculation is converged after launching the source for time that allows the waves to propagate through the whole structure for at least 20 times and reaching a steady state before collecting the data at the monitoring planes. Performance of the probe is assessed in the near-field distance ranging from 0 to 30nm with a step size of 2nm. For straight slot PhC waveguide termination, there are strong reflections back to the probe body due to the PhC–air boundary, and the center peak inside the slot also splits into two strong side lobes (Figure 6.2(c)), which is not fit for near-field light confinement purposes.

In order to make a near-field light confinement tip, a FP resonator, formed by two smaller mirror air holes anchored in the bulk lattice position with radius of $0.7r$ along the sides of the air slot (Figure 6.2(a)), is incorporated in the slotted PhC waveguide to enhance the light throughput and block the strong side lobes to make it a single peak probe at the near-field. The cavity size of the FP resonator is around 1.5λ (λ is the wavelength in the substrate medium) by isolating mirroring holes with distance of $3a$ to form a constructive interference [96]. As the distance from the tip aperture increases, the center light intensity decreases but the single peak is kept all the way to a 30nm near-field distance. At a 10nm near-field distance, the FWHM of the light beam is 87.8nm, which is about $\lambda/7$ with peak intensity of 7.6%, twice of that of the one without the resonator (all the light intensity is normalized to the light source intensity peak). In the vertical cross section, the light is confined in the waveguide layer through TIR. Thus at the near-field, the light is confined in the 3D with single one peak which is suitable for near-field light confinement purpose.

6.1.2 Bulk photonic crystal refraction index and water perturbations

Because the near-field light confinement is in the sub-wavelength level and very close to the tip aperture, it is necessary to study the light distribution changes due to the impacts from both the refraction index changes in the PhC substrate and the higher refraction index object at the near-field. A flat water medium with refraction index of 1.33 is placed 10nm away from the tip aperture (Figure 6.3(a)), because the normal near distance control for the near-field imaging system is most accurate in the $<$ 10nm range [47]. This kind of configuration mimics the scenario of biological imaging applications, because most cells have high water content, with only a 4-5nm lipid bilayer cell membrane [48]. Two monitoring planes at the near-field of 5 and 15nm along the y direction are chosen to assess the probe near-field focusing capabilities in terms of the FWHM and center peak intensity of the light beam as functions of the PhC substrate refraction index ranging from 1.97 to 2.07, which is about ±2.5% from the typical Si_3N_4 index ($n = 2.02$) (Figure 6.3 (b) and (c)). Perturbation from the refraction index change of the bulk PhC causes beam splitting for a refraction index greater than 2.04. For an index ranging from 1.97 to 2.04, the FWHM is always less than 200nm for all scenarios, and

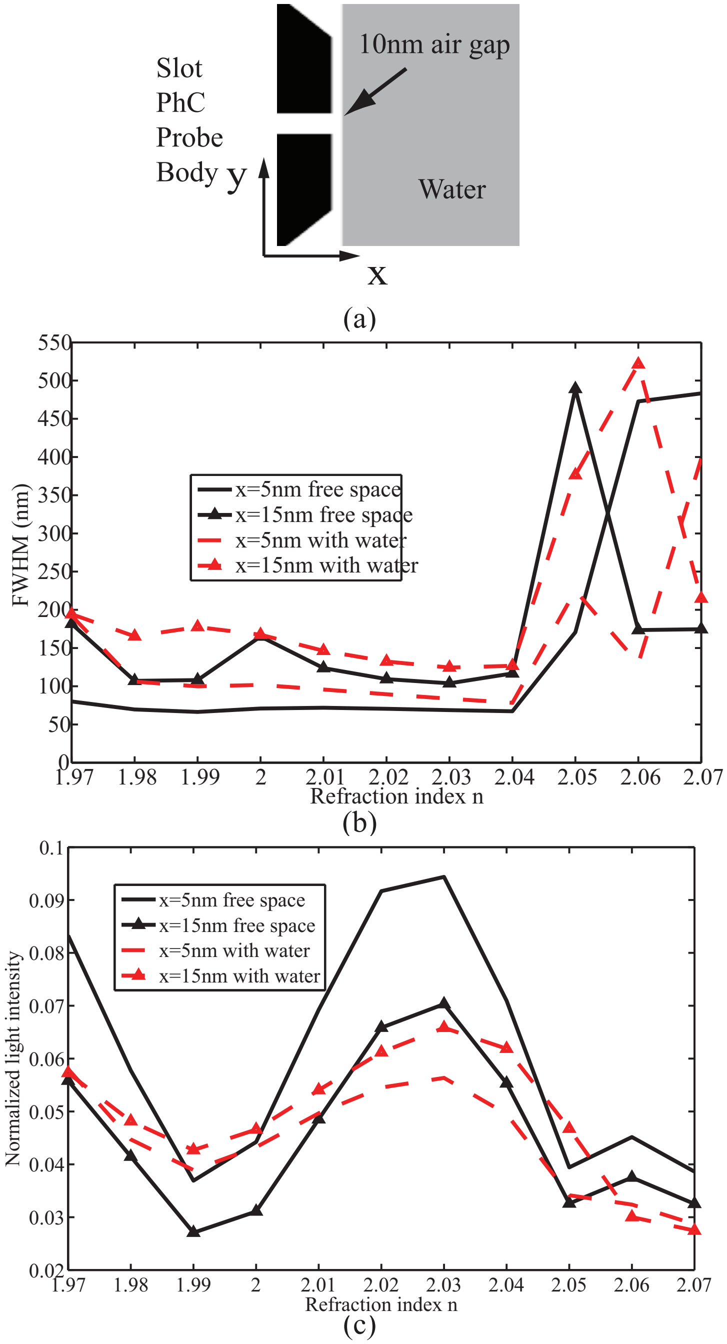

(a)

(b)

(c)

Figure 6.3: Perturbations on light confinement.(a) Illustration of water medium at the near-field of the probe tip with 10nm air gap between tip and water film. (b) FWHM plot of the light center peak and (c) normalized center peak intensity in 5nm and 15nm near-field distance with PhC bulk refraction index varying from 1.97 to 2.07 for both free space case and water film case at the near-field.

due to the impact from the water medium at the near-field, the FWHM increases slightly about 30nm in the center index range from 2.00 to 2.04. The “concave lens” effect, due to the near-field distance between the probe tip and water film, causes the spreading of the wave front that enlarges the beam size at the near-field.

In conclusion, the near-field focusing effects of the slotted FP PhC nanoresonator of low in-plane index contrast and a pure dielectric material can provide subwavelength light confinement at the visible wavelength of 632.8nm. The perturbation changes in the PhC substrate dielectric property cause beam splitting for refraction indices higher than 2.04. Perturbation from the water medium causes slight beam spreading, but it is still under the subwavelength range.

6.2 Fluorescence signal detection

Cy5 is a common cyanine based fluorescent dye that can be excited by HeNe laser (632.8nm) and has emission max around 690nm [70, 102]. Also Cy5, as water soluble, can be immobilized onto the Si_3N_4 surface evenly through covalent bonding with DNA or antibody probe [69]. Thus it is very useful to study the radiation pattern for fluorescence signal at wavelength of 690nm. In this section, two detection scenarios are simulated. The first one detects the far-field fluorescence signal directivity change in free space of the embedded metallic grating coupler. The fluorescence signal detection can be enhanced in the vertical direction and it avoids the excitation light contamination by angular differentiating the two in free space. The second modeling simulates a scenario for subwavelength excited fluorescence signal detection by the $\lambda/4$ slot resonator embedded in the 1W PhC waveguide. Due to the wide 3dB band gap in the PhC waveguide structure, the fluorescence emission signal at 690nm can also be detected with minimal out of plane radiation loss.

6.2.1 Enhanced detection by embedded metallic grating

Based on the effective refraction index, the 1^{st} order diffraction angle relates to the light wavelength in a way that the increase of wavelength reduces the coupling angle as predicted by equation (3.6). Thus by this nature of the device, the fluorescence signal can be differentiated from the excitation source by directivity change in free space. The radiation angle of the peak fluorescence signal at 690nm is predicted to be around $\theta_f = 0^\circ$ by equation (3.7).

Through 3D FDTD modeling of the exact same grating coupler structure as in Figure 4.5 for both Ag and Au materials, the radiation patterns are presented in Figure 6.4 for fluorescence light wavelength at 690nm under TE mode excitation. The peak directivities of both metallic grating couplers are pointing towards vertical direction into free space, which would reduce the source light coupling contamination at $\theta_1 = 10^\circ$ and enhance the signal to noise ratio by utilizing a low numerical aperture objective lens. The μm scale grating coupler device structure also enables the large scale fluorescence signal detection on one single chip for system integration purpose. The Ag grating coupler yields smaller directivity towards the substrate and higher free space directivity. Similar to the case of the 632.8nm wavelength, due to the material loss difference, the Ag grating coupler still has slightly higher radiation intensity at the 1^{st} order diffraction angle. Since the grating couplers are optimized for tilted radiation at $\theta = 10^\circ$, the overall radiation efficiencies for Ag and Au grating couplers for fluorescence signal are 50.54% and 43.71% respectively. The reduction of the radiation efficiencies is also caused by the larger penetration depth for longer wavelength and smaller tilted angle as predicted by equation (4.3). Also there is slight stronger impedance or mode mismatch between

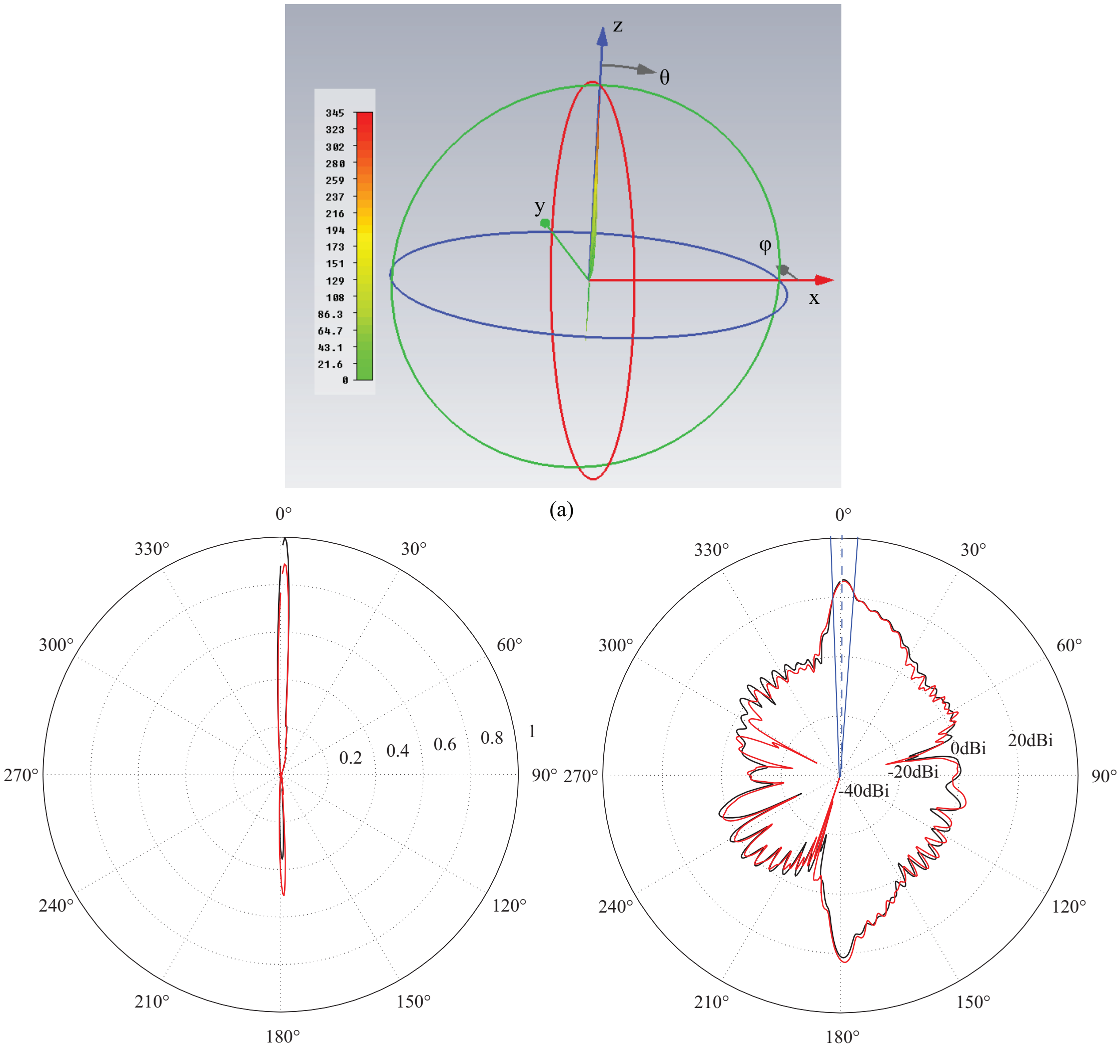

(a)

(b) (c)

Figure 6.4: Far-field radiation pattern for fluorescence wavelength at 690nm. (a) 3D directivity pattern as functions of spherical angles for Ag grating coupler with peak directivity of 345; (b) Normalized far-field power radiation pattern as function of θ on φ = 0° plane; (b) Far-field directivity as function of θ on φ = 0° plane in unit of dBi. The black curve represents Ag grating and red one is for Au grating.

the rib dielectric waveguide and the grating coupler that causes the efficiency decrease.

6.2.2 Tip enhanced detection

Since the very intense light can be confined in subwavelength scale at the near-field of the $\lambda/4$ slot embedded in PhC waveguide as introduced in section 5.2.3, it is possible to excite the Cy5 fluorescence molecules using extremely focused light at the probe tip. Thus it is meaningful to study the reverse process for subwavelength localized fluorescence light detection by the same probe tip. As it is observed by Figure 5.8(b) of the S_{21} plot, the 3dB transmission window covers the 690nm wavelength of the Cy5 emission peak for 632.8nm excitation. It is possible to reversely transform the polarized fluorescence signal in nanometer scale into the traveling wave of the rib dielectric waveguide due to the transmission window of the PhC waveguide. And such traveling wave continues to propagate back to the compact embedded metallic focus grating coupler region to further differentiate in free space by far-field imaging methods as illustrated in section 6.2.1.

The near-field localized fluorescence light detection by $\lambda/4$ slot PhC probe tip is almost a reciprocal problem as the light confinement process. However it is not exactly a reciprocity one due to the fact that the wavelength difference between the incident excitation light and the fluorescence light. So a 3D FDTD model is necessary to assess the fluorescence light detection performance of such a probe tip. In such a numerical model as illustrated in Figure 6.5, the probe tip has the same structure design as that of Figure 5.13, which has 284nm PhC lattice size, 20nm slot width and $\lambda/4$ long slot from the tip aperture. The PhC has single line center defect for maximal light delivery by working in the PBG center for 632.8nm wavelength. However the structure is illuminated from a waveguide port source at $x = 50$nm with port size plane of 80nm in y direction and 250nm in z direction with fluorescence light signal at 690nm wavelength linearly

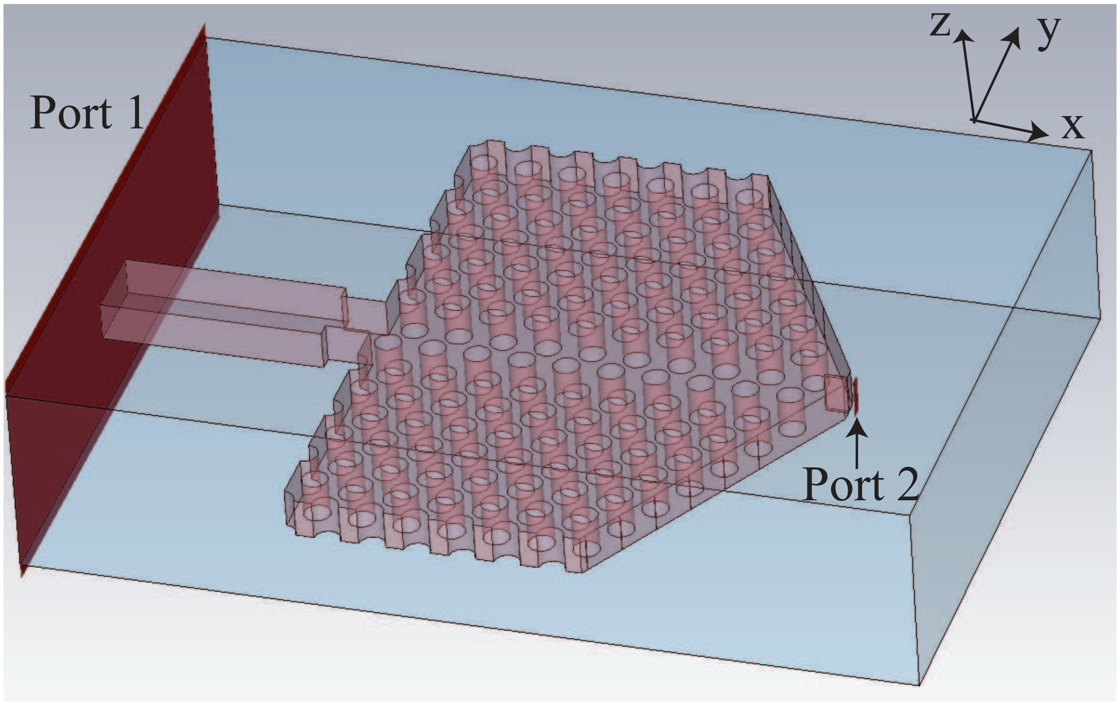

Figure 6.5: Reverse detection model for localized and linearly polarized near-field fluorescence signal of wavelength at 690nm. The PhC has 284nm lattice constant with slot width of 20nm and $\lambda/4$ slot length. The fluorescence waveguide port has geometry of 80nm in y and 250 in z direction located at $x = 50$nm at the near-field of the probe tip.

polarized in y direction. Such a waveguide port size is delicately chosen to model the light diffuse size at the $x = 50$nm yz cross plane for the light confinement source from the probe tip at 632.8nm wavelength. The single mode for such waveguide port is linearly polarized in y direction. The polarization of the fluorescence signal depends not only on the polarization of the excitation source (in this model the excitation source is linear polarized in y direction), but also the local medium composition. For biological system the constituents of the local medium varies for different experiment scenarios. Thus the linearly polarization for the fluorescence signal is assumed only to simplify the problem.

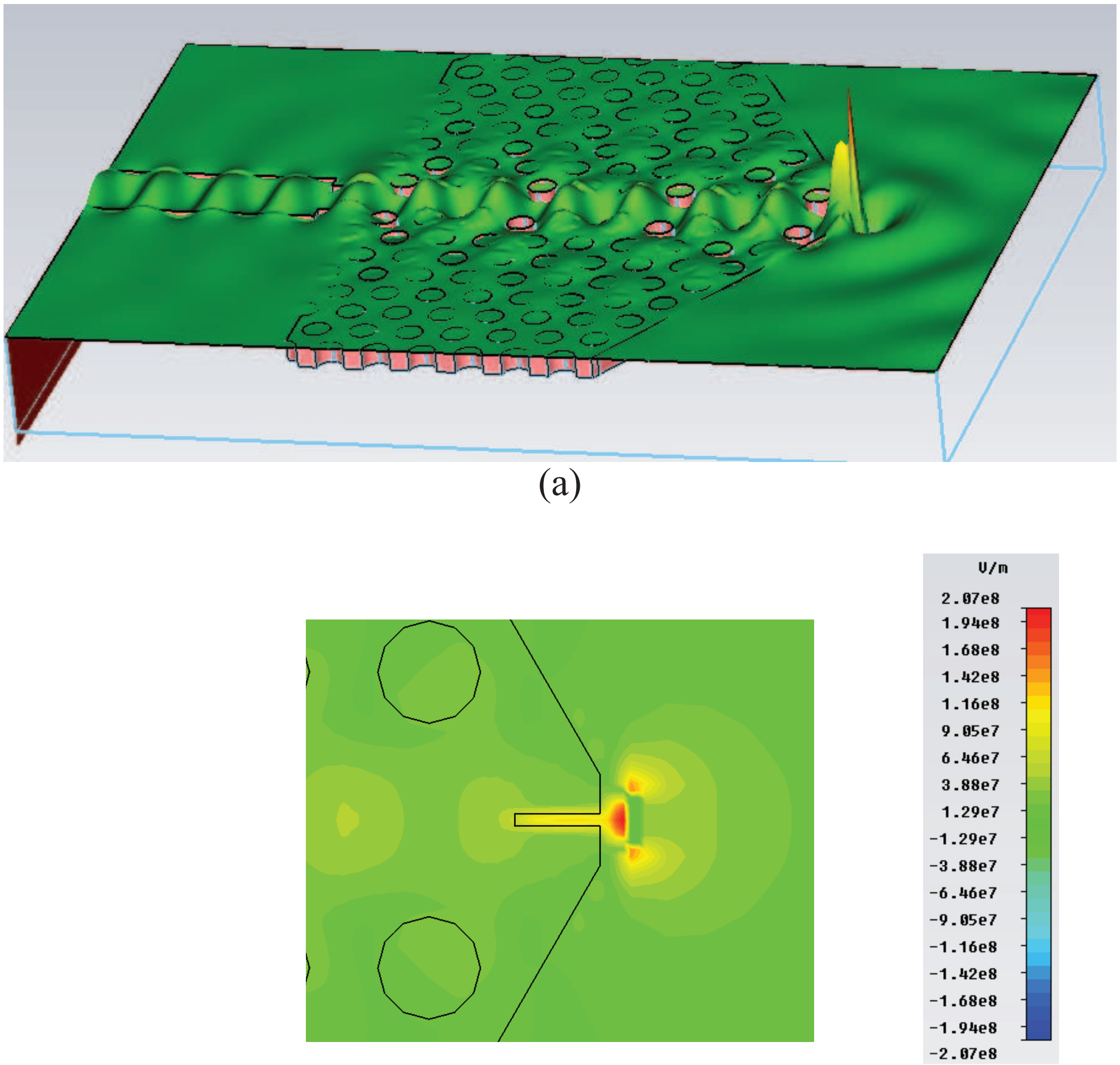

(a)

(b)

Figure 6.6: E_y distribution plots on the xy center cross plane for 690nm fluorescence waveguide port excitation at $x = 50$nm near-field yz plane. (a) E_y 3D surface plot on center xy cross plane; (b) Close up plot of $|E_y|$ amplitude around probe tip aperture on xy cross plane.

The 3D surface plot field distribution of E_y field component on xy center cross plane is shown in Figure 6.6(a), and the enlarged close up plot around tip aperture is shown in 2D surface plot in Figure 6.6(b). Similar to the 632.8nm wavelength excitation

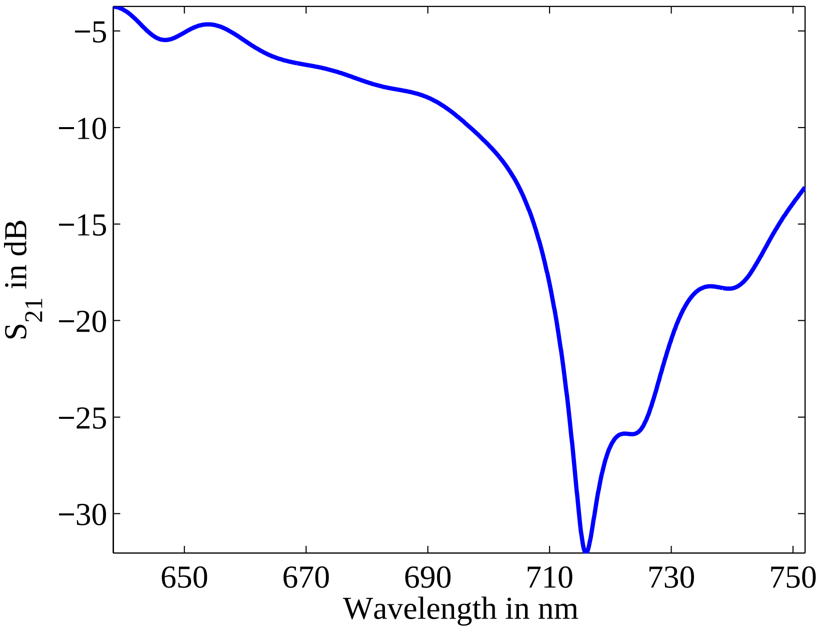

Figure 6.7: S_{21} of the fluorescence waveguide port (port 2) excitation at $x = 50$nm near-field yz plane as a function of wavelength with range center at 690nm. The waveguide port 2 locates at the dielectric rib waveguide.

field distribution, there is also light resonance near the probe tip aperture, but at the near-field of the probe. And the light is confined the slot region with higher intensity. This demonstrate higher light intensity in the slot region is not strong wavelength dependent. Instead the light polarization plays a much more important role. Traveling wave in single mode wave form propagates towards the rib dielectric waveguide direction. The transmission S_{21} parameter is also calculated as a function of wavelength with range center at 690nm in Figure 6.7. Compared to the S_{21} at 632.8nm, there is about 3dB drop for fluorescence wavelength at 690nm. This conforms with the PhC waveguide design in Figure 5.8(b). So the fluorescence light transmission drop is largely caused by the light loss in out of plane radiation form in the PhC waveguide structure.

6.3 Summary

In this chapter, the biological application simulations of the proposed light confinement structure in previous chapters have been modeled. The slotted center placed nano resonator embedded in pseudo-3W PhC waveguide is assessed for the perturbations coming from the water membrane at the near-field and the PhC dielectric index changes. The proposed structure is robust to handle such perturbations by keeping light confinement size still under subwavelength level. The Cy5 fluorescence detection and differentiation simulations are implemented for both embedded metallic grating coupler and the $\lambda/4$ slot resonator embedded in 1W PhC waveguide. The embedded metallic grating structure provides a way to detect fluorescence in the vertical direction. The $\lambda/4$ PhC resonator probe tip has been found to be able detect subwavelength fluorescence signal at the near-field of the probe tip. The proposed $\lambda/4$ PhC resonator probe tip shows the light confinement and Cy5 fluorescence detection capabilities on one single probe tip platform for subwavelength fluorescence excitation and emission detection.

Chapter 7

Conclusion and future works

The goal of this research is to find an alternative near-field light confinement probe design on scanning probe with enhanced transmission and zero Ohmic loss. During the pursuit process two novel light processing devices, embedded metallic grating coupler and PhC nano resonator based light confinement probe tip, have been proposed and studied by numerical methods.

Thin metallic films by Au and Ag are applied as an active grating layer to direct light from the dielectric waveguide into the free space with enhanced directivity. The dispersive optical properties of metal are well considered in the numerical modeling. The mathematical relationship between the tilted radiation angle and grating ellipses equations are developed and numerically verified. The performance of such grating couplers are analyzed in terms of optical antenna far-field directivity and gain patterns. The high tilted angle embedded metallic grating coupler shows higher transmission rate and far-field directivity with minimal light loss into the substrate layer. For the first time the under-waveguide layer metallic grating structure is proposed at visible wavelength to have higher transmission rate and is compatible with planar silicon micro-machining fabrication technology with more tolerance on fabrication error. The light enhancement factor of $\times 282$ from free space laser beam intensity to the dielectric waveguide is demonstrated. Such a compact focus grating coupler can be applied in large scale to make a dense coupling bridging system between the subwavelength near-field and the far-field optics.

Another original contribution in this research is the proposed nano resonator based PhC probe tip for near-field light confinement with totally pure dielectric material. The PhC material serves a very good light insulator and feed source for the nano resonators. The first group of nano resonator is based on center placed slotted nano resonator inside the center defect of the PhC waveguide. Light enhancement in subwavelength scale is demonstrated. The second group of nano resonator is based on the $\lambda/4$ slot resonator embedded in the PhC single line defect waveguide. A transmission line impedance match model is proposed for such a $\lambda/4$ slot resonator. Enormous light enhancement has been observed for such structure due to delicate mode match design on the probe tip. The "air rod" optical antenna concept for subwavelength light confinement is for the first time proposed and verified by both the mathematical model and the numerical modeling results. The total light confinement intensity achieves $\times 1185.41$ enhancement factor with beam size of $\lambda/20$ well beyond the transmission rate of the plasmonic based or pulled metal coated optical fiber based light confinement probe tip designs.

Potential biological application scenarios has been simulated by the numerical methods. Cy5 fluorescence differentiate capabilities in free space by the embedded metallic grating coupler have been modeled to find an efficient way to detect it in the free space. Cy5 fluorescence excitation and emission detection has been integrated on the same probe tip platform. The proposed $\lambda/4$ probe tip can both excite the Cy5 fluorophore molecules and detect the fluorescence signal in subwavelength scale. The fluorescence signal can be converted to the dielectric rib propagation mode and be further detected in free space by the proposed embedded metallic grating coupler structure.

Appendix C documents the preliminary fabrication and optical testing for the proposed device design in this thesis. The recommendations for future work include 3D PhC structure for 3D subwavelength light confinement, multi-wavelength device design, nano-LED and quantum dot device integration. Many other research possibilities can be based on such monolithic based probe tip system for near-field and far-field optics conversion.

Appendices

Appendix A

CAMFR code for calculating the reflection and out-of-plane coupling of the etched grating coupler

```
####################################################################
#
# Simulate 1D grating made on Si3N4 material. This simulation is 2D.
# It will calculate the reflection and coupling efficiencies of the
# light coupling structure on 2D basis. Even the grating iteself is
# 1D. The calculation is based on 2D cross section along the vertical
# direction.
####################################################################
from camfr import *
# Set parameters.
# Specify the light wavelenegth
set_lambda(0.6328)
set_N(130)
set_polarisation(TE)
set_chunk_tracing(0)
set_degenerate(0)
set_orthogonal(False)

# Create materials.
SiO2  = Material(1.46)
SiN   = Material(2.02)
air   = Material(1)
# Si    = Material(3.914)
# Assume SiO2 substrate
Si    = Material(1.46)

# Define each layer’s thickness
# H is defined as the whole computational thickness in x direction
```

```
H     = 10
SiO2T = 0.1
SiNT  = 0.25
airT  = (H/2)-(SiNT/2)
SiT   = (H/2)-(SiNT/2)-SiO2T

# Define how many period of the gratings
periods = 20
# Define slabs.

set_lower_PML(-0.4)
set_upper_PML(-0.4)

guided = 0
inc = zeros(N())
inc[guided] = 1

outfile = file("Data.out",'w')

# Print the reflectivity for different grating period.
# Define Grating thickness (Eg ranges from 50nm to 100nm with 10nm
# interval.

for Eg in arange(0, 0.25, 0.01):
    slab1 = Slab(Si(SiT)+ SiO2(SiO2T)+ SiN(SiNT-Eg) + air(airT+Eg))
    slab2 = Slab(Si(SiT) + SiO2(SiO2T) + SiN(SiNT) + air(airT))
    for L in arange(0.2, 0.6, 0.001):
        stack = Stack(slab2(2) + periods*(slab1(L/2) + slab2(L/2)) + slab2(2))
        stack.set_inc_field(inc)
        stack.calc()
        print Eg, L
        print >> outfile, L, abs(stack.R12(guided,guided))**2,
            abs(stack.T12(guided,guided)**2)
    free_tmps()
outfile.close()
```

Appendix B

VBA code to draw the ellipses in CST MW Studio

```
′  define material: Au_Drude
′  define units
With Units
     .Geometry "um"
     .Frequency "THz"
     .Time "s"
     .TemperatureUnit "Kelvin"
     .Voltage "V"
     .Current "A"
     .Resistance "Ohm"
     .Conductance "S"
     .Capacitance "PikoF"
     .Inductance "NanoH"
End With
With Material
     .Reset
     .Name "Au_Drude"
     .FrqType "all"
     .Type "Normal"
     .SetMaterialUnit "Hz", "um"
     .Epsilon "1"
     .Mue "1"
     .Kappa "0.0"
     .TanD "0.0"
     .TanDFreq "0.0"
     .TanDGiven "False"
     .TanDModel "ConstTanD"
     .KappaM "0"
     .TanDM "0.0"
```

```
     .TanDMFreq "0.0"
     .TanDMGiven "False"
     .TanDMModel "ConstTanD"
     .DispModelEps "Drude"
     .EpsInfinity "1"
     .DispCoeff1Eps "1.06136453404393E+16"
     .DispCoeff2Eps "281848942863495"
     .DispModelMue "None"
     .DispersiveFittingSchemeEps "1st Order"
     .DispersiveFittingSchemeMue "1st Order"
     .UseGeneralDispersionEps "False"
     .UseGeneralDispersionMue "False"
     .Rho "0"
     .ThermalType "Normal"
     .ThermalConductivity "0"
     .HeatCapacity "0"
     .MetabolicRate "0"
     .BloodFlow "0"
     .VoxelConvection "0"
     .MechanicsType "Unused"
     .Colour "1", "1", "0.501961"
     .Wireframe "False"
     .Reflection "False"
     .Allowoutline "True"
     .Transparentoutline "False"
     .Transparency "0"
     .Create
End With
’  execute macro: AuRings
Dim L0 As Double
Dim nt As Double
Dim Tc As Double
Dim neff As Double
Dim Xoff1 As Double
Dim ARadius1 As Double
Dim BRadius1 As Double
Dim Xoff2 As Double
```

```
Dim ARadius2 As Double
Dim BRadius2 As Double
Dim Zh As Double
Dim Qt As Double
Dim start_counter As Integer
Dim end_counter As Integer
Dim QCnt As Integer
start_counter = 1
end_counter = 20
L0 = 0.6328
nt = 1
Tc = 80*pi/180
neff = 1.7711
Qt = 20
For QCnt = start_counter To end_counter
ARadius1 = Qt*L0*neff/(neff^2-(nt*Cos(Tc))^2)
BRadius1 = Qt*L0/((neff^2-(nt*Cos(Tc))^2)^0.5)
Xoff1 = -Qt*L0*nt*Cos(Tc)/(neff^2-(nt*Cos(Tc))^2)
ARadius2 = (Qt-0.5)*L0*neff/(neff^2-(nt*Cos(Tc))^2)
BRadius2 = (Qt-0.5)*L0/((neff^2-(nt*Cos(Tc))^2)^0.5)
Xoff2 = -(Qt-0.5)*L0*nt*Cos(Tc)/(neff^2-(nt*Cos(Tc))^2)
With Ellipse
 .Reset
     .Name "Ellipses1"&QCnt
     .Curve "Curve"
     .XRadius ARadius1
     .YRadius BRadius1
     .Xcenter Xoff1
     .Ycenter 0
     .Segments "0"
     .Create
End With
With Ellipse
 .Reset
     .Name "Ellipses2"&QCnt
     .Curve "Curve"
     .XRadius ARadius2
```

```
     .YRadius BRadius2
     .Xcenter Xoff2
     .Ycenter 0
     .Segments "0"
     .Create
End With
With LoftCurves
 .Reset
     .Name "AuRing_"&QCnt
     .Component "AuRing"
     .Material "Au_Drude"
     .Solid "True"
     .MinimizeTwist "True"
     .AddCurve "Curve:Ellipses1"&QCnt
     .AddCurve "Curve:Ellipses2"&QCnt
     .Create
End With
Qt = Qt + 1
Next QCnt
```

Appendix C

Preliminary fabrication and optical testing

C.1 Silicon based fabrication

Fabrication flow based on Si micro-fabrication technology is presented for the embedded metallic grating coupler, as shown in Figure C.1. Before dicing, a 3μm thick SiO_2 layer is grown by thermal oxidation in wet thermal oxidation furnace on the Piranha cleaned 4 inches Si wafer. A 2cm $\times$ 2cm Si chip is then diced from the Si wafer in order to fit the Jeol 6000 EBL chip window size. Piranha wash of 20mins, and 5mins sonicating cleaning in acetone, IPA and DI water of the chips has been performed to remove any residue dust particles due to the dicing process followed with the nitrogen blow drying process. Since there are at least two device patterns, metallic gratings and dielectric rib waveguide, to be aligned in the proposed embedded grating coupler structure, the first step in the EBL pattern definition process is to define the global alignment markers, so that the following patterns can be aligned in sequence under nanometer accuracy. The Jeol 6000 EBL system requires the global alignment markers made by Au crosses with size of at least 3μm$\times$1mm.

For all the following EBL process, the electron beam resist Zep-520A is used. And for each metal liftoff process, PG remover is used to remove resist residue and the chips are then sonicating cleaned in acetone, IPA and DI water in sequential order followed by nitrogen blow drying. The Au global alignment markers are defined by EBL and deposited on SiO_2 layer by CHA electron beam evaporator with thickness of 100nm and adhesion layer of 5nm chromium (Cr) followed by Au liftoff in PG remover. The 40nm thick metallic grating layer made by either Au or Ag is aligned to the prior Au global alignment markers. After metal liftoff process, the Si chip is then deposited with Si_3N_4 by LPCVD nitride process with temperature peak at 800°C. The LPCVD is preferred than the PECVD due to the high optical quality of the Si_3N_4. The LPCVD recipe uses dichlorosilane (DCS) and ammonia to form the 250nm thick Si_3N_4. During the LPCVD process, the Au global alignment markers are also be covered up with smaller Si chips to make them exposed during the following EBL process. Otherwise due to the non-conductive nature of Si_3N_4, it is very difficult for EBL equipment to detect the Au

(a) Define global alignment markers by Au lift off (Au thickness ~ 100nm) on SiO_2 layer by EBL pattern. Thin layer ITO (20nm) or Espacer 300Z is used as charge dissipating layer. Zep520A used;

(c) LPCVD Si_3N_4 deposition to form the 250nm waveguide layer;

(b) Align Au or Ag (40nm) grating structure by 2nd EBL pattern. Zep520A used;

(d) Align waveguide structure by 3rd EBL pattern. Zep520A used. Then RIE dry etching through Si_3N_4 layer to finalize device.

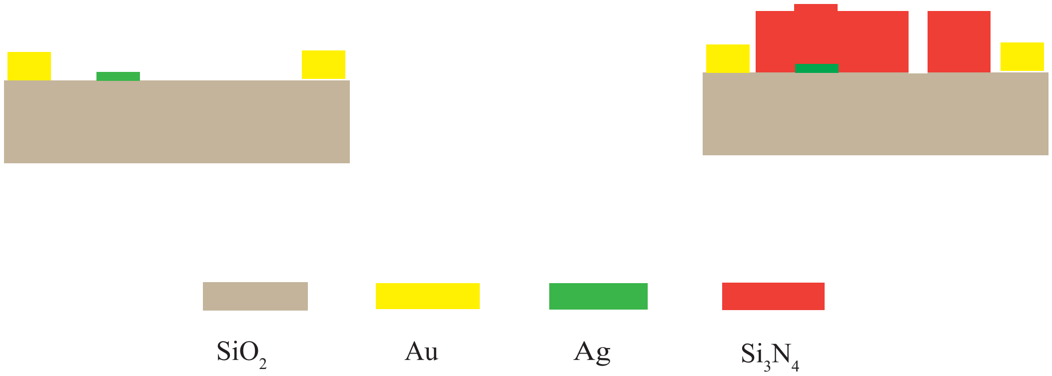

Figure C.1: Embedded metallic grating coupler fabrication flow by Si micro-fabrication technology.

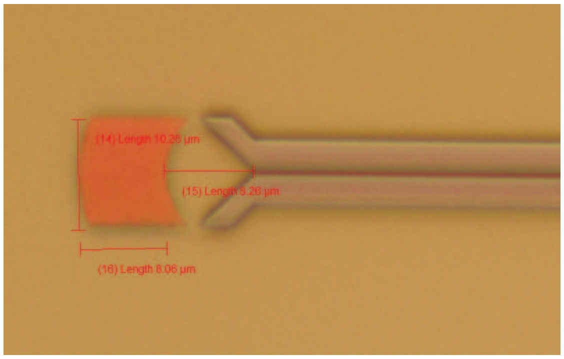

Figure C.2: Embedded Au grating coupler aligned with Si_3N_4 rib waveguide.

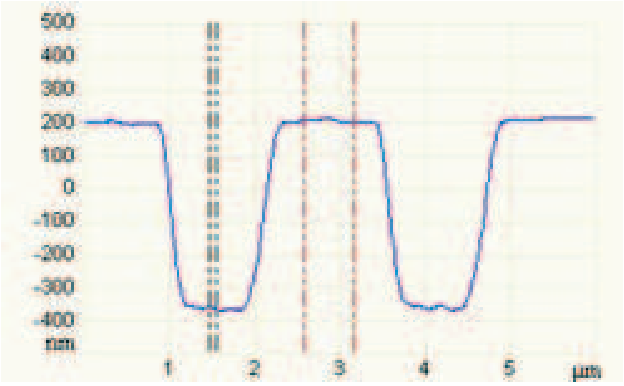

(a) Step size measurement of the ridged waveguide before removing the Zep520A after 5mins RIE etching on SiN layer. Step size is around 568nm.

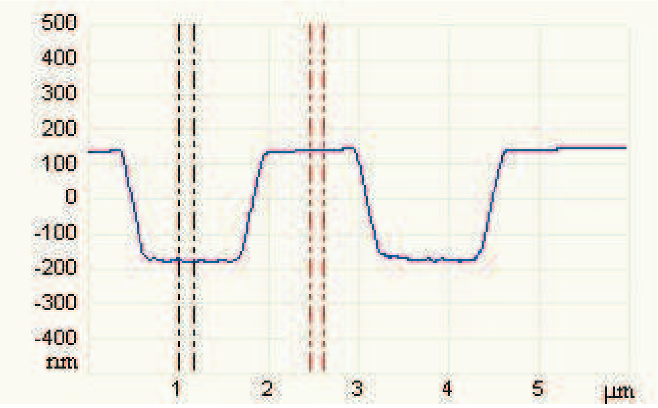

(b) Step size measurement of the ridged waveguide after stripping the resist. Step size is about 314nm.

(c) Topographical view of the ridged waveguide by AFM.

Figure C.3: Step size measurement on ridged waveguide area by AFM.

global alignment markers underneath 250nm Si_3N_4 layer. For mature fabrication process, this simple Si chip trick should be replaced with photolithography and dry etching the Si_3N_4 layer that covers up the Au global alignment markers.

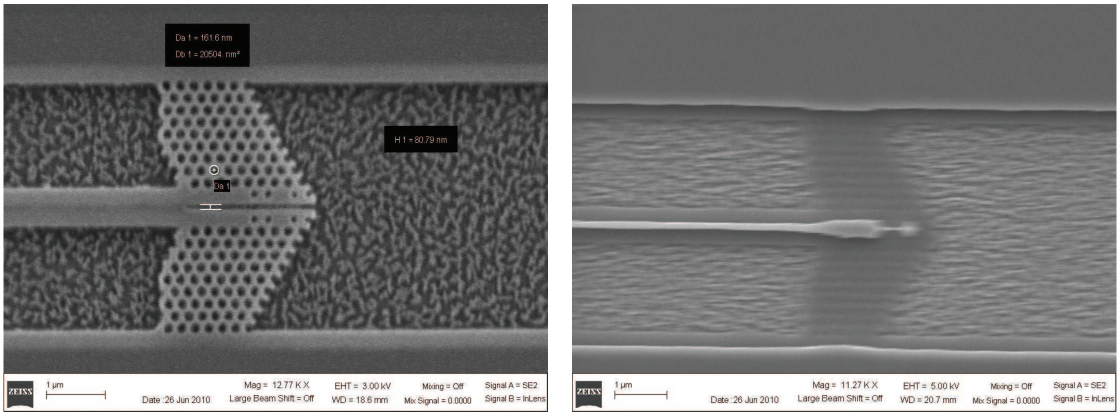

(a) Before removing Cr layer; (b) After removing Cr layer.

Figure C.4: PhC probe tip fabrication failure for Cr hard mask patterning transfer.

Finally as shown in Figure C.2 the rib waveguide structure is defined and aligned in EBL through Au global alignment markers followed by the reactive ion etching (RIE) process to etch off the Si_3N_4 layer to form the structure. During the same EBL patterning process for rib waveguide, the PhC probe tip on planar platform can also be defined. During the initial trial and error process, hard mask dry etching method through pattern transfer from Cr pattern to the Si_3N_4 layer fails due to the strong under etching effects as show in Figure C.4.

Thus the direct drying etching by Zep-520A has been used to form the PhC device part since it has good dry etching selectivity around 1:1. Such a probe tip of Si_3N_4 layer grown by PECVD method is shown in Figure C.5. It also explains the surface bumps on the Si_3N_4 surface due to poor quality of PECVD grown nitride. Thus LPCVD nitride is the preferred method to grown Si_3N_4 waveguide layer.

The step size of the rib waveguide before and after removing the Zep-520A after RIE etching on Si_3N_4 layer for probe shown in Figure C.2 is measured by AFM scanning over the ridged waveguide area as shown in Figure C.3. The Si_3N_4 thickness is verified by ellipsometer measurement to be 250nm. The dry etching process in Figure C.3 demonstrates the over etching into the SiO_2 layer for about 64nm due to non-stopping layer etching used.

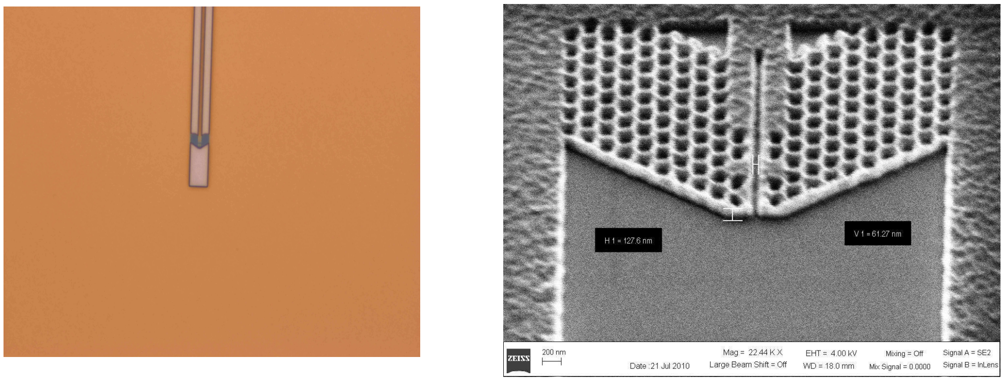

(a) Confocal microscopy image of the tip after RIE; (b) Side view of the tip after RIE;

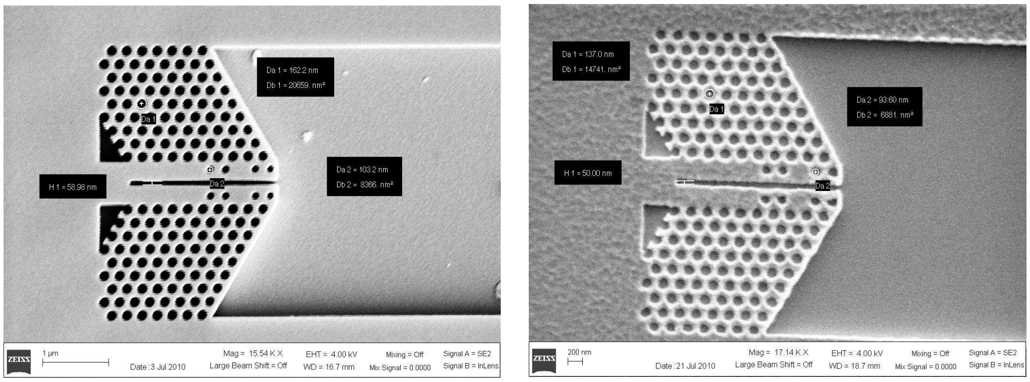

(c) After Zep520A developing; (d) Overview of the tip after RIE.

Figure C.5: PhC probe tip fabrication results on planar platform. The Zep-520A resist is used as dry etching mask.

In the meanwhile the ITO based probe fabrication has also been performed on silica chips, but not yet finalized. The ITO fabrication has its unique advantages in EBL process for its excellent conductivity to reduce the charging effects as commonly met by the Si_3N_4 waveguide material as shown in Figure C.6. The non-annealed ITO grown by sputtering method has been measured to have similar optical properties as that of the Si_3N_4 at 632.8nm HeNe wavelength. Thus all the modeling based on Si_3N_4 is also valid for the ITO based devices. However the tricky part for ITO probe fabrication is to define the waveguide pattern on ITO layer by either ITO liftoff or ITO dry etching. The ITO liftoff has the problem of resist pattern damage due to ITO bombardment in the ITO sputtering process. So ultra low energy and low pressure ITO sputtering process needs to be tailored to find the optimal recipe for ITO liftoff process to avoid the resist damage during the ITO liftoff. On the other hand the ITO dry etching can also be realized by HBr or HI dry etching. But the recipe needs further development for more accurate pattern transfer. The HI dry etching of ITO is preferred, but currently I do not have access to it.

C.2 Optical testing of the embedded metallic grating coupler

The optical testing for the proposed embedded metallic grating coupler has been performed by coupling the free space plane wave light source with the input/output grating couplers. The input grating coupler has an enlarged size about $100\mu m \times 160\mu m$ as illustrated in Figure C.6. Resist pattern damage has been observed due to the charging effects in EBL process. This kind of resist damage is unavoidable for high desnity features, especially at the feature center region where more charges are accumulated. Even the center has charge effect damage, the grating coupler in Figure C.6 can still be used for testing purpose due to the grating lines count defined in the edge region

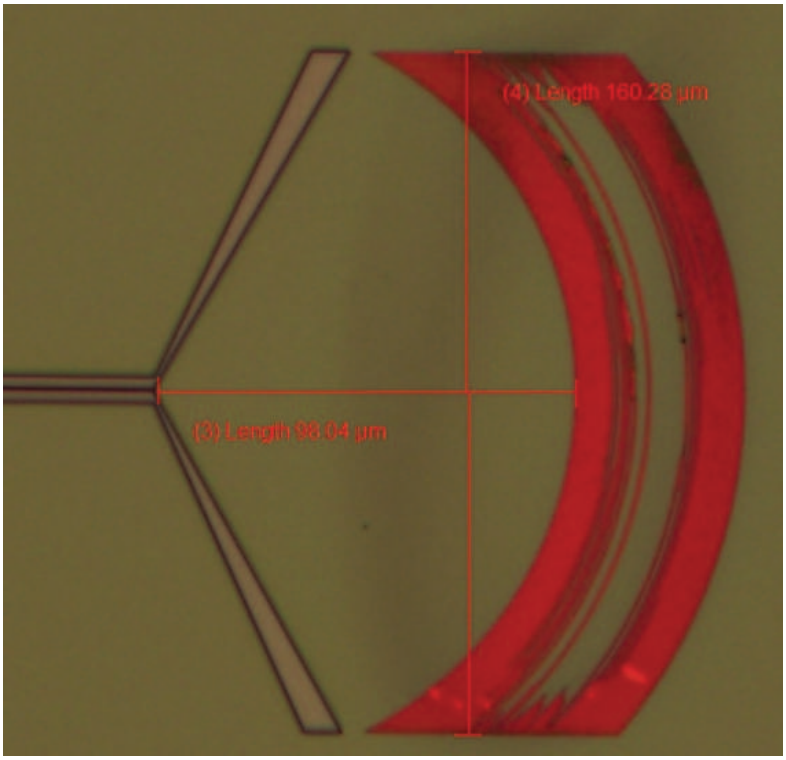

Figure C.6: Enlarged embedded metallic grating coupler tilted for $\theta = 10°$. The center pattern damage is caused by excessive charge accumulation during the EBL patterning process which is unavoidable for high density features.

is still large enough to stop light propagation in lateral plane direction. This is due to the shorter propagation distance caused by the plasmonic effects on the metallic grating layer as discussed in the modeling chapters. The output grating has smaller size of about 7μm×10μm as shown in Figure C.2 with the same size as defined in the previous modeling work.

Figure C.7 shows the optical measurement setup where a linearly polarized continuous HeNe laser source (632.8nm wavelength) with 18mW power rating is used as the light input source and the CMOS camera mounted with objective lens is used as the image collecting device. The laser source position is fixed while as the sample stage is mounted on a 3D translational stage with rotational angle control. The same is with the CMOS camera which also can be controlled with the rotational angle. The distance between the input and output grating couplers is 7mm in order to reduce the background noise. The idea in this setup is to collect more light from the input side by using larger grating size.

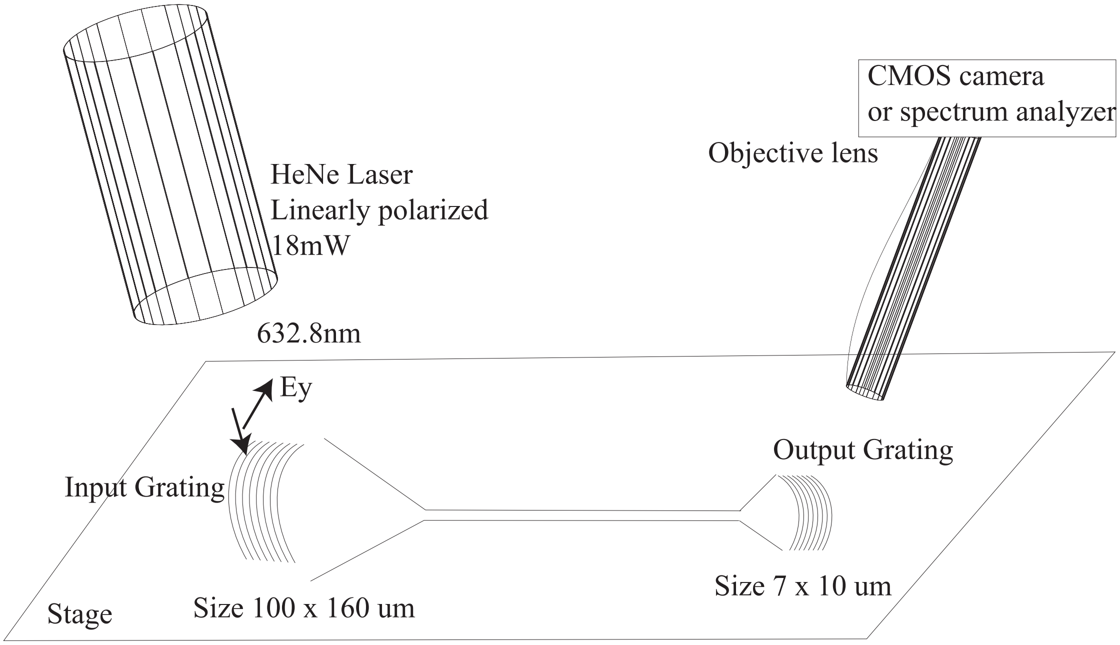

Figure C.7: Optical setup for input/output grating coupler measurement.

Figure C.8 show the scattering images collected when the input laser source is rotated at $\theta = 10^\circ$. The beam spot is observed at the entrance of the dielectric waveguide which demonstrates the light focusing effect of such a grating coupler. At the output

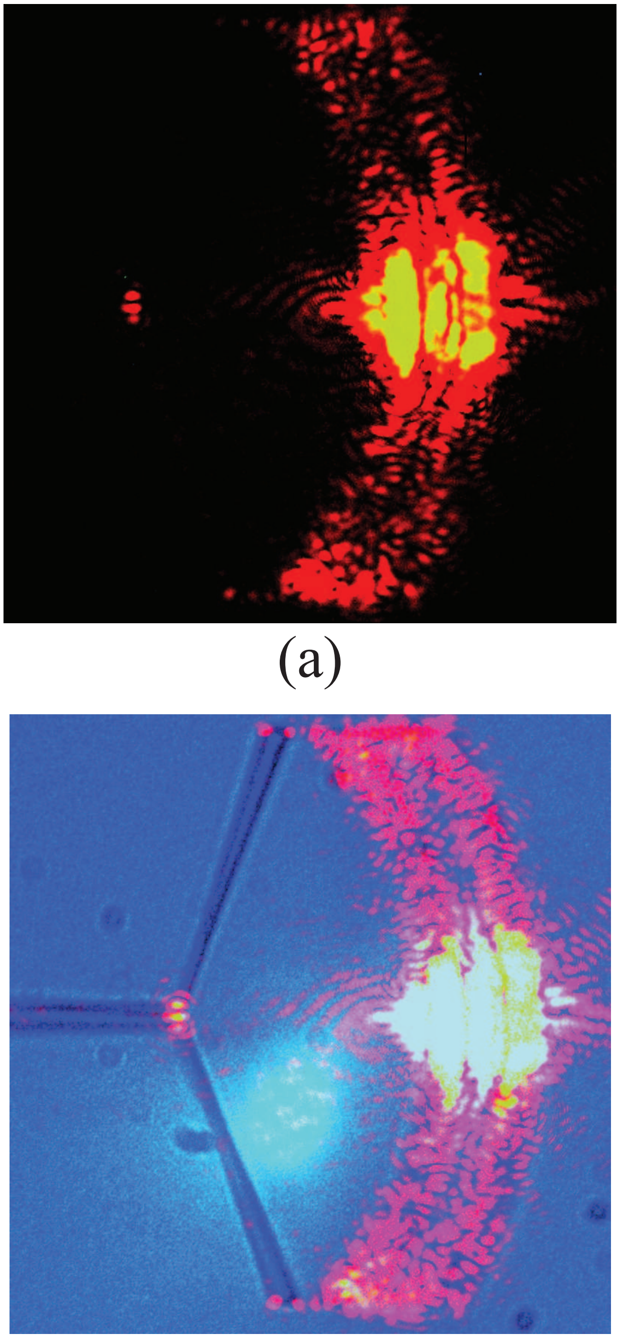

Figure C.8: Scattering image of the enlarged input grating coupler under linearly polarized light excitation at $\theta = 10^\circ$ for $\lambda = 632.8$nm. (a) image taken when ambient light turns off; (b) image taken when ambient light turns on (white LED).

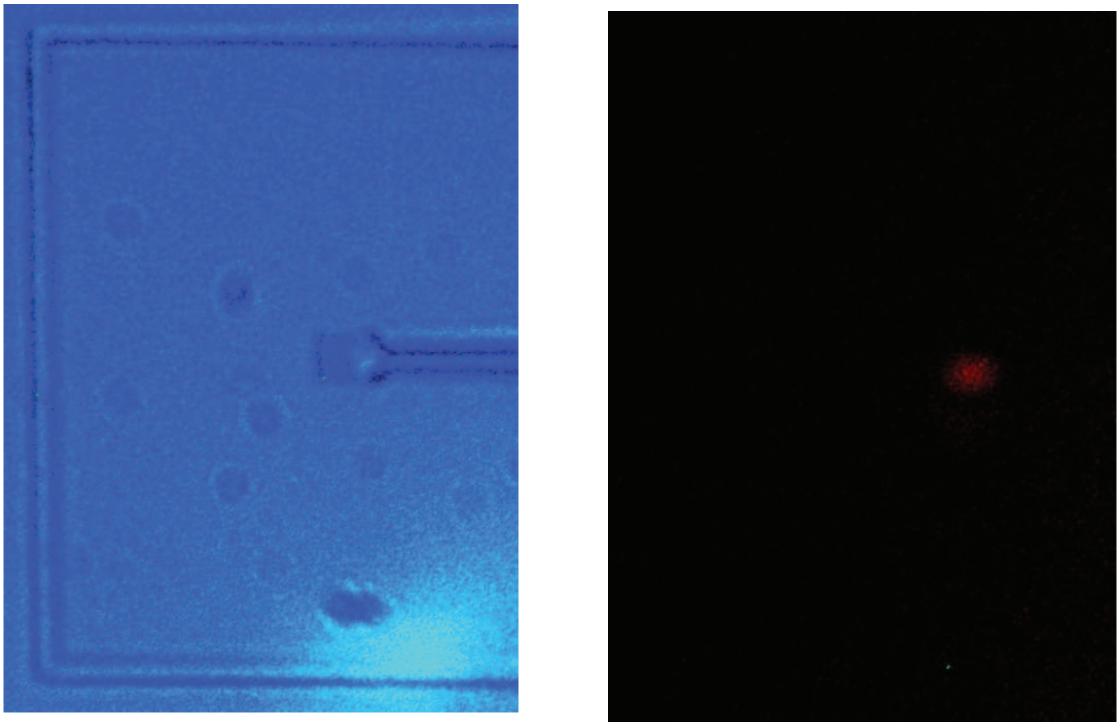

(a) (b)

Figure C.9: Output grating coupler light collection at θ = 10°. (a) ambient light on for imaging the device structure. The Au rectangular structure around output grating coupler is designed to help locating the structure; (b) Light spot observed at the output grating coupler region.

grating region, the light is collected at θ = 10° for maximum light coupling. Figure C.9 shows the light out coupling image from the output grating structure.

Bibliography

[1] Phan Ngoc Minh, Ono Takahito, and Esashi Masayoshi. *Fabrication of silicon microprobes for optical near-field applications*. CRC Press LLC, Boca Raton, Florida, 2002.

[2] E. H. Synge. A suggested method for extending microscopic resolution into the ultra-microscopic region. *Philosophical Magazine*, 6:356–62, 1928.

[3] M. Born and E. Wolf. *Principles of Optics*. Pergamon, Oxford, UK, 1987.

[4] D. McMullan. The prehistory of scanned image microscopy part 1: scanned optical microscopes. *Proc. R. Microsc. Soc*, 25:127–131, 1990.

[5] Eric Betzig and Jayk Trautman. Near-field optics: Microscopy, spectroscopy, and surface modification beyond the diffraction limit. *Science*, 257(5067):189–195, 1992.

[6] Lukas Novotny. From near-field optics to optical antennas. *Physics Today*, 6:47–52, July 2011.

[7] E. A. Ash and G. Nicholls. Super-resolution aperture scanning microscope. *Nature*, 237(5357):510–512, 1972. 10.1038/237510a0.

[8] G. Binnig, H. Rohrer, Ch. Gerber, and E. Weibel. Surface studies by scanning tunneling microscopy. *Phys. Rev. Lett.*, 49:57–61, 1982.

[9] D. W. Pohl, W. Denk, and M. Lanz. Optical stethoscopy: Image recording with resolution $\lambda/20$. *Appl. Phys. Lett.*, 44:651, 1984.

[10] A. Harootunian M. Isaacson E. Betzig, A. Lewis and E. Kratschmer. Near field scanning optical microscopy (nsom) development and biophysical applications. *Biophysical Journal*, 49:269–279, 1986.

[11] Bert Hecht, Beate Sick, Urs P. Wild, Volker Deckert, Renato Zenobi, Olivier J. F. Martin, and Dieter W. Pohl. Scanning near-field optical microscopy with aperture probes: fundamentals and applications. *J. Chem. Phys.*, 112:7761–74, 2000.

[12] H. J. Lezec, A. Degiron, E. Devaux, R. A. Linke, L. Martin-Moreno, F. J. Garcia-Vidal, and T. W. Ebbesen. Beaming light from a subwavelength aperture. *Science*, 297, 2002.

[13] Nicholas Fang, Hyesog Lee, Cheng Sun, and Xiang Zhang. Sub–diffraction-limited optical imaging with a silver superlens. *Science*, 308, 2005.

[14] Seungchul Kim, Jonghan Jin, Young-Jin Kim, In-Yong Park, Yunseok Kim, and Seung-Woo Kim. High-harmonic generation by resonant plasmon field enhancement. *Nature*, 453, 2008.

[15] Kunihiko Ishihara, Keishi Ohashi, Tomofumi Ikari, Hiroaki Minamide, Hiroyuki Yokoyama, Jun ichi Shikata, and Hiromasa. Terahertz-wave near-field imaging with subwavelength resolution using surface-wave-assisted bow-tie aperture. *Appl. Phys. Lett.*, 89, 2006.

[16] T. H. Taminiau, F. D. Stefani, F. B. Segerink, and N. F. van Hulst. Optical antennas direct single-molecule emission. *Nature Photonics*, 2, 2008.

[17] Nicholas E. Dickenson, Elizabeth S. Erickson, Olivia L. Mooren, and Robert C. Dunn. Characterization of power induced heating and damage in fiber optic probes for near-field scanning optical microscopy. *Review of Scientific Instruments*, 78(5):053712, 2007.

[18] Allen Taflove and Susan C. Hagness. *Computational electrodynamics: the finite-difference time-domain method*. Artech House antennas and propagation library. Artech House, Boston, 3rd edition, 2005.

[19] Peter Bienstman. *Rigorous and efficient modelling of wavelength scale photonic components*. PhD thesis, Universiteit Gent, 2001.

[20] Steven G. Johnson and J. D. Joannopoulos. Block-iterative frequency-domain methods for maxwell's equations in a planewave basis. *Opt. Express*, 8(3):173–190, 2001.

[21] Marko Lončar, Theodor Doll, Jelena kovi, and Axel Scherer. Design and fabrication of silicon photonic crystal optical waveguides. *Journal of Lightwave Technology*, 18:1402–11, 2000.

[22] Marko Lončar, Theodor Doll, Jelena kovi, and Axel Scherer. Quantitative measurement of transmission, reflection, and diffraction of two-dimensional photonic band gap structures at near-infrared wavelengths. *Phys. Rev. Lett.*, 79:4147–50, 1997.

[23] Edward D. Palik and Gorachand Ghosh. *Handbook of optical constants of solids*. Academic Press, 1998.

[24] T. N. Oder, J. Shakya, J. Y. Lin, and H. X. Jiang. Iii-nitride photonic crystals. *Appl. Phys. Lett.*, 83(6):1231–33, 2003.

[25] S. Combrié, S. Bansropun, M. Lecomte, O. Parillaud, S. Cassette, H. Benisty, and J. Nagle. Optimization of an inductively coupled plasma etching process of gainp/gaas based material for photonic band gap applications. *J. Vac. Sci. Technol. B*, 23:1521–26, 2005.

[26] Michael Barth, Nils Nüsse, Johannes Stingl, Bernd Löchel, and Oliver Benson1. Emission properties of high-q silicon nitride photonic crystal heterostructure cavities. *Appl. Phys. Lett.*, 93, 2008.

[27] G. Böttger, C. Liguda, M. Schmidt, and M. Eich. Improved transmission characteristics of moderate refractive index contrast photonic crystal slabs. *Appl. Phys. Lett.*, 81(14):2517–19, 2002.

[28] W H P Pernice, M Li, D F G Gallagher, and H X Tang. Silicon nitride membrane photonics. *J. Opt. A: Pure Appl. Opt.*, 11, 2009.

[29] R. Iliew, C. Etrich, M. Augustin, E.-B. Kley, S. Nolte, A. Tünnermann, and F. Lederer. Linear and nonlinear effects of light propagation in low-index photonic crystal slabs. *phys. stat. sol. (a)*, 204(11):3689–3707, 2002.

[30] M. E. Zoorob, M. B. D. Charlton, G. J. Parker, J. J. Baumberg, and M. C. Netti. Complete photonic bandgaps in 12-fold symmetric quasicrystals. *Nature*, 404:740–44, 2000.

[31] M. C. Netti, M. D. B. Charlton, G. J. Parker, and J. J. Baumberg. Visible photonic band gap engineering in silicon nitride waveguides. *Appl. Phys. Lett.*, 76:991–93, 2000.

[32] A. A. Michelson. On the application of interference methods to spectroscopic measurements. *The London, Edinburgh, and Dublin Philosophical Magazine and Journal of Science*, 31:338–46, 1891.

[33] S. L. McCall, P. M. Platzman, R. Dalichaouch, David Smith, and S. Schultz. Microwave propagation in two-dimensional dielectric lattices. *Phys. Rev. Lett.*, 67:2017–20, 1991.

[34] Robert D. Meade, Karl D. Brommer, Andrew M. Rappe, and J. D. Joannopoulos. Existence of a photonic band gap in two dimensions. *Phys. Rev. Lett.*, 61:495–97, 1992.

[35] E. Yablonovitch. Inhibited spontaneous emission in solid-state physics and electronics. *Phys. Rev. Lett.*, 58:2059–62, 1987.

[36] John D. Joannopoulos, Steven G. Johnson, Joshua N. Winn, and Robert D. Meade. *Photonic Crystals: Molding the Flow of Light*. Princeton University Press, Princeton, NJ, 2nd edition, 2008.

[37] Concita Sibilia, T. M. Benson, Marian Marciniak, and Tomasz Szoplik, editors. *Photonic Crystals: Physics and Technology*. Springer, 2008.

[38] D. Marcuse. *Theory of dielectric optical waveguides*. Academic Press, New York, 1974.

[39] Bradley Schmidt, Vilson Almeida, Christina Manolatou, Stefan Preble, and Michal Lipson. Nanocavity in a silicon waveguide for ultrasensitive nanoparticle detection. *Appl. Phys. Lett.*, 85(21):4854–56, 2004.

[40] Sudeep Mandal and David Erickson. Nanoscale optofluidic sensor arrays. *Optics Express*, 16:1623–31, 2008.

[41] A. Di Falco, L. O' Faolain, and T. F. Krauss. Chemical sensing in slotted photonic crystal heterostructure cavities. *Appl. Phys. Lett.*, 94, 2009.

[42] Qianfan Xu, Vilson R. Almeida, Roberto R. Panepucci, and Michal Lipson. Experimental demonstration of guiding and confining light in nanometer-size low-refractive-index material. *Optics Letters*, 29:1626–28, 2004.

[43] M. Galli, D. Gerace, A. Politi, M. Liscidini, M. Patrini, L. C. Andreani, A. Canino, M. Miritello, R. Lo Savio, A. Irrera, and F. Priolo. Direct evidence of light confinement and emission enhancement in active silicon-on-insulator slot waveguides. *Appl. Phys. Lett.*, 89, 2006.

[44] T. Baehr-Jones, M. Hochberg, G. Wang, R. Lawson, P. A. Sullivan Y. Liao, L. Dalton, A. K.-Y. Jen, and A. Scherer. Optical modulation and detection in slotted silicon waveguides. *Opt. Express*, 13:5216–26, 2005.

[45] T. Fujisawa and M. Koshiba. All-optical logic gates based on nonlinear slot-waveguide couplers. *J. Opt. Soc. Am. B*, 23:684–91, 2006.

[46] Vilson R. Almeida, Qianfan Xu, Carlos A. Barrios, and Michal Lipson. Guiding and confining light in void nanostructure. *Optics Letters*, 29:1209–11, 2004.

[47] C. A. Barrios, B. Sánchez, K. B. Gylfason, A. Griol, H. SohlstrBöm, M. Holgado, and R. Casquel. Demonstration of slot-waveguide structures on silicon nitride / silicon oxide platform. *Opt. Express*, 15:6846–56, 2007.

[48] A. Di Falco, L.O'Faolain, and T. F. Krauss. Dispersion control and slow light in slotted photonic crystal waveguides. *APPLIED PHYSICS LETTERS*, 92, 2008.

[49] A. Di Falco, L. O'Faolain, and T.F. Krauss. Photonic crystal slotted slab waveguides. *Photonics and Nanostructures – Fundamentals and Applications*, 6(1):38–41, 2008.

[50] T F Krauss. Slow light in photonic crystal waveguides. *J. Phys. D: Appl. Phys.*, 40:2666–70, 2007.

[51] Olav Solgaard. *Photonic Microsystems: Micro and Nanotechnology Applied to Optical Devices and Systems*. Springer Science+Business Media, LLC, 2009.

[52] P. Lalanne, C. Sauvan, and J.P. Hugonin. Photon confinement in photonic crystal nanocavities. *Laser and Photonics Reviews*, 2:514–26, 2008.

[53] Takasumi Tanabe, Eiichi Kuramochi, Akihiko Shinya, and Masaya Notomi. Ultrahigh-q photonic crystal nanocavities and their applications. In Andrey Matsko, editor, *Practical Applications of Microresonators in Optics and Photonics*, pages 1–52, Boca Raton, Florida, 2009. CRC Press.

[54] Feridun Ay, Askin Kocabas, Coskun Kocabas, Atilla Aydinli, and Sedat Agan. Prism coupling technique investigation of elasto-optical properties of thin polymer films. *Journal of Applied Physics*, 96(12):7147–7153, 2004.

[55] W. K. Burns and G. B. Hocker. End fire coupling between optical fibers and diffused channel waveguides. *Appl Opt*, 16(8):2048–50, 1977.

[56] Wang Qian, Loh Ter-Hoe, D. K. T. Ng, and Ho Seng-Tiong. Design and analysis of optical coupling between silicon nanophotonic waveguide and standard single-mode fiber using an integrated asymmetric super-grin lens. *Selected Topics in Quantum Electronics, IEEE Journal of*, 17(3):581–589, 2011.

[57] S. Scheerlinck, J. Schrauwen, F. Van Laere, D. Taillaert, D. Van Thourhout, and R. Baets. Efficient, broadband and compact metal grating couplers for silicon-on-insulator waveguides. *Opt Express*, 15(15):9625–30, 2007.

[58] Frederik Van Laere, Günther Roelkens, Melanie Ayre, Jonathan Schrauwen, Dirk Taillaert, Dries Van Thourhout, Thomas F. Krauss, and Roel Baets. Compact and highly efficient grating couplers between optical fiber and nanophotonic waveguides. *J. Lightwave Technol.*, 25(1):151–156, 2007.

[59] Christopher Doerr, Long Chen, Young-Kai Chen, and Larry Buhl. Wide bandwidth silicon nitride grating coupler. *IEEE Photonics Technology Letters*, 22(19):1461–1463, 2010.

[60] D. Taillaert, W. Bogaerts, P. Bienstman, T. T. Krauss, P Van Daele, I. Moerman, S. Verstuyft, K. De Mesel, and R. Baets. An out-of-plane grating coupler for efficient butt-coupling between compact planar waveguides and single-mode fibers. *IEEE Journal of Quantum Electronics*, 38:949–55, 2002.

[61] K. Hoshino, A. Gopal, and X.J. Zhang. Near-field scanning nanophotonic microscopy - breaking the diffraction limit using integrated nano light-emitting probe tip. *Selected Topics in Quantum Electronics, IEEE Journal of*, 15(5):1393–1399, 2009.

[62] K. Hoshino, L. Rozanski, D. A. Vanden Bout, and X.J. Zhang. Direct fabrication of nano-scale light emitting diode on silicon probe for near-field scanning optical microscopy. *IEEE/ASME Journal of Microelectromechanical Systems*, 17:4–10, 2008.

[63] Kazunori Hoshino, Lynn J. Rozanski, David A. Vanden Bout, and X.J. Zhang. Near-field scanning optical microscopy with monolithic silicon light emitting diode on probe tip. *Appl Phys Lett*, 92(13):131106–131106–3, 2008.

[64] Yuyan Wang, Yu-Yen Huang, and X.J. Zhang. Plasmonic nanograting tip design for high power throughput near-field scanning aperture probe. *Opt. Express*, 18(13):14004–14011, 2010.

[65] Youngkyu Lee, Andrea Alu, and X. J. Zhang. Efficient apertureless scanning probes using patterned plasmonic surfaces. *Opt. Express*, 19(27):25990–25999, 2011.

[66] Lingyun Wang, Kazunori Hoshino, and X.J. Zhang. Numerical simulation of photonic crystal based nano-resonators on scanning probe tip for enhanced light confinement, 2010.

[67] L. Wang, K. Hoshino, and X.J. Zhang. Light focusing by slot fabry-perot photonic crystal nanoresonator on scanning tip. *Opt Lett*, 36(10):1917–9, 2011.

[68] E. Dulkeith, A. C. Morteani, T. Niedereichholz, T. A. Klar, J. Feldmann, S. A. Levi, F. C. van Veggel, D. N. Reinhoudt, M. Moller, and D. I. Gittins. Fluorescence quenching of dye molecules near gold nanoparticles: radiative and nonradiative effects. *Phys Rev Lett*, 89(20):203002, 2002.

[69] Luigi Martiradonna, Ferruccio Pisanello, Tiziana Stomeo, Antonio Qualtieri, Giuseppe Vecchio, Stefania Sabella, Roberto Cingolani, Massimo De Vittorio, and Pier Paolo Pompa. Spectral tagging by integrated photonic crystal resonators for highly sensitive and parallel detection in biochips. *Appl Phys Lett*, 96(11):113702–3, 2010.

[70] I. D. Block, P. C. Mathias, N. Ganesh, S. I. Jones, B. R. Dorvel, V. Chaudhery, L. O. Vodkin, R. Bashir, and B. T. Cunningham. A detection instrument for enhanced-fluorescence and label-free imaging on photonic crystal surfaces. *Opt Express*, 17(15):13222–35, 2009.

[71] A. Pokhriyal, M. Lu, C. S. Huang, S. Schulz, and B. T. Cunningham. Multicolor fluorescence enhancement from a photonics crystal surface. *Appl Phys Lett*, 97(12), 2010.

[72] A. Pokhriyal, M. Lu, V. Chaudhery, C. S. Huang, S. Schulz, and B. T. Cunningham. Photonic crystal enhanced fluorescence using a quartz substrate to reduce limits of detection. *Opt Express*, 18(24):24793–808, 2010.

[73] G. A. Valaskovic, M. Holton, and G. H. Morrison. Parameter control, characterization, and optimization in the fabrication of optical fiber near-field probes. *Appl. Opt.*, 34(7):1215–1228, Mar 1995.

[74] Palash Bharadwaj, Bradley Deutsch, and Lukas Novotny. Optical antennas. *Adv. Opt. Photon.*, 1(3):438–483, 2009.

[75] John Daniel Kraus. *Antennas*. McGraw-Hill series in electrical engineering Radar and antennas. McGraw-Hill, New York, 2nd edition, 1988.

[76] D. Taillaert, W. Bogaerts, P. Bienstman, T. F. Krauss, P. Van Daele, I. Moerman, S. Verstuyft, K. De Mesel, and R. Baets. An out-of-plane grating coupler for efficient butt-coupling between compact planar waveguides and single-mode fibers. *Quantum Electronics, IEEE Journal of*, 38(7):949–955, 2002.

[77] R. Waldhausl, B. Schnabel, P. Dannberg, E. B. Kley, A. Brauer, and W. Karthe. Efficient coupling into polymer waveguides by gratings. *Appl Opt*, 36(36):9383–90, 1997.

[78] I. Giuntoni, D. Stolarek, H. Richter, S. Marschmeyer, J. Bauer, A. Gajda, J. Bruns, B. Tillack, K. Petermann, and L. Zimmermann. Deep-uv technology for the fabrication of bragg gratings on soi rib waveguides. *Photonics Technology Letters, IEEE*, 21(24):1894–1896, 2009.

[79] T. A. Savas, S. N. Shah, M. L. Schattenburg, J. M. Carter, and H. I. Smith. Achromatic interferometric lithography for 100-nm-period gratings and grids. *Journal of Vacuum Science Technology B: Microelectronics and Nanometer Structures, Volume 13, Issue 6, November 1995, pp.2732-2735*, 13:2732–2735, November 1995.

[80] P. Bienstman and R. Baets. Optical modelling of photonic crystals and vcsels using eigenmode expansion and perfectly matched layers. *Optical and Quantum Electronics*, 33(4):327–341, 2001.

[81] Cst microwave studio, 2010.

[82] P. B. Johnson and R. W. Christy. Optical constants of the noble metals. *Physical Review B*, 6(12):4370–4379, 1972.

[83] G. Schider, J. R. Krenn, W. Gotschy, B. Lamprecht, H. Ditlbacher, A. Leitner, and F. R. Aussenegg. Optical properties of ag and au nanowire gratings. *Journal of Applied Physics*, 90(8):3825–3830, 2001.

[84] F. Hao and P. Nordlander. Efficient dielectric function for fdtd simulation of the optical properties of silver and gold nanoparticles. *Chemical Physics Letters*, 446(1–3):115–118, 2007.

[85] Alexandre Vial, Anne-Sophie Grimault, Demetrio Macías, Dominique Barchiesi, and Marc Lamy de la Chapelle. Improved analytical fit of gold dispersion:application to the modeling of extinction spectra with a finite-difference time-domain method. *Physical Review B*, 71(8):085416, 2005.

[86] T. W. Lee and S. Gray. Subwavelength light bending by metal slit structures. *Opt Express*, 13(24):9652–9, 2005.

[87] Jinsu Yoo, Suresh Kumar Dhungel, and Junsin Yi. Annealing optimization of silicon nitride film for solar cell application. *Thin Solid Films*, 515(19):7611–7614, 2007.

[88] *CRC handbook of chemistry and physics*. CRC Press, Boca Raton, FL, 86th ed. edition, 2005.

[89] Ardavan F. Oskooi, David Roundy, Mihai Ibanescu, Peter Bermel, J. D. Joannopoulos, and Steven G. Johnson. Meep: A flexible free-software package for electromagnetic simulations by the fdtd method. *Computer Physics Communications*, 181(3):687–702, 2010.

[90] Dimitri A. Papathanassoglou and Brian Vohnsen. Direct visualization of evanescent optical waves. *American Journal of Physics*, 71(7):670–677, 2003.

[91] David M. Pozar. *Microwave engineering*. J. Wiley, Hoboken, NJ, 3rd edition, 2005.

[92] Steven G. Johnson, Pierre R. Villeneuve, Shanhui Fan, and J. D. Joannopoulos. Linear waveguides in photonic-crystal slabs. *PHYSICAL REVIEW B*, 62(12):8212–22, 2000.

[93] Steven G. Johnson, Shanhui Fan, Pierre R. Villeneuve, and J. D. Joannopoulos. Guided modes in photonic crystal slabs. *PHYSICAL REVIEW B*, 60(8):5751–58, 1999.

[94] Ardavan Farjadpour, David Roundy, Alejandro Rodriguez, Mihai Ibanescu, Peter Bermel, J. D. Joannopoulos, Steven G. Johnson, and Geoffrey Burr. Improving accuracy by subpixel smoothing in fdtd. *Optics Letters*, 31(20):2972–74, 2006.

[95] Xiaonan Chen, Wei Jiang, Jiaqi Chen, Lanlan Gu, and Ray T. Chen. 20 db-enhanced coupling to slot photonic crystal waveguide using multimode interference coupler. *APPLIED PHYSICS LETTERS*, 91, 2007.

[96] Alexis V. Kudryashov and Horst Weber. *Laser resonators: novel design and development*. SPIE Press, 1999.

[97] Raoul M. Stöckle, Yung Doug Suh, Volker Deckert, and Renato Zenobi. Nanoscale chemical analysis by tip-enhanced raman spectroscopy. *Chemical Physics Letters*, 318(1–3):131 – 136, 2000.

[98] D. ten Bloemendal, P. Ghenuche, R. Quidant, I. Cormack, P. Loza-Alvarez, and G. Badenes. Local field spectroscopy of metal dimers by tpl microscopy. *Plasmonics*, 1:41–44, 2006.

[99] Erik J. Sánchez, Lukas Novotny, and X. Sunney Xie. Near-field fluorescence microscopy based on two-photon excitation with metal tips. *Phys. Rev. Lett.*, 82:4014–4017, May 1999.

[100] Tim H. Taminiau, Robert J. Moerland, Frans B. Segerink, Laurens Kuipers, and Niek F. van Hulst. λ/4 resonance of an optical monopole antenna probed by single molecule fluorescence. *Nano Letters*, 7(1):28–33, 2007.

[101] R Gesche, S Kuhn, and C Andrei. Plasma ignition in a quarter-wavelength microwave slot resonator. *Journal of Physics D: Applied Physics*, 41(19):194003, 2008.

[102] P. C. Mathias, H. Y. Wu, and B. T. Cunningham. Employing two distinct photonic crystal resonances to improve fluorescence enhancement. *Appl Phys Lett*, 95(2):21111, 2009.

Vita

Lingyun Wang (王凌云) was born in Zaozhuang, Shandong Province, P. R. China on 30 July 1978, brother of Yuhan Wang, and son of Lipei Wang and Zhonglan Wang. He graduated from Zaozhuang No. 1 High School in 1996. He received the Bachelor of Science degree in Electronics and Information System at the East China Normal University (华东师范大学) in 2000, and the Master of Science in Electrical Engineering degree from the University of Alaska Fairbanks in 2002 working on ionospheric scintillation effects on GPS system. He started PhD study at the University of Texas at Austin in Dr. John Pearce's group initially in 2002, working on microwave radiometer. He joined Dr. Xiaojing Zhang's group in 2008 to finish the thesis work.

Permanent address: 2504 Johnathan Way
Leander, Texas 78641-3065
U. S. A.

This Dissertation was typeset with LaTeX[†] by the author.

[†] LaTeX is a document preparation system developed by Leslie Lamport as a special version of Donald Knuth's TeX Program.